

**ՀՀ ԳԱԱ Վ. ՀԱՄԲԱՐՁՈՒՄՅԱՆԻ ԱՆՎԱՆ ԲՅՈՒՐԱԿԱՆԻ
ԱՍՏՂԱԴԻՏԱՐԱՆ**

**ՀԱՐՈՒԹՅՈՒՆՅԱՆ ԳԵՎՈՐԳ ԳԱՐԵԳՆԻ
ՄԵԾ ՀԵՌԱՎՈՐՈՒԹՅԱՄԲ ԲԼԱԶԱՐՆԵՐԻ
ԲԱԶՄԱՀԱՃԱԽԱՅԻՆ ՃԱՌԱԳԱՅԹՄԱՆ ՄԵԽԱՆԻԶՄՆԵՐԻ
ՈՒՍՈՒՄՆԱՍԻՐՈՒԹՅՈՒՆԸ**

Ատենախոսություն

**Ա.03.02 - «Աստղաֆիզիկա, ռադիոաստղագիտություն»
մասնագիտությամբ**

**Ֆիզիկամաթեմատիկական գիտությունների
թեկնածուի գիտական աստիճանի համար**

**Գիտական ղեկավար՝
Ֆ.մ.գ.դ. Նարեկ Սահակյան**

ԵՐԵՎԱՆ-2023

**NAS RA BYURAKAN ASTROPHYSICAL OBSERVATORY AFTER V.
AMBARTSUMIAN**

GEVORG GAREGIN HARUTYUNYAN

BROADBAND STUDY OF HIGH REDSHIFT BLAZARS

DOCTORAL THESIS

**A thesis submitted in fulfillment of the requirements
for the degree of doctor of philosophy
in specialization 03.02 – “Astrophysics and radioastronomy”**

**Supervisor:
Dr. Narek Sahakyan**

YEREVAN–2023

Table of Contents

INTRODUCTION.....	5
1 DATA ANALYSIS AND THE RADIATION MECHANISMS FROM BLAZAR JETS.....	12
1.1 SWIFT TELESCOPE.....	12
1.2 FERMI-LAT TELESCOPE.....	13
1.3 RADIATION MECHANISMS OF BLAZARS.....	17
2 MULTIWAVELENGTH STUDY OF HIGH REDSHIFT BLAZARS.....	24
2.1 INTRODUCTION.....	24
2.2 THE SAMPLE.....	28
2.3 FERMI-LAT OBSERVATIONS.....	29
2.4 SWIFT OBSERVATIONS.....	30
2.5 RESULTS OF DATA ANALYSES.....	33
2.6 THE ORIGIN OF MULTIWAVLENGTH EMISSION.....	44
2.7 DISCUSSION AND CONCLUSION.....	53
2.8 SUMMARY.....	57
3 ORIGIN OF MULTIWAVELENGTH EMISSION FROM FLARING HIGH REDSHIFT BLAZAR PKS 0537-286.....	60
3.1 INTRODUCTION.....	60
3.2 FERMI-LAT OBSERVATIONS AND DATA ANALYSES.....	62
3.3 NUSTAR DATA ANALYSIS.....	64
3.4 SWIFT DATA ANALYSIS.....	65
3.1 MULTIWAVELENGTH SEDS.....	66
3.2 ORIGIN OF BROADBAND EMISSION.....	68
3.3 RESULTS AND DISCUSSIONS.....	70
3.4 SUMMARY.....	76
4 EXPLORING THE ORIGIN OF MULTIWAVELENGTH EMISSION FROM HIGH REDSHIFT BLAZAR B3 1343+451.....	78
4.1 INTRODUCTION.....	78
4.2 DATA ANALYSIS.....	79
4.3 MODELING THE SED.....	86

4.4 RESULTS AND DISCUSSION	90
4.5 CONCLUSION	91
5 MULTIWAVELENGTH PROPERTIES OF SELECTED HIGH REDSHIFT BLAZARS	93
5.1 INTRODUCTION	93
5.2 DATA ANALYSIS	94
5.3 MODELING OF MULTIWAVELENGTH SEDS	99
5.4 SUMMARY	102
CONCLUSION	105
BIBLIOGRAPHY	106

INTRODUCTION

Recent advancements in technology for both space and ground-based detectors provided new possibility to study astrophysical objects across a wide range of energy bands, including radio, infrared, optical, ultraviolet, X-ray and γ -ray. This led to developing a new field of astrophysics—multiwavelength astrophysics. This approach involves collecting data from multiple telescopes and observatories, each specializing in a particular wavelength range, and combining the data to gain a more comprehensive understanding of the object or phenomenon being studied. The multiwavelength observations and studies can lead to new insights into the physics of the universe, from the formation of stars and galaxies to the behavior of exotic objects like supermassive black holes and neutron stars.

Intense research on a new type of object known as Active Galactic Nuclei (AGNs) was sparked in the early 20th century after the discovery of emission lines in the nuclei of some galaxies, and the identification of the first quasar. The emission from AGNs is mainly generated by the compact core, which is much brighter than the rest of the galaxy. The prevailing theory is that this activity results from the accretion onto a supermassive black hole, although alternative explanations have been suggested. AGNs are distinguished by their exceptionally high luminosity, which ranks them among the most powerful extragalactic sources, and their emission can be observed across the electromagnetic spectrum.

Despite the wide range of observable properties exhibited by AGNs that have been classified to date, they share some common features. AGNs can be classified in various ways based on their properties. For example, radio emission strength, also known as loudness, is one way to classify AGNs. Radio loudness is determined by calculating the ratio of an AGN's radio and optical fluxes at 5 GHz and B-bands, respectively. If this ratio is greater than 10, the AGN is classified as radio loud; otherwise, it is considered radio quiet. Examples of radio quiet AGNs include Seyfert 1 and 2, quasars, and others, while the radio loud class includes Fanaroff–Riley Class 1 and 2 radio galaxies, blazars, and others.

Approximately 10% of AGNs are classified as radio loud, and these exhibit a narrow beam of plasma, called a jet, that is ejected from the central region of a supermassive black hole. The jet is composed of highly energetic particles, such as electrons and positrons, that are

accelerated to relativistic speeds. Along the propagation of the jet, these particles interact with the magnetic and/or photon fields and produce the observed radiation.

According to the unified model [1], AGNs are believed to have a similar internal structure, consisting of an accretion disk, broad and narrow line regions, a dusty torus, and relativistic jets. The varied observable properties of AGNs are explained by differences in the orientation of the source relative to the observer. In this model, if the AGN is viewed edge-on to the observer's line of sight, close to the torus plane, direct radiation from the accretion disk and broad line region is obscured by the torus, and only narrow lines are visible. These objects are classified as Seyfert II (Sy II) or narrow-line radio galaxies (NLRG) for radio-quiet and loud cases, respectively. A change in the viewing angle of the jet, in addition to the narrow line region, can also reveal emission from the broad line region (BLR). These objects, which make some angle relative to the torus plane, are called Seyfert I (Sy I) or broad-line radio galaxies (BLRG), depending on their radio quietness and loudness, respectively. Lastly, AGNs that have a jet which makes a small angle relative to the observer are classified as blazars.

The jet plays an important role in the study of AGNs and their classification. The appearance of radio-loud AGNs can vary greatly depending on the orientation of their jets. If the jet is oriented at a large angle with respect to the observer, the AGN is classified as a radio galaxy. On the other hand, if the jet is oriented at a small angle with respect to the observer, the AGN is classified as a blazar. Blazars are considered the most luminous and intriguing class of AGNs due to their unique and extreme characteristics. They are the brightest persistent sources in the universe and are visible even at great distances. This makes them of significant interest to astronomers and astrophysicists.

Blazars are known for their exceptional variability in amplitude and time. Some blazars even show variability on a timescale as short as minutes [2]. This, along with their strong polarization across radio and optical wavelengths, superluminal motion, and extremely high luminosities, has led to further study and interest in these objects. The short variability timescales of blazars suggest that their emission region is compact. The plasma in the jet is moving at relativistic velocities (high Lorentz factor) and because of small inclination angle the emission from blazars is strongly amplified. The relativistic beaming effect that results

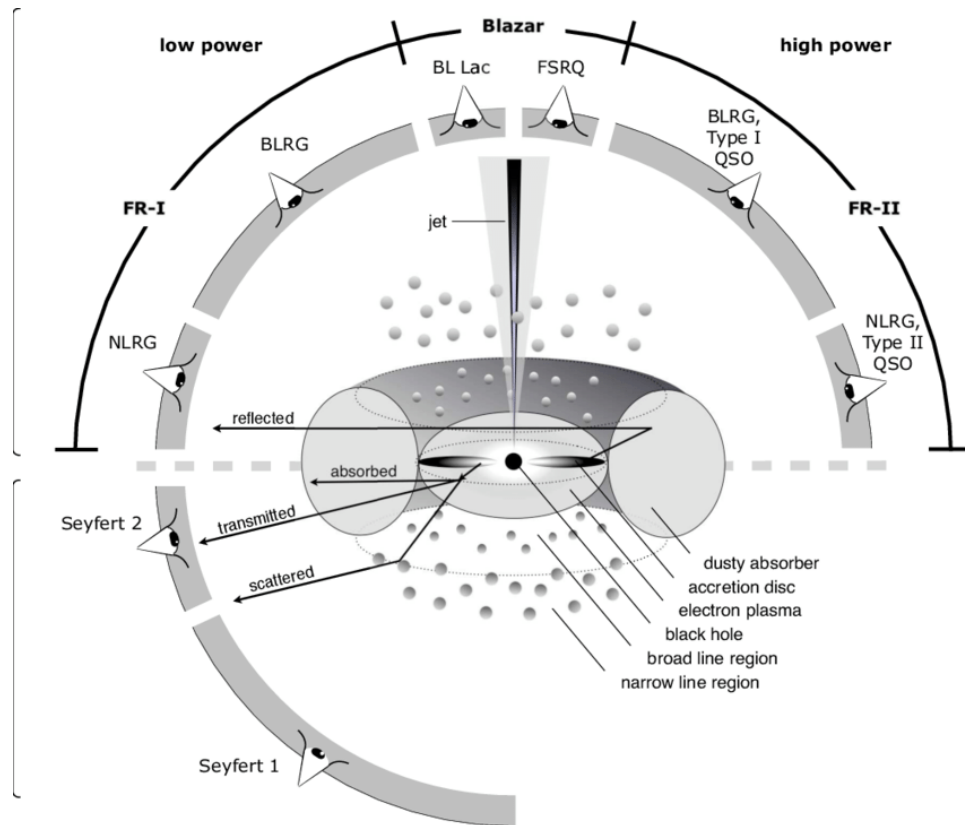


Figure 1. Unification model of AGNs [3].

from this causes blazars to appear significantly brighter in the observer's frame. This effect is an important factor in understanding the extreme luminosities of these objects.

Blazars are often separated into two groups based on their observable properties: BL Lacertae (BL-Lac) objects and Flat Spectrum Radio Quasars (FSRQs). BL-Lac objects are characterized by weak or absent emission lines, which is thought to be due to the low rate of material accretion onto the central supermassive black hole. In contrast, FSRQs are known for their broad emission lines in the optical and ultraviolet bands, and they tend to be more luminous. The accretion disks of FSRQs are extremely luminous, and in some cases, the thermal emission from these disks can surpass the non-thermal component. This is a unique feature of FSRQs compared to BL-Lac objects. The broad emission lines are thought to arise from the accretion disk and provide information about the physical conditions and processes occurring in the vicinity of the central black hole. It is important to note that these classifications are not absolute and that there is some overlap between the two groups. Some blazars can have properties of both BL-Lac objects and FSRQs, making their classification more complicated.

Blazars are known for their broad-band emission that spans a wide range of frequencies from radio to high energy (HE; >100 MeV) and even up to very high energy (VHE; >100 GeV) γ -rays (see Figure 2). The spectrum energy distribution (SED) of blazars typically consists of two components: a low energy component and a HE component. The low energy component of the SED peaks in the infrared to X-ray bands and is believed to originate from synchrotron radiation of ultra-relativistic electrons in a magnetic field. On the other hand, the HE component of the SED peaks in the X-ray to HE (and sometimes VHE) γ -ray bands. Two models have been proposed to explain the HE component of the SED: the leptonic and hadronic models. The leptonic model assumes that the HE component is produced through inverse Compton (IC) scattering of photons by HE electrons, with the Synchrotron Self-Compton (SSC) and External Compton (EIC) models being the two most widely studied scenarios. The SSC model assumes that the photons produced by synchrotron radiation are up-scattered by the same electrons [4, 5, 6]. In contrast, the EIC model considers seed photon fields from outside of the jet to be the source of the photons being up-scattered [7, 8, 9].

In addition to the leptonic models, there are also hadronic models that have been proposed to explain the HE component of the SED in blazars. These models suggest that the synchrotron radiation from protons, as well as secondary particles generated through photo-pion and photo-pair interactions, are responsible for the emission in the X-ray to HE γ -ray bands [10, 11, 12, 13]. In this case, the HE component of the SED is produced through the interactions of ultra-high energy protons with lower energy photons. The secondary particles generated through these interactions produce the emission in the X-ray to HE γ -ray bands [14].

Another classification of blazars is based on the synchrotron peak frequency. Depending on the peak location of the synchrotron radiation, blazars can be further separated into categories such as low-synchrotron-peaked (LSP $\nu_s < 10^{14}$ Hz), intermediate-synchrotron-peaked (ISP 10^{14} Hz $< \nu_s < 10^{15}$ Hz), and high-synchrotron-peaked (HSP $\nu_s > 10^{15}$ Hz) sources [15, 16]. In this classification FSRQs are predominately LSPs. Some BL Lacs, referred as extreme synchrotron BL Lac objects, also known as Extreme High-Synchrotron- Peaked BL Lacs (EHSPs), are characterized by a synchrotron peak energy that is significantly higher than that of standard HSPs. Specifically, the synchrotron peak energy of EHSPs is located

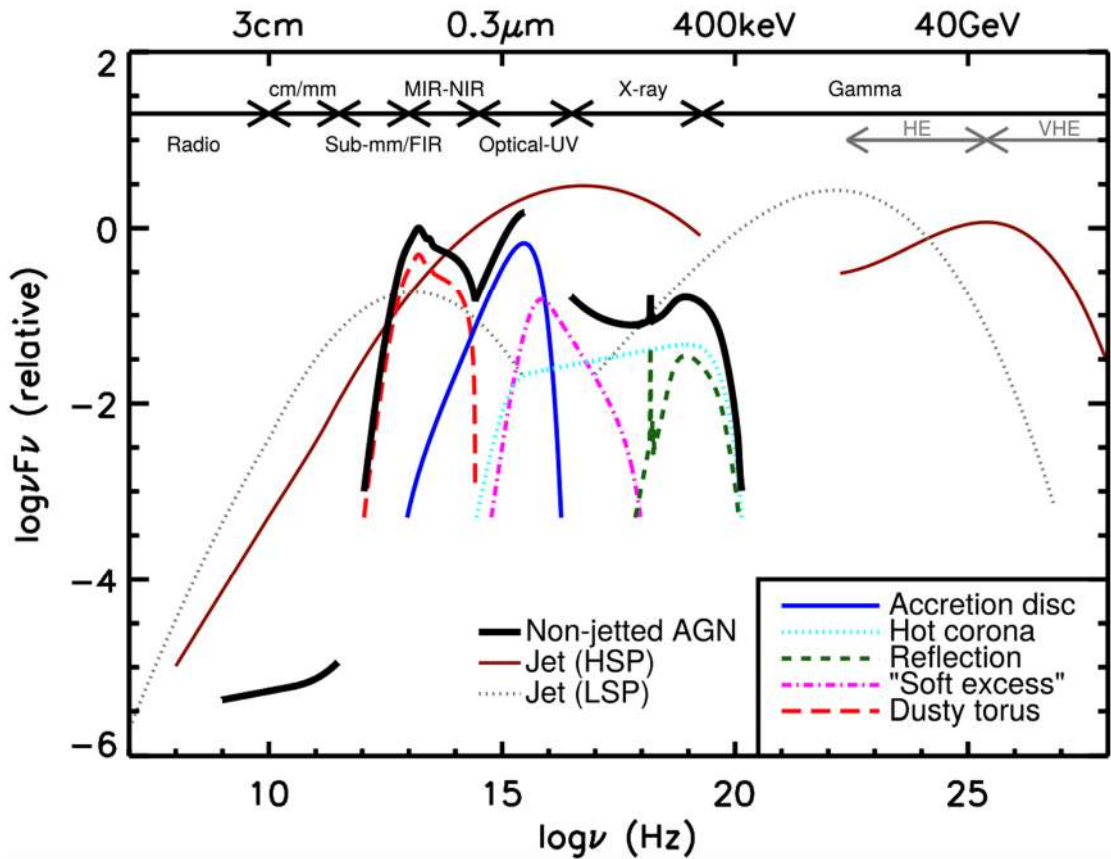


Figure 2. The SED of different types of AGNs [17].

above 2.4×10^{17} Hz (1 keV), which is an order of magnitude higher than that of standard HSPs [18].

As already have been mentioned, because of the high luminosities blazars even at high redshifts have been observed. These high redshift blazars are of particular interest because of their large distances and peculiar properties. The main focus of this thesis is comprehensive study of high redshift blazars that have been observed in HE γ -ray band. The importance to study high-red shift blazars ($z > 2.5$) is:

- High redshift blazars are some of the most distant known objects in the universe, allowing to examine the early universe and the formation of the first galaxies.
- The strong radiation from blazars will enable to understand the intergalactic medium, particularly the distribution of gas in the universe.
- Studying these objects helps to investigate the cosmological evolution of blazars and supermassive black holes.
- Large distances to high redshift blazars can be used to constrain cosmological parameters, such as the density of extragalactic background light (EBL).

- Can shed light on evolution of relativistic jets across different cosmic epochs and accretion disc-jet connection.

The second objective of this thesis is to develop a numerical package designed for analyzing data collected with Fermi-LAT allowing in-depth and efficient analysis of large amount of data. It should be noted that other available multiwavelength data (e.g., in optical/UV and X-ray band) were also used to study multiwavelength behavior of high redshift blazars.

The thesis consists of Introduction, five chapters, conclusion and references.

In Chapter 1 provided an overview of the Swift and Fermi-LAT telescopes, as well as a description of a package developed for Fermi-LAT data analysis. Additionally, the radiation mechanisms that produce the broad band SED of blazars is briefly presented.

In Chapter 2 the spectral and temporal properties of thirty-three distant blazars ($z > 2.5$) detected in the HE γ -ray band are investigated by analysing the Fermi-LAT and Swift UVOT/XRT data collected between 2008-2020 and 2006-2020 respectively. The properties of distant blazar jets are derived by modeling the multiwavelength SEDs within a one-zone leptonic scenario assuming that the X-ray and γ -ray emissions are produced from IC scattering of synchrotron and dusty torus photons.

In Chapter 3 presented a comprehensive study of PKS 0537-286, which is a high redshift blazar at a redshift of 3.1. The blazar is known for being very bright and it has been observed in the X-ray band using various instruments, which have revealed a particularly hard X-ray spectrum. The blazar has also exhibited γ -ray flares on several occasions. The broadband SED of PKS 0537-286 in the quiescent and flaring periods was modeled within a one-zone leptonic scenario assuming different locations of the emission region and considering both internal (synchrotron radiation) and external (from the disk, broad-line region and dusty torus) photon fields for the IC scattering. The modeling shows that the most optimistic scenario, from the energy requirement point of view, is when the jet energy dissipation occurs within the broad-line region. The excess emission observed in the optical/UV band is attributed to emission from a bright thermal accretion disk.

In Chapter 4 the broadband emission from a distant blazar B3 1343+451 have been studied. In recent years, this blazar has been observed to be in a high emission/bright flaring

state in the γ -ray band, which is remarkable considering its distance ($z = 2.534$). Swift Observatory has also monitored the source in various years, providing data in optical/UV and X-ray bands. The large amount of data available in the γ -ray band (more than ten years) and the periods of flaring state enabled a detailed investigation of the origin of multiwavelength emission from B3 1343+451. The SED of B3 1343+451 is modeled during the quiescent and flaring periods assuming a compact emitting region outside the BLR. It is found that the flares can be explained by only changing the bulk Lorentz factor of the emitting region without significant modification of the emitting electron parameters and luminosity of the jet.

In Chapter 5, the origin of broadband emission from 7 high redshift blazars (redshift greater than 2.5) was studied by analyzing data from Swift UVOT/XRT and Fermi-LAT. During the analysis, several flaring periods were observed in blazars such as PKS 1830-211, LQAC 247-061, TXS 0536+145, and 4C+41.32, characterized by an increase in flux and a hardening of the photon index in the HE γ -ray band. To model the time-averaged broadband SED of these sources, a one-zone leptonic emission model was applied, taking into account both synchrotron and external photons for the IC scattering. The parameters of the emitting particles and the energetics of the jet were also estimated as part of the analysis.

1 DATA ANALYSIS AND THE RADIATION MECHANISMS FROM BLAZAR JETS.

In this chapter, we provide the steps on how to analyze the data accumulated from Fermi Large Area Telescope (Fermi-LAT) and Swift telescopes, as well as provide a brief overview of the radiation mechanisms occurring within blazar jets. Furthermore, automated tool designed to analyze Fermi-LAT data is presented.

1.1 SWIFT TELESCOPE

The Neil Gehrels Swift Observatory, previously known as the Swift Gamma-Ray Burst Explorer, was launched on November 20, 2004 [19]. This versatile observatory is capable of conducting quasi-simultaneous observations across multiple bands, including optical, ultraviolet, and X-ray wavebands. As such, it plays a crucial role in examining the underlying physics of various astronomical phenomena. While its primary objective is to identify, investigate, and classify GRBs—believed to originate from high-mass stars transforming into neutron stars or black holes through explosive events or from the merging of two neutron stars—the Swift telescope has also proven valuable in studying AGNs, X-ray binaries, supernovae, and other celestial objects. The telescope is equipped with three distinct instruments, namely.

THE BURST ALERT TELESCOPE (BAT): The BAT is an imaging telescope and the largest instrument on the SWIFT telescope [20]. The BAT operates in the range of 15-150 keV and is highly sensitive, capable of detecting events with an accuracy of 1 to 4 arcminutes. After detecting an event, the BAT sends a signal to the other instruments, UVOT and XRT, to point out the same event, making it possible to obtain data in optical, ultraviolet, and X-ray bands almost simultaneously.

THE X-RAY TELESCOPE (XRT): The XRT is an X-ray telescope that images the sky which can be used for spectral analysis [21]. The performance range of the XRT is 0.2-10 keV. The XRT has four observation modes:

Imaging mode - which computes the energy in each pixel.

Photodiode mode - which allows us to obtain data from sources.

Windowed timing mode - which provides information about the one-dimensional position of the source.

Photon counting mode - in which the XRT performs spectral and spatial analysis, which is most suitable for powerful sources.

THE ULTRAVIOLET/OPTICAL TELESCOPE (UVOT): The main purpose of the UVOT is to detect optical and ultraviolet radiation and the working range of the UVOT is 1600 – 6000 Å [22]. It includes seven main filters *v*, *b*, *u*, *uvw1*, *uvw2*, *uvw2*, and *white* with corresponding wavelengths of 5402 Å, 4329 Å, 3501 Å, 2634 Å, 2231 Å, 2030 Å, and 3471 Å respectively. The UVOT has three working modes, similar to the XRT:

Event mode -the UVOT provides data about each detected event.

Image mode – gives binned and two-dimensional image of the event.

Event and Image – above mentioned two modes taken together.

For multiwavelength observations of astrophysical events, it is necessary to combine data from other telescopes. For example, to study the HE behavior of blazars, data accumulated with Fermi-LAT is essential.

1.2 FERMI-LAT TELESCOPE

The Fermi Gamma-ray Space Telescope is a space-based observatory launched by NASA into orbit on June 11, 2008. The main objective of the Fermi telescope is to investigate the high-energy universe by observing γ -rays. The Fermi spacecraft has two instruments onboard: The Fermi-LAT and the Gamma-ray Burst Monitor (GBM).

The Fermi-LAT is designed to survey the entire sky every three hours and it has been used to study a wide range of HE phenomena, including blazars. The Fermi-LAT observes the entire sky within an energy range of 20 MeV to 1 TeV. The main components of the Fermi-LAT's structure are the tracker, calorimeter, and anticoincidence detector. The tracker detects γ -rays, which undergo a pair conversion process. Firstly, the γ -rays interact with layers of silicon strip detectors and tungsten converter plates. The γ -rays are then absorbed by the tungsten plates, producing an electron-positron pair, which transfers energy to the silicon strip detectors. This energy deposit is then used to determine the direction and energy of the original γ -rays.

The calorimeter, which is composed of cesium iodide crystals, calculates the total energy of the electron-positron pair. Information from both the tracker and calorimeter is combined to identify the original γ -rays and their energy. To dismiss the "effect" of incidental charged particles, an anticoincidence detector (ACD) is used [23]. For instance, γ -rays that originate from the interaction of cosmic rays with the Earth's limbs are identified as background events and rejected by ACD. The efficacy of ACD to reject background radiation is up to 99.9%.

The performance of the Fermi-LAT is defined by three main factors: the design of the hardware, algorithms used for event reconstruction, and background selection. To describe the performance of the LAT, Instrument Response Functions (IRFs) are created. IRFs are mathematical functions that describe how the Fermi telescope responds to incoming γ -rays, taking into account parameters such as photon energy, incidence angle, and conversion point within the instrument. To better evaluate the LAT response functions, a Monte Carlo simulation is performed, which simulates a large number of γ -ray events to cover all possible photon inclination angles and energies. The important arguments of IRFs are the effective area, which measures the efficiency of the detector, the point-spread function, and energy dispersion.

Effective Area: The Effective Area (A_{eff}) of a γ -ray detector is a measure of its sensitivity to γ -rays as a function of energy and direction. It is calculated as the fraction of incoming γ -rays that are detected by the detector, taking into account the probability of interaction and detection efficiency as a function of energy and direction. Typically expressed in units of cm^2 , and it can be viewed as the "window" that γ -rays must pass through to be detected. The larger the Effective Area, the more sensitive the detector is to γ -rays and the better it can detect fainter sources.

Energy Dispersion: The energy dispersion of the LAT is described by how much the reconstructed energy (E') of an event differs from its true energy (E), expressed as a fraction.

$$\frac{\delta E}{E} = \frac{E' - E}{E} \quad (1. 1)$$

Point Spread Function: The Point Spread Function (PSF) of the LAT is a measure of its angular resolution, which describes the ability of the telescope to distinguish between two closely spaced γ -ray sources. The PSF is defined as the probability density function of the

angular separation between the reconstructed position of a γ -ray event and the true position of the γ -ray source in the sky.

$$\delta p = 2 \sin^{-1} \left(\frac{|\hat{p}' - \hat{p}|}{2} \right) \quad (1. 2)$$

The reconstructed direction is represented by \hat{p}' while the true direction of the photon is represented by \hat{p} .

Fermi continuously collects data and has produced a large amount of data for almost fifteen years, which requires analysis. The data analysis process is being implemented using tools developed by the Fermi-LAT collaboration. The automation of the data analysis process using Fermi tools and the Python programming language will facilitate and speed up the extraction, preparation, and analysis processes of the data accumulated by the telescope. As a result, the MADAM package was developed, which stands for Multiwavelength Astrophysical Data Analysis Machine. The working principles and structure of the MADAM are described below.

MADAM: The package was developed using Python programming language to perform a comprehensive analysis of Fermi-LAT data. Here's a more in-depth description of the process:

- Input Arguments: The analysis starts by inputting the necessary arguments through the command-line interface (CLI). Arguments are associative and catalog names of the source, time interval which can be in MET, MJD, and Gregorian date formats, energy range in MeV, radius of interest, binning size for light curve in days, core number which defines how many cores to use during the analysis, and booleans to instruct to calculate light curves, adaptively binned light curve, Bayesian blocks, and SED for adaptive bins. As an example of the command line is shown in Figure 1.1.
- Data Download: After running the package using .sh file the sub-package responsible for queries downloads the Fermi-LAT data from Fermi data center with above specified parameters.
- Data Processing and Model Creation: The package applies several Fermi Tools commands on the downloaded data, for example *gtselect* command to define the specific parameters of the data time intervals, energy ranges, and event classes and *gtmktime* to select time intervals during which the Fermi-LAT data is considered valid for analysis. Based on *gtselect* and *gtmktime* counts map (CMAP) is being created using *gtbin* command to create


a model later. Then model submodule creates a model based on the processed data with last version of `make4FGLxml.py` python script.

- Fitting and Response Function: Created model file is an input for fitting and response functions which executing parallel to save time. `gtdiffrsp` tool generates the effective area and PSF correction files needed for spectral analysis of the Fermi-LAT data, while the `gtlike` function fits a model to the data to get the spectral parameters. To determine the best value of the spectral model parameters they are being varied to maximize likelihood. The likelihood (L) represents the probability of obtaining the data from a given input model, which, in this scenario, is the arrangement of γ -ray sources in the model. Additionally, `gttsmap` tool is applied to produce a map of test-statistics for the purpose of detecting and locating sources. Test statistic (TS) can be expressed as:

$$TS = -2\ln\left(\frac{L_{max,0}}{L_{max,1}}\right) \quad (1.3)$$

where $L_{max,0}$ is the ‘null hypothesis’ namely the maximum likelihood of a model without new sources and $L_{max,1}$ is a maximum likelihood considering new sources. So, large TS indicates that the source is most likely in the given position.

- SED and Light Curve Creation: The output of the fitting process is then used as an input for modules that create the SED and light curves (LCs). The SED is created with logarithmically equal 4, 5, and 6 bins respectively, and a comparison plot is generated to compare the catalog SED points with the results obtained from the analysis. To calculate LCs whole period is being divided to shorter and equal bins (intervals) and for each bin is being implemented binned or unbinned analysis depending on bin size. The LCs is created in parallel too, to reduce the overall processing time especially when bins count is large.
- Adaptive binned light curve and Bayesian Blocks: There is a class in the package that are responsible to calculate an Adaptively Binned light curve and then SED for each adaptive



```

user2@icranet-dell: ~/Desktop/gev_working/madam
File Edit View Search Terminal Tabs Help
user2@icranet-dell: ~/Desktop/jupyter x user2@icranet-dell: ~/Desktop/gev_w... x user2@icranet-dell: ~/Desktop/gev_w... x +
(fermi) user2@icranet-dell:~/Desktop/gev_working/madam$ python madam fermi_run --assoc_name "PKS 0726-476" --ca
talog_name "4FGL J0728.0-4740" -tmin 239557417 -tmax 691804805 -emin 100 -emax 300000 -ttype "MET" -bin_size 30
-core_num 50 -run_lc False -adaptive_lc False -bayes_block False -run_adaptive_sed False -rad 12

```

Figure 1.1 Command to run the MADAM package

bin. Based on Adaptively Binned light curve result file, Bayesian Blocks is being computed. The idea of the adaptive binning is to create such bins in which the number of registered counts almost the same. It means in active periods bin will be shorter than in quiescent periods. Bayesian methods merges consecutive bins which have the same level of flux. These methods provide a more detailed view of the source behavior which may not be apparent in larger dataset.

- Interpretation of results: The last step is an interpretation of obtained results and some of them are shown in Figure 1.2.

1.3 RADIATION MECHANISMS OF BLAZARS

This subchapter discusses the main radiation mechanisms that describe non-thermal emission occurring in the jets of blazars. Understanding these processes is crucial as they can shed light on the physical properties of blazars, such as particle acceleration up to HE, huge magnetic fields, and the energetics of the jet.

SYNCHROTRON RADIATION: The synchrotron radiation ranges from radio to X-ray band and describes low energy component of SED of blazars. Synchrotron radiation occurs when an accelerated particle is moving spirally under magnetic field. This kind of emission is due to Lorentz force which makes the particle to gyrate around lines of the magnetic field. When only Lorentz force acts on a relativistic particle ($E = 0$) we have [24],

$$\vec{F}_L = \frac{d}{dt}(\gamma m \vec{v}) = \frac{e}{c} [\vec{v} \times \vec{B}] \quad (1. 4)$$

where B is magnetic field, m and e is an electron rest mass and charge respectively, γ is the Lorentz factor and \vec{v} is the velocity of the vector of electron. Lorentz force has two components from which $F_{L\parallel} = 0$ therefore $a_{\parallel} = 0$ and,

$$F_{L\perp} = \gamma m \frac{dv_{\perp}}{dt} = e \frac{v_{\perp}}{c} B \rightarrow a_{\perp} = \frac{evB \sin \theta}{\gamma mc} \quad (1. 5).$$

In the general case Larmor's formula is [24],

$$P_e = \dot{P}_e = \frac{2e^2}{3c^3} [\dot{a}'_{\parallel}{}^2 + \dot{a}'_{\perp}{}^2] = \frac{2e^2}{3c^3} \gamma^4 [\gamma^2 a_{\parallel}{}^2 + a_{\perp}{}^2] \quad (1. 6).$$

Here were taken into account that Lorentz transformations for two components of accelerations are $\dot{a}'_{\parallel} = \gamma^3 \dot{a}_{\parallel}$ and $\dot{a}'_{\perp} = \gamma^2 \dot{a}_{\perp}$ (primed is the rest frame of an electron and non-primed is an observer's frame) respectively.

Replacing a_{\perp} in Eq.1.6 by Eq.1.5 we get total loss of an electron in case of synchrotron radiation which is [24],

$$P_S = \frac{2e^4}{3m^2c^3} B^2 \gamma^2 \beta^2 \sin^2 \theta \quad (1.7)$$

where $a_{\parallel} = 0$, $\beta = v/c$, θ is a pitch angle.

To make Eq.1.7 simpler let's define $U_B = B^2/8\pi$ as magnetic field density, $r_0 = e^2/mc^2$ classical electron radius and $\sigma_T = 8\pi r_0^2/3 = 6.65 \times 10^{-25} \text{cm}^2$ as Thomson scattering cross section. Using these definitions and isotropic distribution of pitch angles the Eq.1.7 can be rewritten,

$$P_S(t) = -\frac{dE}{dt} = \frac{4}{3} U \sigma \gamma^2 c \beta^2 \quad (1.8)$$

A differential spectrum of an individual electron which spiraling around magnetic field and radiates in a certain range of frequencies shown in Figure 1.3 and can be computed from the following [25],

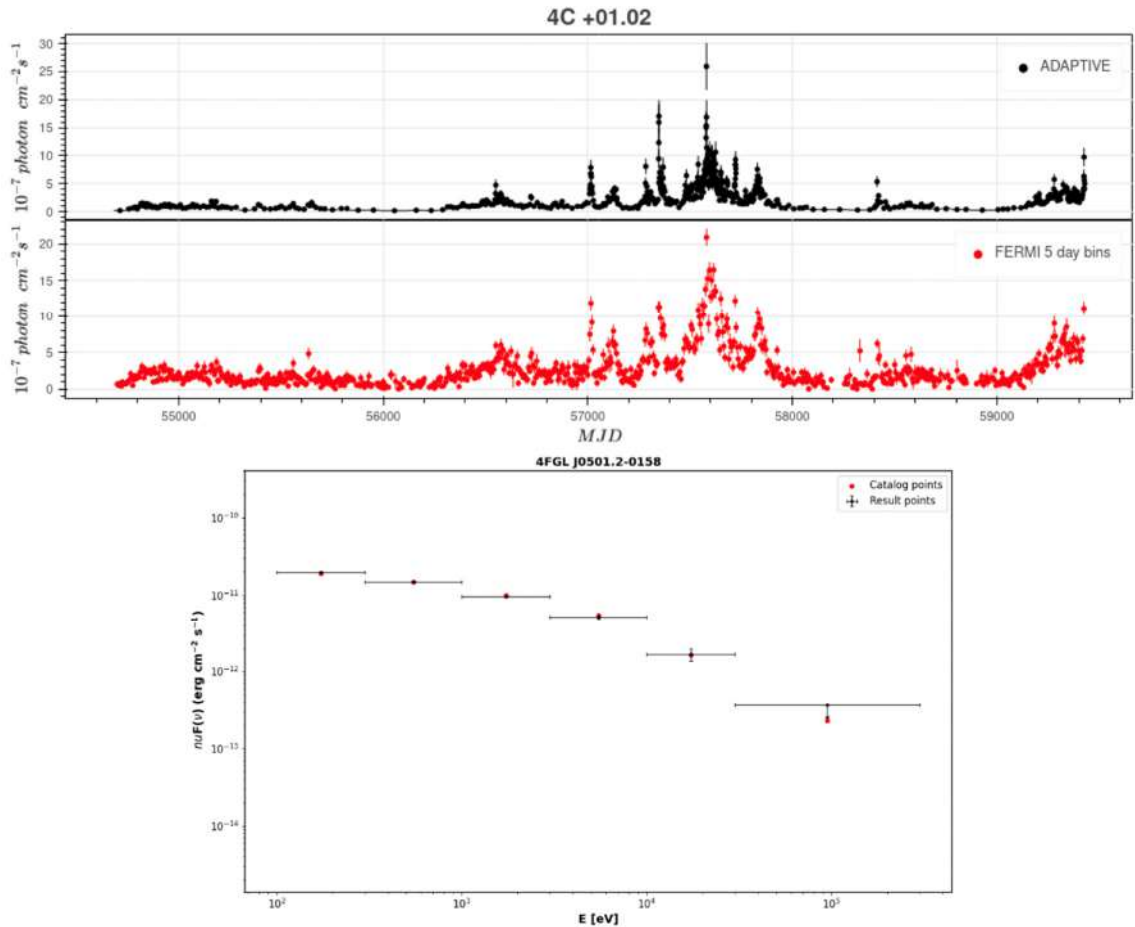


Figure 1.2 Results of the package: LCs of the source showing changes in brightness over time (above) and comparison plot of SEDs(below).

$$\frac{dN_\gamma}{dE_\gamma dt} = \frac{\sqrt{3}}{2\pi\hbar} \frac{e^3 B}{mc^2 E_\gamma} F\left(\frac{E_\gamma}{E_c}\right) \quad (1.9)$$

where \hbar is the Plank's constant, E_c is a characteristic energy,

$$E_c = \frac{3}{2} \frac{\hbar e B}{mc} \gamma^2, \quad \gamma = \frac{E_e}{mc^2} \quad (1.10)$$

and $F(x)$ is defined as,

$$F(x) = x \int_x^\infty K_{5/3}(x') dx' \quad (1.11)$$

where $K_{5/3}$ is the modified Bessel function with order of 5/3 [25]. Eq.1.11 can be approximated by,

$$F(x) \approx 2.15x^{1/3}(1 + 3.06x)^{1/6} \frac{1+0.884x^{2/3}+0.471x^{4/3}}{1+1.64x^{2/3}+0.974x^{4/3}} e^{-x} \quad (1.12)$$

It is convenient to use Eq.1.12 because it is more precisely in case of large range of x values. As shown in Figure 1.3 spectrum of an electron is peaking at $0.29E_c$. Assuming that the radiation is coming from population of electrons, it is necessary to take into account energy distribution of the particles. Charged particles inside the jets of AGNs can be accelerated by the relativistic shocks and distribution can be described by a power-law [26] or power-law with exponential cut-off [27],

$$N(E) = N_0 E^{-p} \quad (1.13),$$

$$N(E) = N_0 E^{-p} \exp(-E/E_{cut}) \quad (1.14).$$

In the blazar jet, the emitting region contain electrons with different energy and their distributions are given by Eq. 1.13 and 1.14. To obtain the energy spectrum emitted by these particles due to synchrotron emission, the individual spectrum of a single particle should be multiplied by the distribution and integrated. Therefore, for the synchrotron flux (energy on a surface of 1 cm^2 in per second) of a population of electrons, we have,

$$\left(\frac{dN_\gamma}{dE_\gamma dt}\right)_N = \int_{E_{min}}^{E_{max}} \left(\frac{dN_\gamma}{dE_\gamma dt}\right)_1 N(E) dE \quad (1.15)$$

Electrons between the energy range E to $E + dE$ radiates photons with the frequencies in the range of ν to $\nu + d\nu$ and in that range the following relation occurs [24],

$$F(\nu) \sim B^{\frac{(p+1)}{2}} \nu^{-\frac{(p-1)}{2}} \quad (1.16)$$

The importance of Eq. 1.16 is that a power law distribution of energies of radiated photons follows from the radiation of electrons with a power law energy distribution. The spectral index, $\alpha = (p - 1)/2$, is known where p is the slope of the electron energy spectrum.

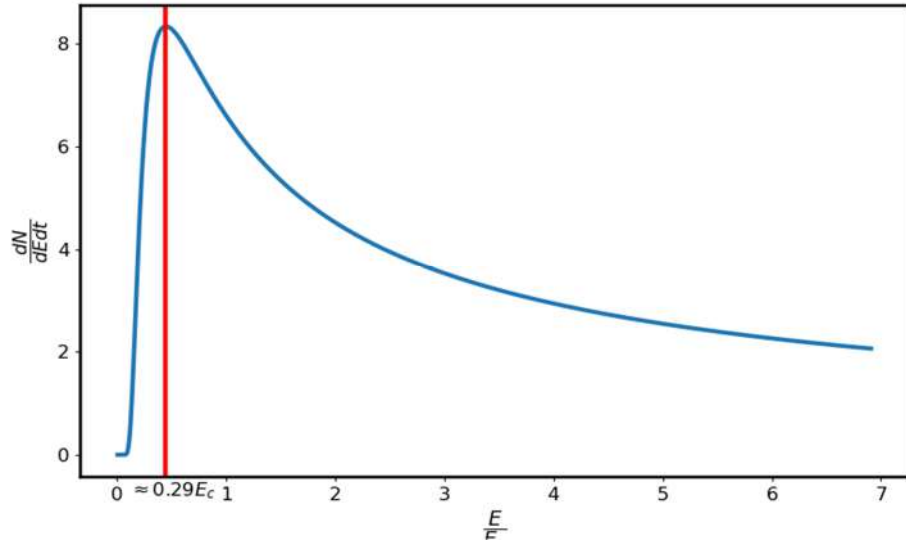


Figure 1.3 Differential spectrum of an electron.

INVERSE COMPTON RADIATION: The HE component of the SED of blazars is primarily due to IC scattering, which occurs when a high-energy particle, usually an electron, interacts with a low-energy photon. During this interaction, the electron loses energy while the photon gains energy. IC scattering can range from X-rays up to HE and VHE γ -rays. There are two regimes of IC scattering depending on the energy of the interacting particles. When the energy of the incoming photon is smaller than the energy of the electron in its rest frame ($h\nu < m_e c^2$) then regime is called Thomson regime and final energy of the scattered photon is proportional to γ^2 . On the other hand ($h\nu > m_e c^2$) we have the Klein-Nishina regime which considers quantum electrodynamics and in which the scattered photon energy is proportional to γ . The total energy losses of an electron that satisfy both cases can be given by the following equation [28],

$$\frac{d\gamma}{dt} = \frac{4}{3} \frac{c\sigma_T}{m_e c^2} U_0 \gamma^2 F_{KN}, \quad F_{KN} = \frac{1}{U_0} \int_{\varepsilon_{min}}^{\varepsilon_{max}} f_{KN}(\tilde{b}) U_\varepsilon d\varepsilon \quad (1.17)$$

where $U_0 = \int_{\varepsilon_{min}}^{\varepsilon_{max}} U_\varepsilon d\varepsilon$ energy density of seed photons field, $\tilde{b} = \frac{4\gamma\varepsilon}{m_e c^2}$ and,

$$\begin{cases} \tilde{b} \ll 1 & f_{KN} = 1 & \text{Thomson regime} \\ \tilde{b} \gg 1 & f_{KN} = \frac{9}{2\tilde{b}^2} \left(\ln(\tilde{b}) - \frac{11}{6} \right) & \text{Klein - Nishina regime} \end{cases} \quad (1.18).$$

Using approximation of F_{KN} function Eq. 1.17 can be rewritten as [28],

$$\frac{d\gamma}{dt} = \frac{4}{3} \frac{c\sigma_T}{m_e c^2} U_0 \gamma^2 \frac{1}{(1+\tilde{b})^{1.5}} \quad (1.19)$$

If initial and final energies of the scattered photon are ε_i and ε_f correspondingly the

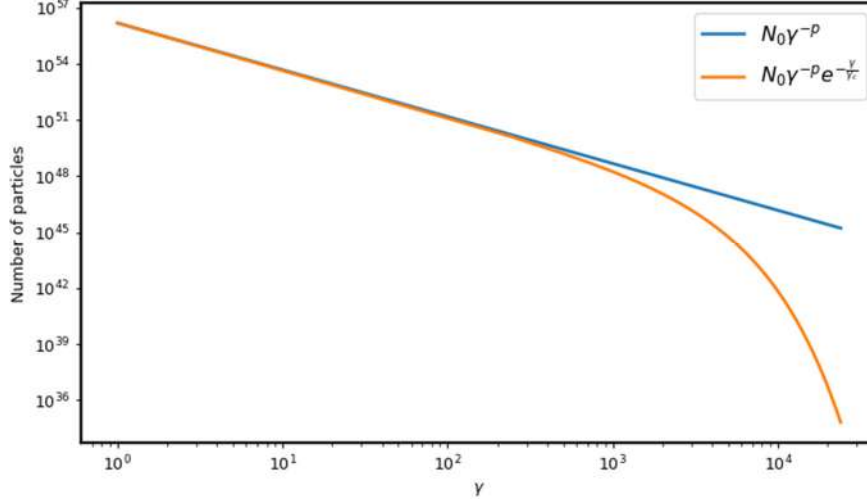


Figure 1.4 Difference between two distributions.

differential spectrum of the IC scattering will be [29],

$$\frac{dN}{dt d\varepsilon_f} = \frac{2\pi r_0^2 m_e c}{\gamma^2} \frac{n(\varepsilon_i) d\varepsilon_i}{\varepsilon_i} F_c(q, \Gamma_e) \quad (1. 20),$$

where $n(\varepsilon_i)$ is the low energy photon field, γ is the energy of an interacting electron and $F_c(q, \Gamma_e)$ is the cross section of IC which is presented as follows [29],

$$F_c(q, \Gamma_e) = \left[2q \ln q + (1 + 2q)(1 - q) + \frac{1}{2} \frac{(\Gamma_e q)^2}{1 + \Gamma_e q} (1 - q) \right] \quad (1. 21).$$

In Eq. 1.21 should be taken account that:

$$q = \frac{E_1}{\Gamma_e(1-E_1)}, \quad \Gamma_e = \frac{4\gamma\varepsilon}{m_e c^2}, \quad E_1 = \varepsilon_1(\gamma m_e c^2) \quad (1. 22).$$

Similar to the synchrotron radiation spectrum of a single electron, the combined spectrum of IC radiation for a group of electrons can be calculated by integrating Eq. 1.20 over all electron energies. In the case of IC, the luminosity, or quantity of energy radiated per second, can be calculated as follows [30],

$$L(\varepsilon_s) = \frac{3}{4} c \sigma_T \varepsilon_s^2 \int_0^\infty d\varepsilon \frac{u(\varepsilon)}{\varepsilon^2} \int_{\gamma_{min}}^{\gamma_{max}} d\gamma \frac{N_e(\gamma)}{\gamma^2} F_c(q, \Gamma_e) \quad (1. 23).$$

In Eq. 1.23 ε_s is scattered photon energy, σ_T is the cross section, $u(\varepsilon)$ is the energy density of seed photons field, $N_e(\gamma)$ is the energy distribution of electrons (see Eq. 1.13 and Eq. 1.14).

Depending on location of the emitting region (blob) as a target photon for IC can be photons produced by synchrotron radiation (synchrotron self-Compton [6, 5, 4]) or external fields such as thermal photons emitted by accretion disc directly, photons reflected from BLR and infrared photons from dusty torus [9, 7].

SYNCHROTRON SELF-COMPTON: Synchrotron self-Compton (SSC) is a specific case of IC when in a compact emitting region, synchrotron photons up-scattering on the same population of relativistic electrons that caused synchrotron radiation. Assuming that the distribution of electrons and photons is an isotropic and homogenous $L_{SSC}(\varepsilon_s)$ can be computed using Eq. 1.23 considering these limits,

$$\frac{1}{4\gamma^2} \leq q \leq 1, \quad \gamma_{min} = \frac{1}{2} \frac{\varepsilon_s(1+z)}{\delta_D} \left(1 + \sqrt{1 + \left(\varepsilon \frac{\varepsilon_s(1+z)}{\delta_D} \right)^{-1}} \right) \quad (1. 24).$$

In Eq. 1.24 δ_D is the Doppler factor, z is redshift, $u(\varepsilon) = u_{SSC}(\varepsilon)$ is the energy density of synchrotron photons and,

$$u_{SSC}(\varepsilon) = \frac{L_{syn}(\varepsilon)}{4 \pi c R_b'^2} \quad (1. 25).$$

In SSC mechanism the radiation was assumed to come from a spherical emission region which volume is $V_B' = \frac{4}{3} \pi (R_b')^3$ and minimum time of observed variability allows to constrain R_b' as,

$$R_b' \leq \frac{\delta_D c t_{obs}}{(1+z)} \quad (1. 26).$$

EXTERNAL INVERSE COMPTON: As mentioned above, the distance of the emitting region from the central source plays a crucial role, and depending on that, the soft photon field for IC can differ (Fig 2.4 [31]). Unlike SSC, for external inverse Compton (EIC), seed photons are outside of the jet. The main external photon fields that can impact IC are thermal photons emitted from the accretion disc, the same photons reprocessed and reemitted from the BLR, and infrared photons from the molecular and dusty torus. The luminosity for the EIC radiation is calculated by this general formula [30],

$$L_{ext}(\varepsilon) = \frac{15}{\pi^4} \xi_{ext} L_{disk} \frac{(\varepsilon/kT_{ext})^4}{\exp \varepsilon/kT_{ext} - 1} \quad (1. 27)$$

where ξ_{ext} shows portion of the reprocessed emission in BLR or torus and values are $\xi_{BLR} = 0.6$, $\xi_{dust} = 0.3$ respectively, L_{disk} is the luminosity of the accretion disc and T_{ext} is the temperature of the external field. Photon energy densities for external fields can be computed by this overall formula [32, 33],

$$u_{ext}(\varepsilon, r) = \frac{L_{ext}(\varepsilon)}{4 \pi c R_{ext}^2} \frac{1}{1 + (r/R_{ext})^{n_{ext}}} \quad (1. 28)$$

where $L_{ext}(\varepsilon)$ is given by Eq. 1.27, $n_{ext} = 4$ in case of BLR and 3 for torus, r and R_{ext} are

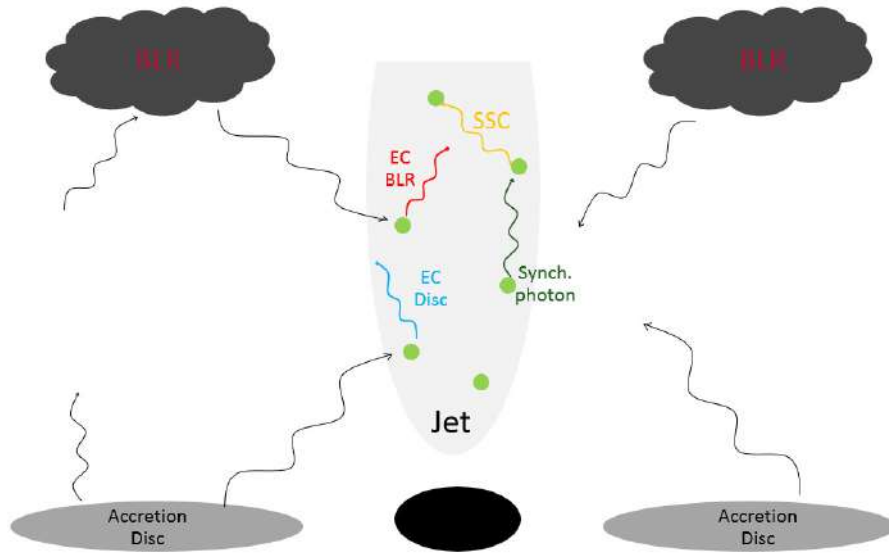


Figure 1.5 Low energy photon fields which can serve as a target for IC scattering.

the distances of emitting region and external field from the central engine correspondingly. R_{ext} is determined by these formulas [34, 35],

$$R_{BLR} = 10^{17} \left(\frac{L_{disk}}{10^{45}} \right)^{0.5} \text{ cm} \quad (1.29),$$

$$R_{dust} = 0.4 (L_{disk}/10^{45})^{0.5} (1500 \text{ K}/T_{dust})^{2.6} \text{ pc} \quad (1.30).$$

2 MULTIWAVELENGTH STUDY OF HIGH REDSHIFT BLAZARS

2.1 INTRODUCTION

Blazars are the dominant sources in the extragalactic γ -ray sky. Among the total 5000 sources in the Fermi-LAT fourth source catalog of γ -ray sources (4FGL [36]), 2800 are blazars, 45 are radio galaxies, and 19 are other AGNs. Low- to high- redshift blazars are observed showing different redshift distributions for FSRQs and BL Lacs; the distribution of FSRQs has a peak around $z = 1$ with a median of 1.14 ± 0.62 and there is a high number of FSRQs at the redshift of $\simeq 0.5 - 2.0$, while the peak of BL Lacs is at $z = 0.3$ with a mean of 0.34 ± 0.42 .

There are only 105 sources detected with $z > 2$ (3.75 per cent of total sources) and only 33 with $z > 2.5$ (1.18 per cent). Blazars harboring supermassive black holes are valuable sources for studying the relativistic outflows and formation and propagation of relativistic jets. In this context, the high redshift blazars ($z > 2.5$) are of particular interest; they are the most powerful nonexplosive astrophysical sources having ever been detected in the γ -ray band. Their study can shed light on the further understanding of the cosmological evolution of blazars and supermassive black holes and also on the evolution of relativistic jets across different cosmic epochs [37]. Moreover, the γ -ray observations of distant blazars are important since a limit on the density of the Extragalactic Background Light (EBL) can be derived. The γ -rays, as they propagate from their sources to the Earth, are subject to absorption through two-photon pair production when interacting with EBL photons [38, 39]. This absorption feature is visible in the spectrum of the nearby sources only at VHEs while for distant sources ($z > 2.0$), it can be significant already at tens of GeV. Thus, the EBL density in a redshift-dependence way can be constrained or measured by analyzing the γ -ray data (e.g., [40, 41, 42, 43]). However, if the γ -ray spectrum does not extend above 10 GeV to constrain the EBL density, by the theoretical interpretation of the data, the intrinsic source processes can be investigated and separated from the propagation effects which can be a help in the observations of distant blazars by future telescopes (e.g., CTA).

The vast majority of high redshift blazars are LSPs so the HE peak in their SEDs is at MeV

Table 2.1: List of γ -ray emitting blazars at $z > 2.5$. The results of observation of distant blazars from August 4, 2008, to August 4, 2018 by Fermi-LAT are presented in the right part of the table.

Object	4FGL name	Class	RA	Dec	F_{γ}^1	Photon index	TS	E_{\max}^2	Probability	z
GB 1508+5714	J1510.1+5702	FSRQ	227.54	57.04	0.76 ± 0.15	2.95 ± 0.15	63.50	8.76	0.8268	4.31
PKS 1351-018	J1354.3-0206	FSRQ	208.50	-2.11	1.11 ± 0.15	2.69 ± 0.09	98.49	1.30	0.7010	3.72
MG3 J163554+3629	J1635.6+3628	BCU	248.92	36.48	1.46 ± 0.27	2.84 ± 0.12	123.95	3.74	0.8413	3.65
NVSS J121915 +365718	J1219.0+3653	BCU	184.77	36.89	0.22 ± 0.08	2.20 ± 0.14	40.56	2.67	0.8273	3.53
PKS 0335-122	J0337.8-1157	FSRQ	54.47	-11.96	0.72 ± 0.16	2.69 ± 0.13	49.47	10.19	0.9245	3.44
PKS 0537-286	J0539.9-2839	FSRQ	84.99	-28.66	4.38 ± 0.18	2.72 ± 0.03	1694.80	7.60	0.9619	3.10
TXS 0800+618	J0805.4+6147	FSRQ	121.36	61.80	2.23 ± 0.14	2.82 ± 0.05	475.17	4.83	0.8441	3.03
S4 1427+543	J1428.9+5406	FSRQ	217.23	54.11	0.59 ± 0.15	2.62 ± 0.14	67.10	10.26	0.7831	3.01
GB6 J0733+0456	J0733.8+0455	FSRQ	113.47	4.93	1.14 ± 0.15	2.39 ± 0.07	197.26	17.65	0.9854	3.01
B2 0743+25	J0746.4+2546	FSRQ	116.60	25.77	2.06 ± 0.19	2.87 ± 0.07	280.99	1.52	0.7449	2.99
PKS 0347-211	J0349.8-2103	FSRQ	57.47	-21.06	3.25 ± 0.15	2.47 ± 0.03	1372.81	5.83	0.9690	2.94
S4 1124+57	J1127.4+5648	FSRQ	171.87	56.80	0.96 ± 0.13	2.75 ± 0.09	147.30	7.09	0.8495	2.89
MRSS 291-81526	J2313.9-4501	BCU	348.49	-45.02	0.89 ± 0.20	2.80 ± 0.13	81.12	2.25	0.7550	2.88
PKS 0438-43	J0440.3-4333	FSRQ	70.09	-43.55	2.24 ± 0.20	2.60 ± 0.05	574.84	2.00	0.9225	2.85
S4 2015+65	J2015.4+6556	FSRQ	303.86	65.95	0.39 ± 0.15	2.37 ± 0.15	23.77	4.34	0.7257	2.84
87GB 214302.1+095227	J2145.5+1006	BL Lac	326.38	10.12	0.048 ± 0.014	1.71 ± 0.19	40.46	67.15	0.9874	2.83
MG2 J174803+3403	J1748.0+3403	FSRQ	267.01	34.06	0.97 ± 0.13	2.31 ± 0.07	284.21	31.63	0.9934	2.76
PKS 0834-20	J0836.5-2026	FSRQ	129.13	-20.45	1.93 ± 0.19	2.94 ± 0.08	171.15	1.15	0.5796	2.75
TXS 0222+185	J0224.9+1843	FSRQ	36.24	18.72	1.72 ± 0.22	3.05 ± 0.12	101.08	2.59	0.5327	2.69
OD 166	J0242.3+1102	FSRQ	40.59	11.05	1.94 ± 0.20	2.59 ± 0.06	252.83	6.91	0.8651	2.68
CRATES J233930	J2339.6+0242	BCU	354.90	2.71	1.00 ± 0.21	2.58 ± 0.11	94.50	6.17	0.8537	2.66
TXS 0907+230	J0910.6+2247	FSRQ	137.67	22.80	1.17 ± 0.14	2.37 ± 0.06	262.58	5.38	0.9578	2.66

Table 2.1. Continued

PMN J1441-1523	J1441.6-1522	FSRQ	220.41	-15.38	0.65 ± 0.23	2.32 ± 0.13	72.02	11.77	0.9535	2.64
CRATES J105433 +392803	J1054.2+3926	BCU	163.56	39.44	0.27 ± 0.09	2.30 ± 0.16	34.05	4.79	0.9000	2.63
MG1 J154930+1708	J1549.6+1710	BL Lac	237.41	17.18	0.17 ± 0.08	2.01 ± 0.16	44.75	17.03	0.9759	2.62
TXS 1448+093	J1450.4+0910	FSRQ	222.62	9.18	0.76 ± 0.13	2.35 ± 0.08	130.24	10.58	0.9599	2.61
PMN J0226+0937	J0226.5+0938	FSRQ	36.63	9.63	0.48 ± 0.12	2.18 ± 0.10	96.49	56.42	0.9523	2.61
PKS 0451-28	J0453.1-2806	FSRQ	73.29	-28.11	5.83 ± 0.17	2.66 ± 0.02	3118.20	10.77	0.9815	2.56
B3 0908+416B	J0912.2+4127	FSRQ	138.06	41.46	1.51 ± 0.14	2.42 ± 0.05	539.57	12.10	0.9903	2.56
TXS 1616+517	J1618.0+5139	FSRQ	244.52	51.67	0.69 ± 0.13	2.68 ± 0.12	72.65	12.38	0.8408	2.56
B3 1624+414	J1625.7+4134	FSRQ	246.45	41.57	1.38 ± 0.14	2.49 ± 0.06	395.12	9.69	0.9787	2.55
B3 1343+451	J1345.5+4453 c	FSRQ	206.39	44.88	15.01 ± 0.16	2.25 ± 0.008	34652.7	24.25	0.9994	2.53
PKS 2107-105	J2110.2-1021c	FSRQ	317.56	-10.36	0.88 ± 0.18	2.66 ± 0.13	53.29	5.46	0.6500	2.50

¹ Integrated γ -ray flux in units of $\times 10^{-8}$ photon $\text{cm}^{-2}\text{s}^{-1}$

² Photon energy in GeV.

below the Fermi-LAT band. They are sometimes also called 'MeV' blazars [44], being bright and strong X-ray emitters. In the X-ray band, these sources usually have a hard spectrum which corresponds to the rising part of the HE component, so these data are crucial for investigation of the origin of nonthermal emission [45]. Yet, due to the shift of SED peaks, for some blazars the direct thermal emission from the accretion disc is visible in the optical-UV band (the big blue bump) which can be modeled to derive the accretion disc luminosity [46] and the black hole mass and so to understand the properties of the central source. So, the Neil Gehrels Swift Observatory ([47], hereafter Swift), taking the data in Optical/UV and X-ray bands, is an ideal instrument (within its sensitivity limit) for observing distant blazars.

Even though in the γ -ray band the distant blazars are relatively faint as compared with the X-ray band, Fermi-LAT observations are still crucial. The γ -ray band corresponds to the falling part of the HE component which combined with the X-ray data will fully constrain the second peak in the SED. This is fundamental allowing to derive the physical parameters of the jets. The multiwavelength observations and theoretical interpretations are a regular approach and

Table 2.2: Spectral parameters of the sources modeled with log-parabola.

Object	F_{γ}^1	α	β
PKS 1351-018	$(6.86 \pm 1.66) \times 10^{-9}$	2.20 ± 0.23	0.63 ± 0.23
PKS 0537-286	$(4.15 \pm 0.20) \times 10^{-8}$	2.66 ± 0.04	0.10 ± 0.03
TXS 0800+618	$(2.04 \pm 0.16) \times 10^{-8}$	2.67 ± 0.08	0.17 ± 0.06
B2 0743+25	$(1.72 \pm 0.23) \times 10^{-8}$	2.53 ± 0.14	0.40 ± 0.13
PKS 0347-211	$(2.69 \pm 0.17) \times 10^{-8}$	2.32 ± 0.05	0.19 ± 0.03
PKS 0438-43	$(1.15 \pm 0.23) \times 10^{-8}$	2.35 ± 0.12	0.48 ± 0.11
S4 2015+65	$(1.66 \pm 1.00) \times 10^{-9}$	2.42 ± 0.35	0.42 ± 0.31
PKS 0834-20	$(1.76 \pm 0.20) \times 10^{-8}$	2.62 ± 0.16	0.29 ± 0.13
OD 166	$(1.45 \pm 0.24) \times 10^{-8}$	2.43 ± 0.11	0.24 ± 0.08
TXS 0907+230	$(8.68 \pm 1.77) \times 10^{-8}$	2.28 ± 0.09	0.12 ± 0.06
PKS 0451-28	$(5.56 \pm 0.18) \times 10^{-8}$	2.56 ± 0.04	0.09 ± 0.02
B3 1343+451	$(1.41 \pm 0.02) \times 10^{-7}$	2.18 ± 0.01	0.07 ± 0.006

Integrated γ -ray flux in units of $\times 10^{-8}$ photon $\text{cm}^{-2}\text{s}^{-1}$

a unique way of probing the physical condition of the plasma in the jet. From the theoretical modeling point of view, distant blazars are excellent sources for studying accretion disc-jet connection in the early epoch of quasar formation as well as for probing the environments around supermassive black holes.

Identification of distant blazars and their investigation has always been one of the actively discussed topics in the blazar research (e.g., [48, 49, 50, 51, 52, 53, 54, 55, 56, 57]). In contrast to nearby blazars, good quality multiwavelength data are missing for the high redshift blazars, which significantly complicates their detailed study. However, due to improved sensitivity of the instruments (e.g., X-ray and γ -ray observatories) and wide-field surveys in the low energy bands (e.g., Sloan Digital Sky Survey) [58] or WISE [59]) the number of high redshift blazars with sufficient multiwavelength data has been significantly increased. Along with continuous γ -ray observations of some distant blazars since 2008 this opens new

perspectives for exploring the physics of distant blazars.

Motivated by the large number of detected high redshift γ -ray emitting blazars, with the aim to characterize their multiwavelength emission properties, we perform an intense broadband study of all the thirty-three known γ -ray blazars beyond redshift 2.5. Using the improved Pass 8 data set which is more suitable for studying weak sources, we perform a detailed spectral and temporal analysis of Fermi-LAT γ -ray data accumulated during 2008-2018. The γ -ray flux variation, not well explored for distant blazars, is investigated for the considered 10 years, using an improved adaptive binning method. To characterize the physical properties of the considered sources in the X-ray and optical/UV bands, the data from their observation with both Swift X-ray Telescope (XRT) and Ultraviolet and Optical Telescope (UVOT) in the previous 15 years are analyzed. This allows to collect unprecedented data in the optical/UV, X-ray and γ -ray bands, which is used to constrain the multiwavelength SEDs. Then, through theoretical modeling of these SEDs, the physical parameters characterizing the sources (disc luminosity, black hole mass, etc.) and their jets (e.g., the distribution of underlying electrons, magnetic field, power, etc.) are derived, allowing a quantitative discussion and investigation of the state of plasma in these powerful jets. Taking into account the large number of the considered sources (33) and the amount of analyzed data, this is one of the most comprehensive studies of most distant and powerful blazars.

2.2 THE SAMPLE

The fourth catalog of AGNs detected by Fermi-LAT contains more than 2863 AGNs detected above the 5σ limit [36]. A small fraction of them (1.18 per cent) are distant blazars $z > 2.5$ (~ 20.7 Gpc), including 26 FSRQs, two BL Lacs and five blazars of uncertain type (BCU). The coordinates, redshift and synchrotron peak classification of these sources are given in Table 2.1. The most distant source at $z = 4.31$ is the FSRQ GB 1508+5714, whereas the BL Lacs 87 GB 214302.1+095227 and MG1 J154930+1708 are at $z = 2.83$ and $z = 2.62$, respectively, which is interesting, since due to low γ -ray luminosity BL Lacs are rarely observed at these distances. In this study, the data collected by Fermi-LAT and Swift are analyzed to study the multiwavelength emission from high redshift blazars ($z > 2.5$) selected from the fourth catalog of AGNs detected by Fermi-LAT which are presented in Table 2.1.

Here, we assume the following standard cosmological parameters of $H_0 = 71 \text{ km s}^{-1} \text{Mpc}^{-1}$ and $\Omega_\Lambda = 0.730$ [60].

2.3 FERMI-LAT OBSERVATIONS

The Fermi-LAT data used in the current study had been accumulated during the first 10 years of operation, from 2008 August 4 to 2018 August 4. The PASS 8 events from a circular region with a radius of 12° around each source in the energy range from 100MeV to 500GeV were downloaded and analyzed with the Fermi Tools (1.2.1) using P8R3 instrument response functions. Good data and time intervals were selected using *gtselect* and *gtmktime* tools (with selection cuts ‘*Event class =128*’ and ‘*evtype =3*’) using maximum zenith angle value of 90° to avoid the γ -ray detection from the earth's limb. Using *gtbin* tool, the events are binned into $16.9^\circ \times 16.9^\circ$ a square region of interest (ROI) with pixels of $0.1^\circ \times 0.1^\circ$ and into 37 equal logarithmically spaced energy bins. The model file of each source (point-like sources included in the ROI and background) is generated using the 4FGL-DR2 version of the 4FGL which is based on 10 years of survey. The model file includes all 4FGL sources falling within the ROI $+5^\circ$ region. The *gll_iem_v07* and *iso_P8R3_SOURCE_V2_v1* models are used to parameterize the Galactic and extragalactic diffuse emission components. The spectral parameters set for the sources located within the ROI are allowed to be free in the analysis. The normalization parameters for the two diffuse components were also kept free.

The spectral analysis was performed using the binned maximum-likelihood method implemented in the *gtlike* tool. The source detection significance is estimated using the test statistic (TS) [61] defined as $TS = 2 \times (\log L_1 - \log L_0)$, where L_1 is the likelihood of the data with a point source at the given position and L_0 without the source. The γ -ray spectral models of each considered source were assumed to be the same as in the 4FGL, and for those with a log-parabola an additional fit with the power law model was performed. The spectra were calculated by separately running *gtlike* for smaller energy intervals equal in logarithmic space. Then, using the *gtsrcprob* tool and the model file obtained from the likelihood fitting, the energy of the highest-energy photon detected from the direction of each source is computed.

γ -RAY VARIABILITY: The γ -ray light curves are calculated using the unbinned likelihood analysis method implemented in the *gtlike* tool. The spectra of the considered sources were

modeled by a power-law which can provide a good representation of the data over the small bins of time. The normalization and photon index of the sample sources are allowed to vary while the photon indexes of all background sources within the ROI are fixed to their best values obtained from the fit of the entire 10-yr data set. As the diffuse background emission should not be variable, the parameters of the background models are fixed as well. During the fitting, the events within 0.1 – 300 GeV with the appropriate quality cuts mentioned above are considered.

Initially, in order to study the variability, the γ -ray light curves with 30-d binning are calculated for all sources, considering the 0.1 – 300 GeV range. Additional light curves with short periods (days or a week) were computed for the statistically significant ($\geq 5\sigma$) γ -ray emitting periods identified in the monthly light curves. Next, using the adaptively binned method of Lott et al. [62], the γ -ray variability is studied further. At fixed time binning, when long time intervals are used, a possible fast flux variation will be smoothed out, while using short bins might result in many upper limits during the low-activity periods. In the adaptive binning approach, the time bin widths are adjusted to produce bins with constant flux uncertainty above the optimal energy (E_0) and this approach is proved to be a powerful method to search for γ -ray flux variation (e.g., [63, 64, 65, 66, 67, 68, 69]). E_0 depends on the flux and photon index of each source and can be computed following [62]. For the considered sources, adaptive binning light curves with 15 per cent uncertainty are generated.

2.4 SWIFT OBSERVATIONS

Swift is a multifrequency space observatory, designed as a rapid response mission for follow-up observation of γ -ray bursts (GRBs) [47]. Although its primary scientific goal is the observation of GRBs, due to wide frequency coverage, it is suitable for blazar studies. The data from two of the instruments onboard Swift UVOT (170-600 nm [22]) and XRT (0.3-10.0 keV [21]) have been analyzed in the current study. Twenty-nine sources from Table 2.1 (except MRSS 291081526, CRATES J233930+024420, MG1 J154930+1708 and B3 1624+414) were at least once observed by Swift. There are available data from multiple observations of some sources; e.g., B2 0743+25, PKS 0438-43, TXS 0222+185, TXS 1448+093, PMN J0226+0937, TXS 1616+517 and PKS 2107-105 had been observed more than 10 times. The

Swift XRT data analysis was possible to apply only for 22 sources (see Table 2.3) and 26 were detected in at least one of the optical-UV Swift-UVOT filters (see Table 2.4).

Swift UVOT data from all six bands are considered when available: UVW2 (188 nm), UVM2 (217 nm), UVW1 (251 nm), U (345 nm), B (439 nm) and V(544nm). The photometry analysis of all our sources was performed using the standard UVOT software distributed within the HEASoft package (v6.25) and the calibration included in the CALDB (v.20170922). The source counts for each filter are extracted from a circular region with a 5 arcsec radius around the sources, while the background ones from a region with 20 arcsec radius not being contaminated with any signal from the nearby sources. uvotsource tool was used to convert the source counts using the conversion factors provided by Pool et al. [70]. The fluxes were corrected for extinction using the reddening coefficient $E(B - V)$ from the Infrared Science

Table 2.3: Swift XRT data analyses results. For the sources, when several observations were available, they were merged to estimate the averaged X-ray spectra. The sources for which the number of counts was enough to constrain the flux and the photon index in a single observation are marked with an asterisk (*).

Object	$n_H \times 10^{20} \text{ cm}^{-2}$	Γ_X	$\text{Log}(F_{(0.3-10)\text{keV}})$	C-stat./dof
GB 1508+5714	1.56	1.38 ± 0.52	-12.21 ± 0.21	0.58(20)
PKS 0537-286 *	2.20	1.17 ± 0.04	-11.42 ± 0.02	1.28(679)
TXS 0800+618 *	4.67	1.13 ± 0.10	-11.53 ± 0.04	1.08(355)
S4 1427+543	1.17	1.41 ± 0.23	-12.24 ± 0.09	1.1(102)
GB6 J0733+0456	7.72	1.65 ± 0.65	-12.80 ± 0.23	1.33(20)
B2 0743+25 *	4.50	1.15 ± 0.03	-11.30 ± 0.01	1.39(773)
PKS 0347-211	4.23	1.32 ± 0.27	-12.26 ± 0.12	1.24(75)
PKS 0438-43 *	1.41	1.25 ± 0.09	-11.52 ± 0.04	1.4(345)
S4 2015+65	10.6	1.79 ± 0.69	-12.28 ± 0.23	0.91(17)
MG2	3.22	1.36 ± 0.47	-12.35 ± 0.18	0.61(33)
PKS 0834-20 *	6.07	1.07 ± 0.09	-11.67 ± 0.04	1.12(399)
TXS 0222+185 *	9.40	1.11 ± 0.04	-10.93 ± 0.02	1.89(684)
OD 166	8.97	1.86 ± 0.40	-12.37 ± 0.15	0.65(40)
TXS 0907+230	4.68	1.14 ± 0.40	-12.49 ± 0.18	1.26(40)
PMN J1441-1523	7.71	1.86 ± 0.63	-13.10 ± 0.22	0.51(25)
TXS 1448+093	2.11	2.33 ± 0.62	-13.30 ± 0.16	1.04(26)
PMN J0226+0937	6.57	1.49 ± 0.37	-12.83 ± 0.15	0.93(49)
PKS 0451-28 *	2.07	1.55 ± 0.10	-11.42 ± 0.04	0.99(297)
B3 0908+416B	1.42	1.01 ± 0.46	-12.47 ± 0.19	1.11(30)
TXS 1616+517	1.98	1.25 ± 0.33	-12.77 ± 0.14	1.17(59)
B3 1343+451 *	1.78	1.21 ± 0.17	-12.22 ± 0.07	0.85(160)
PKS 2107-105	6.23	1.24 ± 0.29	-12.49 ± 0.12	1.67(72)

Archive¹. In the case of several observations for the same source, the analysis is performed using the same background region but validated that it is not contaminated by nearby objects in any filter. Also, light curves have been generated for investigation of the flux variation in each band. Then, if no significant variation is found, the spectral points are computed from the summed images, resulting in the flux estimation with reduced uncertainties.

The XRT data, taken both in photon counting and window timing modes were analyzed with standard XRTDAS tool distributed within the HEASoft package (v6.25), applying standard procedures, filtering and screening criteria. The source counts were selected from a 20-pixel (47 arcsec) circle centered on the coordinates of each source, while those for the while those for the background- from an annulus with the same center and inner and outer radii of 51(120 arcsec) and 85 pixels (200 arcsec), respectively. The Cash statistics [71] on ungrouped data

Table 2.4: Summary of Swift-UVOT observations of the considered sources. For the sources, when several observations were available, the fluxes in each band are computed from the summed images. Averaged flux in each band is in units of $\text{erg cm}^{-2}\text{s}^{-1}$.

Object	V	B	U	W1	M2	W2
PKS 1351-108	-	-	$(4.54 \pm 2.53) \times 10^{-14}$	-	-	-
MG3 J163554+3629	-	-	$(6.93 \pm 2.72) \times 10^{-14}$	-	-	$(7.50 \pm 4.11) \times 10^{-14}$
PKS 0537-286	$(3.78 \pm 5.86) \times 10^{-15}$	$(4.53 \pm 1.56) \times 10^{-14}$	$(3.54 \pm 0.42) \times 10^{-13}$	$(4.54 \pm 2.54) \times 10^{-14}$	$(6.84 \pm 0.75) \times 10^{-14}$	$(4.61 \pm 0.55) \times 10^{-13}$
TXS 0800+618	$(7.69 \pm 0.12) \times 10^{-15}$	-	$(2.39 \pm 0.6) \times 10^{-13}$	$(5.68 \pm 0.18) \times 10^{-15}$	-	$(6.58 \pm 0.13) \times 10^{-14}$
S4 1427+543	-	$(2.52 \pm 2.03) \times 10^{-14}$	$(2.53 \pm 0.92) \times 10^{-13}$	-	$(3.88 \pm 1.4) \times 10^{-14}$	$(1.50 \pm 0.02) \times 10^{-15}$
GB6 J0733+0456	-	$(2.97 \pm 2.55) \times 10^{-14}$	-	$(9.40 \pm 0.25) \times 10^{-15}$	-	-
B2 0743+25	-	$(4.92 \pm 0.82) \times 10^{-14}$	$(3.39 \pm 0.59) \times 10^{-13}$	-	$(1.12 \pm 0.22) \times 10^{-13}$	$(4.76 \pm 0.76) \times 10^{-13}$
PKS 0347-211	-	-	$(2.80 \pm 0.52) \times 10^{-13}$	-	$(1.69 \pm 0.5) \times 10^{-13}$	$(2.03 \pm 1.09) \times 10^{-13}$
S4 1124+57	$(1.16 \pm 0.85) \times 10^{-14}$	-	-	-	-	-
PKS 0438-43	$(7.90 \pm 0.1) \times 10^{-15}$	-	$(3.45 \pm 0.38) \times 10^{-13}$	-	-	$(8.02 \pm 0.69) \times 10^{-13}$
S4 2015+65	$(1.63 \pm 0.02) \times 10^{-15}$	-	-	$(6.91 \pm 0.33) \times 10^{-14}$	-	-
87 GB	$(1.01 \pm 0.48) \times 10^{-13}$	$(2.49 \pm 0.36) \times 10^{-13}$	-	$(2.78 \pm 0.72) \times 10^{-13}$	$(3.49 \pm 0.63) \times 10^{-13}$	-
214302.1+095227	-	-	-	-	-	-
MG2 J174803+3403	$(1.92 \pm 0.32) \times 10^{-13}$	$(2.53 \pm 0.25) \times 10^{-13}$	$(4.68 \pm 0.87) \times 10^{-13}$	$(2.40 \pm 0.33) \times 10^{-13}$	$(3.73 \pm 0.61) \times 10^{-13}$	$(3.20 \pm 1.52) \times 10^{-13}$
PKS 0834-20	-	-	$(7.82 \pm 0.54) \times 10^{-13}$	$(3.84 \pm 1.72) \times 10^{-14}$	$(2.39 \pm 0.36) \times 10^{-13}$	$(7.29 \pm 0.91) \times 10^{-13}$
TXS 0222+185	-	-	$(9.36 \pm 0.89) \times 10^{-13}$	-	$(8.18 \pm 1.11) \times 10^{-13}$	$(1.12 \pm 0.21) \times 10^{-12}$
OD 166	-	-	-	-	-	$(9.19 \pm 0.36) \times 10^{-14}$
TXS 0907+230	$(9.53 \pm 4.27) \times 10^{-14}$	$(9.66 \pm 3.17) \times 10^{-14}$	$(5.28 \pm 2.66) \times 10^{-13}$	$(8.77 \pm 3.31) \times 10^{-14}$	$(2.09 \pm 1.55) \times 10^{-13}$	-
PMN J1441-1523	-	-	$(6.33 \pm 4.81) \times 10^{-14}$	-	-	-
CRATES	-	-	-	$(1.90 \pm 0.88) \times 10^{-16}$	-	-
J05433+392803	-	-	-	-	-	-
TXS 1448+093	-	-	$(6.53 \pm 2.36) \times 10^{-14}$	-	-	$(1.35 \pm 0.35) \times 10^{-13}$
PMN J0226+0937	$(9.95 \pm 4.17) \times 10^{-14}$	$(5.13 \pm 0.9) \times 10^{-13}$	$(1.22 \pm 0.06) \times 10^{-12}$	$(4.39 \pm 1.53) \times 10^{-13}$	$(1.30 \pm 0.06) \times 10^{-12}$	$(1.26 \pm 0.08) \times 10^{-12}$
PKS 0451-28	-	$(9.52 \pm 1.21) \times 10^{-14}$	-	-	-	-
B3 0908+416B	$(3.45 \pm 0.11) \times 10^{-15}$	$(3.46 \pm 2.22) \times 10^{-14}$	$(2.08 \pm 0.66) \times 10^{-13}$	$(4.94 \pm 1.95) \times 10^{-14}$	$(6.87 \pm 1.91) \times 10^{-14}$	$(2.67 \pm 1.2) \times 10^{-13}$
TXS 1616+517	-	-	$(1.96 \pm 0.27) \times 10^{-13}$	-	-	$(1.25 \pm 0.34) \times 10^{-13}$
B3 1343+451	-	$(3.12 \pm 2.77) \times 10^{-14}$	$(4.54 \pm 0.55) \times 10^{-13}$	$(7.41 \pm 0.23) \times 10^{-15}$	$(2.52 \pm 0.29) \times 10^{-13}$	$(4.47 \pm 0.65) \times 10^{-13}$
PKS 2107-105	-	-	$(1.74 \pm 0.1) \times 10^{-12}$	-	-	$(1.44 \pm 0.13) \times 10^{-12}$

¹ <http://irsa.ipac.caltech.edu/applications/DUST/>

was used, as for many observations the number of counts was low and did not contain the minimum number of counts required for Gaussian statistics. The 0.3-10 keV X-ray spectrum of each source is fitted with XSPEC 12.10.1 adopting an absorbed power-law model with a neutral hydrogen column density fixed to its Galactic value in each direction.

Initially, for the considered sources, the X-ray spectral analysis was performed for each observation. However, for most of the sources, the count rate was below 20, preventing spectral fitting, and the photon index and flux could be estimated only for a few bright sources. Then, when several observations of the same source were available, they were merged to increase the photon statistics, and the averaged X-ray spectra were obtained. The merging was done using the tool available from the UK Swift Science Data Centre² [72]. Again, XSPEC was used to fit the 0.3-10 keV spectrum, testing both the absorbed power-law and log-parabola models. We note that the spectra of many sources could be constrained only by merging the observations.

2.5 RESULTS OF DATA ANALYSES

The γ -ray data analysis results obtained from the power-law fit in the range from 100 MeV to 500 GeV are presented in Table 2.1 for each source, providing the γ -ray flux (F_γ), photon index, the detection significance (TS), the energy of the highest energy events (E_{\max}) detected from each object with the probability of its association with the target. The sources are detected with $TS > 34.05$ significance, except for S4 2015+65, which appeared with $TS = 23.77$. B3 1343+451 is detected with the highest significance of $TS = 34652.79$ (186.15σ), allowing to perform a detailed spectral and variability analysis. In addition, for the sources with the spectra modeled by a log-parabola in 4FGL, an additional fit with a log-parabola model was performed, the results of which are presented in Table 2.2. The curvature of the spectra of PKS 1351-018, B2 0743+25, PKS 0438-43, S4 2015+65, PKS 0834-20, and OD 166 is substantial ($\beta = 0.24 - 0.63$), so their γ -ray spectrum quickly declines. The flux estimated from the power-law fitting which yielded soft γ -ray spectra as well does not substantially differ from that obtained with a log-parabola. The only noticeable difference is

² https://www.swift.ac.uk/user_objects/

found for PKS 1351-018; the flux estimated from the log-parabola fitting is $(6.86 \pm 1.66) \times 10^{-9}$ photon $\text{cm}^{-2}\text{s}^{-1}$ as compared with $(1.11 \pm 0.15) \times 10^{-8}$ photon $\text{cm}^{-2}\text{s}^{-1}$ when the spectrum was modeled by a power-law. However, for this source $\beta = 0.63 \pm 0.23$ was estimated implying its spectrum is curved significantly. Interestingly, the log-parabola fitting of S4 2015+65 spectrum resulted in detection of the source with TS = 27.96.

The results presented in Table 2.1 are shown in Figure 2.1. The γ -ray photon index versus flux (estimated from power-law fitting) is shown in the upper left panel, where the FSRQs are circles, BL LACs triangles and BCUs squares. Even though the number of sources is not enough for population studies, some difference in various blazar types can be seen. The photon index ($\sim E^{-\Gamma_\gamma}$) estimated in the 0.1-500 GeV range ranges from 1.71 to 3.05 with a mean of 2.54. The soft γ -ray spectra of the considered sources (except 87GB 214302.1+095227 and MG1 J154930+1708) indicate that the peak of the HE component in their SED is in the MeV range. The flux of considered sources ranges from 4.84×10^{-10} to 1.50×10^{-7} photon $\text{cm}^{-2}\text{s}^{-1}$. The two BL Lacs detected beyond $z = 2.5$, 87GB 214302.1+095227 and MG1 J154930+1708, have the lowest flux, $(4.84 \pm 1.37) \times 10^{-10}$ photon $\text{cm}^{-2}\text{s}^{-1}$ and $(1.66 \pm 0.79) \times 10^{-9}$ photon $\text{cm}^{-2}\text{s}^{-1}$, respectively, but they have a harder γ -ray spectrum. The γ -ray photon index of 87GB 214302.1+095227, which is the only ISP object among the selected sources, is 1.71 ± 0.19 and that of MG1 J154930+1708 is $\Gamma_\gamma = 2.01 \pm 0.16$. The γ -ray flux of BCUs included in the sample ranges from 2.19×10^{-9} photon $\text{cm}^{-2}\text{s}^{-1}$ to 1.46×10^{-8} photon $\text{cm}^{-2}\text{s}^{-1}$ with Γ_γ within 2.20 – 2.84. The FSRQs occupy the region of high flux $\geq 3.89 \times 10^{-9}$ photon $\text{cm}^{-2}\text{s}^{-1}$ and $\Gamma_\gamma \geq 2.2$ with a mean $F_\gamma \simeq 2.11 \times 10^{-8}$ photon $\text{cm}^{-2}\text{s}^{-1}$. The highest γ -ray flux of $(1.50 \pm 0.02) \times 10^{-7}$ photon $\text{cm}^{-2}\text{s}^{-1}$ was observed from the bright FSRQ B3 1343+451.

The highest energy events (E_{max}) along with the probability of being associated with the sources are given in Table 2.1. As the sources mostly have a soft γ -ray spectrum or the γ -ray data are better modeled by a log-parabola, their γ -ray spectra do not extend to HEs and the photon energies are below 20 GeV; except for 87GB 214302.1+095227, MG2 J174803+3403, PMN J0226+0937 and B3 1343+451 from which photons with 67.15, 31.63, 56.42 and 24.25

GeV have been detected.

The flux, which is a function of the distance, is compared for each source in Figure 2.1 (upper left panel). Even though it is informative, the total energy released from each source cannot be investigated. Next, using the observed flux (F_γ) and photon index (Γ_γ), the luminosity of each source is computed as:

$$L_\gamma = 4\pi d_L^2 \frac{\Gamma_\gamma - 1}{\Gamma_\gamma - 2} \frac{E_{max}^{2-\Gamma_\gamma} - E_{min}^{2-\Gamma_\gamma}}{E_{max}^{1-\Gamma_\gamma} - E_{min}^{1-\Gamma_\gamma}} F_\gamma \quad (2.1)$$

where $E_{min} = 100$ MeV and $E_{max} = 500$ GeV. Figure 2.1 (upper right panel) shows the distribution of the considered sources in the $\Gamma_\gamma - L_\gamma$ plane. The γ -ray luminosity of considered sources ranges from 1.01×10^{47} erg s $^{-1}$ to 5.54×10^{48} erg s $^{-1}$. The lowest luminosity of $(1.01 \pm 0.38) \times 10^{47}$ erg s $^{-1}$ has been estimated for CRATES J105433+392803 which is of the same order with that of the two BL Lacs included in the sample; $(1.42 \pm 0.98) \times 10^{47}$ erg s $^{-1}$ for 87GB 214302.1+095227 and $(1.24 \pm 0.59) \times 10^{47}$ erg s $^{-1}$ for MG1 J154930+1708. The luminosity of these BL Lacs corresponds to the highest end of the luminosity distribution of BL Lacs included in the fourth catalog of AGNs detected by Fermi-LAT (Fig. 10 in [73]). The γ -ray luminosity of only PKS 0347-211, PKS 0451-28, PKS 0537-286 and B3 1343+451 exceeds 10^{48} erg s $^{-1}$ with the highest γ -ray luminosity of $(5.54 \pm 0.06) \times 10^{48}$ erg s $^{-1}$, estimated for B3 1343+451. Naturally, as compared to the distribution of all γ -ray emitting BL Lacs and FSRQs in the $\Gamma_\gamma - L_\gamma$ plane [73], the blazars considered here occupy the highest luminosity range. We note that the luminosities shown in Figure 2.1 (upper right panel) have been computed based on the time-averaged γ -ray flux, and even higher luminosities are expected during γ -ray flares.

Table 2.3 shows the X-ray data analysis results, for each source presenting the neutral hydrogen column density, X-ray photon index (Γ_X), flux, and C-stat/dof. The flux ranges from $\simeq 5 \times 10^{-14}$ erg cm $^{-2}$ s $^{-1}$ to $\simeq 10^{-11}$ erg cm $^{-2}$ s $^{-1}$ the highest flux of $(1.19 \pm 0.04) \times 10^{-11}$ erg cm $^{-2}$ s $^{-1}$ being observed for TXS 0222+185 ($z = 2.69$).

Interestingly, from the sources considered here, only FSRQs are detected in the X-ray band; among BL Lacs, there are no observations for MG1 J154930+1708, while for 87GB 214302.1+095227, even after merging six observations, only 10 counts are detected. Also,

BCUs included in Table 2.1 have not been detected in the X-ray band.

The X-ray flux is plotted versus the photon index in the lower left panel of Figure 2.1. For several sources, the number of detected counts was not high enough, so the flux and photon index were estimated with large uncertainties. The X-ray photon index of considered sources is < 2.0 , implying the X-ray spectra have a rising shape in the $\nu F_\nu \sim \nu^{2-\Gamma_X}$ representation, which is natural as LSP blazars are considered. The only exception is TXS 1448+093 with $\Gamma_X = 2.33 \pm 0.62$, but even when merging its all 26 observations, the observed counts were only 25. This source is relatively faint in the X-ray band with a flux of $(5.01 \pm 1.85) \times 10^{-14}$ erg cm $^{-2}$ s $^{-1}$, so even an exposure of 2.39×10^4 sec is not enough to detect a reasonable number of counts. B3 0908+416B has the hardest X-ray spectrum with $\Gamma_X = 1.01 \pm 0.46$. In the $F_X - \Gamma_X$ plane, PKS 0451-28, TXS 0222+185, PKS 0834-20, PKS 0537-286, TXS 0800+618, B2 0743+25 and PKS 0438-43 are detached from the other sources flux of TXS

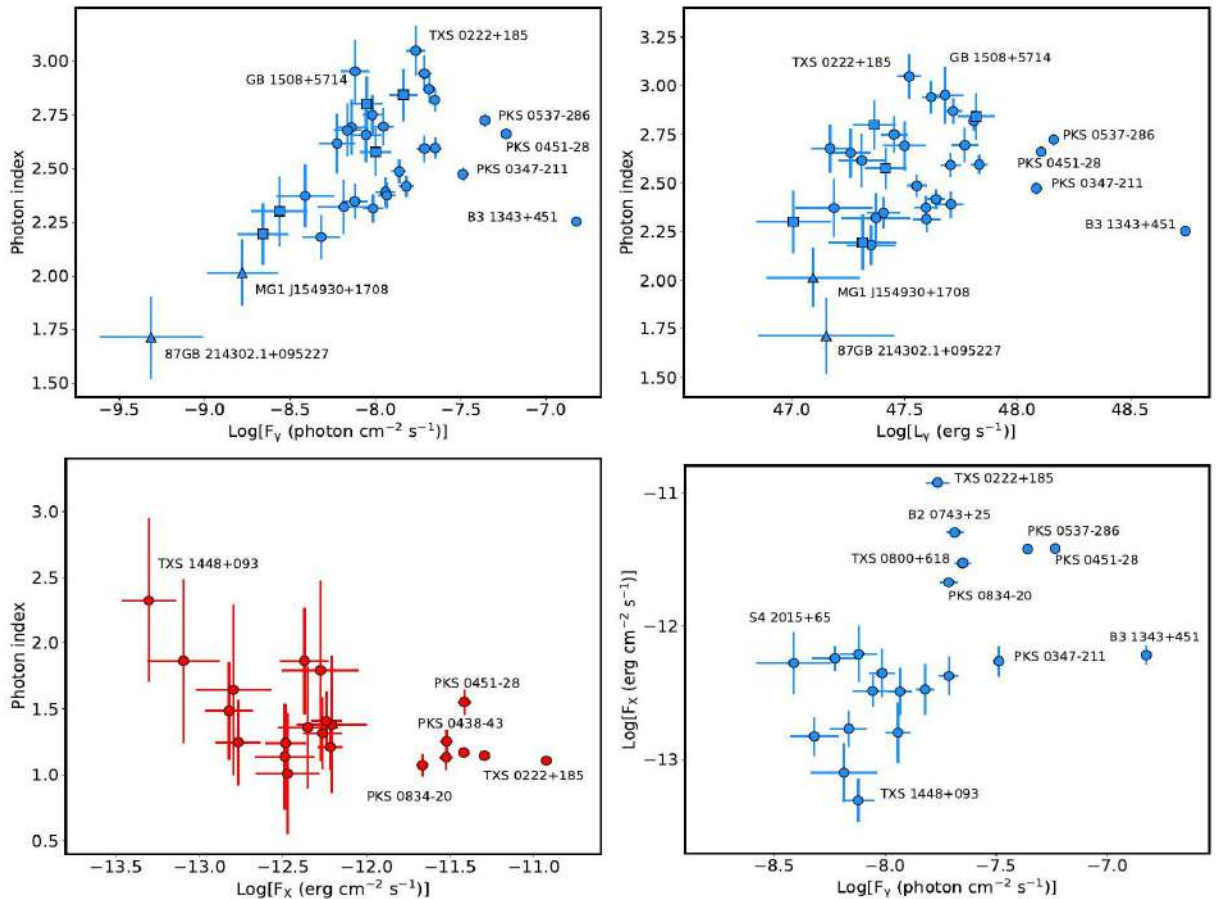


Figure 2.1 The γ -ray flux (> 100 MeV) and luminosity of considered sources versus the photon index are shown in the upper panels. BL lacs, FSRQs and BCUs are shown with triangles, circles, and squares, respectively. Lower left panel: The X-ray flux (0.3-10 keV) versus the photon index. Lower right panel: Comparison of γ -ray and X-ray (if available) fluxes.

because they have a comparably high X-ray flux, $F_{X\text{-ray}} \geq 2.13 \times 10^{-12} \text{ erg cm}^{-2}\text{s}^{-1}$. In the lower right panel of Figure 2.1 the γ -ray and X-ray (if available) fluxes of the considered sources are compared. Interestingly, the bright γ -ray sources PKS 0537-286 and PKS 0451-28 appear to be also bright X-ray emitters. The other bright γ -ray blazars (e.g., B3 1343+451, PKS 0451-28) do not have any distinguishable feature in the X-ray band, having a flux and photon index similar to those of the other considered sources. The bright X-ray sources TXS 0222+185, B2 0743+25, TXS 0800+618, and PKS 0834-20 appear with a similar flux in the γ -ray band, $F_{\gamma} = (1.72 - 2.23) \times 10^{-8} \text{ photon cm}^{-2}\text{s}^{-1}$.

The Swift UVOT data analysis was performed in all available filters. The results are consistent when different background regions are selected. Initially, all the single observations of the sources were analyzed to search for variability. However, the sources are relatively faint in the optical/UV bands and the large uncertainties in the flux estimation do not allow to investigate flux variation in time. Table 2.4 summarizes the results of the UVOT data analysis after merging the observations for each source, presenting the fluxes in the six UVOT filters (if available) with errors. In the SED of GB 1508+5714, PKS 1351-108, PKS 0537-286, TXS 0800+618, S4 1427+543, GB6 J0733+0456, B2 0743+25, PKS 0347-211, S41124+57, PKS 0438-43, S4 2015+65, PKS 0834-20, TXS 0222+185, TXS 0907+230, PMN J0226+0937, PKS 0451-28 and PKS 2107-105, a thermal blue-bump component can be seen, which may represent the emission directly from the disc [74].

X-RAY VARIABILITY: The X-ray flux variability of some sources observed by Swift multiple times have been investigated. The data from each observation were processed and analyzed, but only for eight objects (marked with asterisks in Table 2.3) the number of counts was enough to constrain the flux and the photon index in a single observation. Except for PKS 0438-43, B2 0743+25 and TXS 0222+185, the X-ray emission appeared to be relatively constant, though the sources were observed in different years. For example, the X-ray flux of PKS 0537-286 was $(4.18 \pm 0.74) \times 10^{-12} \text{ erg cm}^{-2}\text{s}^{-1}$ and $(4.53 \pm 0.89) \times 10^{-12} \text{ erg cm}^{-2}\text{s}^{-1}$ on 26 October, 2006 and 12 May 2017, respectively. Fitting the flux observed in different years with a constant flux, the χ^2 test results in $P(\chi^2) = 0.38$ and $\chi^2/\text{dof} = 1.07$ which are consistent with no variability. Similarly, the χ^2 test shows that the X-ray

0800+618, PKS 0834-20, PKS 0451-28 and B3 1343+451 is constant over different years. There is a marginal evidence ($P(\chi^2) = 0.038$ and $\chi^2 / \text{dof} = 1.68$) that the X-ray flux of TXS 0222+185 is variable; it is mostly around $(0.96 - 1.1) \times 10^{-11} \text{ erg cm}^{-2}\text{s}^{-1}$ which increased to $(1.62 \pm 0.13) \times 10^{-11} \text{ erg cm}^{-2}\text{s}^{-1}$ and $(1.37 \pm 0.16) \times 10^{-11} \text{ erg cm}^{-2}\text{s}^{-1}$ on 24 December 2014 and 31 July 2006, respectively. Instead, the χ^2 test shows that the X-ray emission of PKS 0438-43 and B2 0743+25 is variable with $P(\chi^2) < 5.1 \times 10^{-6}$. PKS 0438-43 was in a bright X-ray state on 15 December 2016 with a flux of $(1.09 \pm 0.16) \times 10^{-11} \text{ erg cm}^{-2}\text{s}^{-1}$ as compared with the flux of $(1.30 \pm 0.31) \times 10^{-11} \text{ erg cm}^{-2}\text{s}^{-1}$ in the quiescent state. Similarly, the X-ray flux of B2 0743+25 in the high state on 01 January 2006 was $(1.06 \pm 0.56) \times 10^{-11} \text{ erg cm}^{-2}\text{s}^{-1}$. The variation of the 0.3-10 keV X-ray flux of PKS 0438-43, B2 0743+25 and TXS 0222+185 is shown in Figure 2.4. No variation of X-ray photon index was found, due to the large uncertainties in its estimation.

γ -RAY VARIABILITY: The continuous observation of the considered sources by Fermi-LAT allows a detailed investigation of their γ -ray flux variation during the considered 10 yr. When the source detection significance is $< 10\sigma$, the data are not enough for variability searches in month scales. Their emission could be variable in longer scales (6 or 12 months) more common for non-blazar AGNs [65], which is not investigated here. Initially, the light curves of all sources were calculated with the help of an adaptive binning method. However, the adaptively binned intervals were possible to compute only for the source with a detection significance of $> 37\sigma$. The adaptively binned light curves of B3 1343+451, PKS 0451-28, PKS 0347-211 and PKS 0537-286 computed above $E_0 = 163.9, 163.2, 187.4$ and 151.0 MeV , respectively, are shown in Figure 2.2. B3 1343+451 is the brightest and most variable source in the sample, and in its adaptively binned light curve (Figure 2.2 a) several bright γ -ray emission periods can be identified: around MJD 55100, MJD 55890, MJD 56170, MJD 56640 and MJD 57060. During the bright γ -ray flaring periods, the flux changes in sub-day scales; there are 200 adaptive bins with a high flux and a width shorter than a day; the minimum adaptively binned time width is 6.33 hours observed on MJD 56176.34 when the source flux was $(7.52 \pm 1.85) \times 10^{-7} \text{ photon cm}^{-2}\text{s}^{-1}$ (above 163.9 MeV). Moreover, the width of 83 bins from these 200 is even shorter than 12 hours, which were mostly observed during the flares

around MJD 55890 (24 bins) and MJD 56170 (35 bins). In the quiescent state (e.g., before MJD 55800, expect for the flare on MJD 55100) the γ -ray flux of the source is $\simeq (1 - 5) \times 10^{-8}$ photon $\text{cm}^{-2}\text{s}^{-1}$ which is lower than that averaged over 10 years (including the bright flaring states), reported in Table 2.1. The highest γ -ray flux of $(8.77 \pm 2.16) \times 10^{-7}$ photon $\text{cm}^{-2}\text{s}^{-1}$ above $E_0 = 163.9$ MeV with $\Gamma_\gamma = 2.48 \pm 0.29$ was observed on MJD 55891.7 with a detection significance of 9.1σ within a time bin having a width of 8.2 hours. It corresponds to a flux of $(1.82 \pm 0.45) \times 10^{-6}$ photon $\text{cm}^{-2}\text{s}^{-1}$ above 100 MeV which is 36.4 times higher than the γ -ray flux of the source in the quiescent state (before MJD 55800) but the Γ_γ is within the uncertainties of the value given in Table 2.1. During the hardest γ -ray emission period, $\Gamma_\gamma = 1.45 \pm 0.21$ was detected on MJD 56432 with a significance of 7.2σ , which is unusual for this source. Interestingly, there are twelve periods, mostly during the γ -ray flares, when its γ -ray spectrum was hard (≤ 1.70); one such period had been observed on MJD 55900.53 when, within a time bin having a width of 12.90 hours, Γ_γ was 1.64 ± 0.16 with a detection significance of 10.79σ . In the quiescent state, its γ -ray luminosity is $(2 - 4) \times 10^{48}$ erg s^{-1} which increased up to $\sim 1.5 \times 10^{50}$ erg s^{-1} during the bright γ -ray flares (Figure 2.2 (a)).

The most distant source showing a substantial γ -ray flux increase in short periods is PKS 0537-286 at $z = 3.10$ (Figure 2.2 (b)). The flaring activity of this source was first reported in [75] and the rapid (6 and 12 hours) γ -ray flux variations in [51]. During the extreme γ -ray flaring period from MJD 57878.05 to MJD 57881.55, the adaptively binned light curve confirms the intra-day γ -ray flux increases of PKS 0537-286; the adaptive time bin widths are 20.45, 15.96 and 18.90 hr. For comparison, during the flux increase around MJD 55540 and MJD 56390 the minimum time widths are 2.38 and 3.79 d, respectively. The average γ -ray flux of PKS 0537-286 is $(4.38 \pm 0.18) \times 10^{-8}$ photon $\text{cm}^{-2}\text{s}^{-1}$ (Table 2.1), but it significantly increased in MJD 55528-55553, MJD 56264-56400 and MJD 57878.0-57883.4. In the last period, during five consecutive time intervals, the γ -ray flux above 151.0 MeV was higher than 3×10^{-7} photon $\text{cm}^{-2}\text{s}^{-1}$, with a maximum of $(6.58 \pm 1.35) \times 10^{-7}$ photon $\text{cm}^{-2}\text{s}^{-1}$ observed on MJD 57879.2 with a detection significance of 10.57σ . This corresponds to a flux of $(1.29 \pm 0.26) \times 10^{-6}$ photon $\text{cm}^{-2}\text{s}^{-1}$ above 100 MeV. During these

periods, Γ_γ is 2.45 ± 0.23 , 2.64 ± 0.27 , 2.56 ± 0.28 , 2.79 ± 0.34 and 2.91 ± 0.35 , not significantly different from the value reported in Table 2.1 with no spectral hardening, which shows the emission is dominated by the MeV photons. However, during the flares, the luminosity of the source can be as high as $\simeq 4 \times 10^{49}$ erg s⁻¹, putting PKS 0537-286 in the list of the brightest γ -ray blazars.

The adaptively binned light curves of PKS 0347-211 and PKS 0451-28 (Figure 2.2 c and d) show several periods of γ -ray brightening, when a γ -ray flux increase within day scales is observed. For example, the shortest time interval when the flux increases is 2.65 d for PKS 0347-211, and it is 1.56 d for PKS 0451-28. The light curves of both sources reveal several γ -ray flaring periods when the flux substantially increased. For example, on MJD 54757.04 \pm 2.71 the γ -ray flux of PKS 0347-211 above 187.4 MeV was $(1.57 \pm 0.41) \times 10^{-7}$ photon cm⁻²s⁻¹, which corresponds to a flux of $(3.57 \pm 0.93) \times 10^{-7}$ photon cm⁻²s⁻¹ above 100 MeV. In the case of PKS 0451-28, the peak γ -ray flux of $(2.20 \pm 0.50) \times 10^{-7}$ photon cm⁻²s⁻¹ (above 163.2 MeV) was observed on MJD 56968.60 \pm 0.79 with 9.64 σ . This corresponds to a flux of $(3.70 \pm 0.84) \times 10^{-7}$ photon cm⁻²s⁻¹ above 100 MeV. During this period, Γ_γ was 2.06 ± 0.19 .

The light curves generated with the help of the adaptive binning method allowed to identify periods when the flux of some of the sources considered here (Figure 2.2) increased in sub-day or days scales. It should be mentioned that expect for B3 1343+451, the short time scale variability of the other sources cannot be investigated using the regular time binning method, because in a large number of periods only upper limits are derived. Also, because of low statistics, the adaptively binned light curves were possible to compute only for the source presented in Figure 2.2. For the other sources included in Table 2.1 the variability on week and month scales are investigated. In order to identify whether the γ -ray emission is variable or not, a simple χ^2 test was performed [76]; the flux measured in each interval was fitted by a constant flux and the reduced χ^2 and the probability of the flux being constant are computed.

The χ^2 fitting indicated that the γ -ray emission of B3 0908+416B, TXS 0800+618, PKS 0438-43, OD 166 and TXS 0907+230 is variability in week scales while that of MG3 J163554

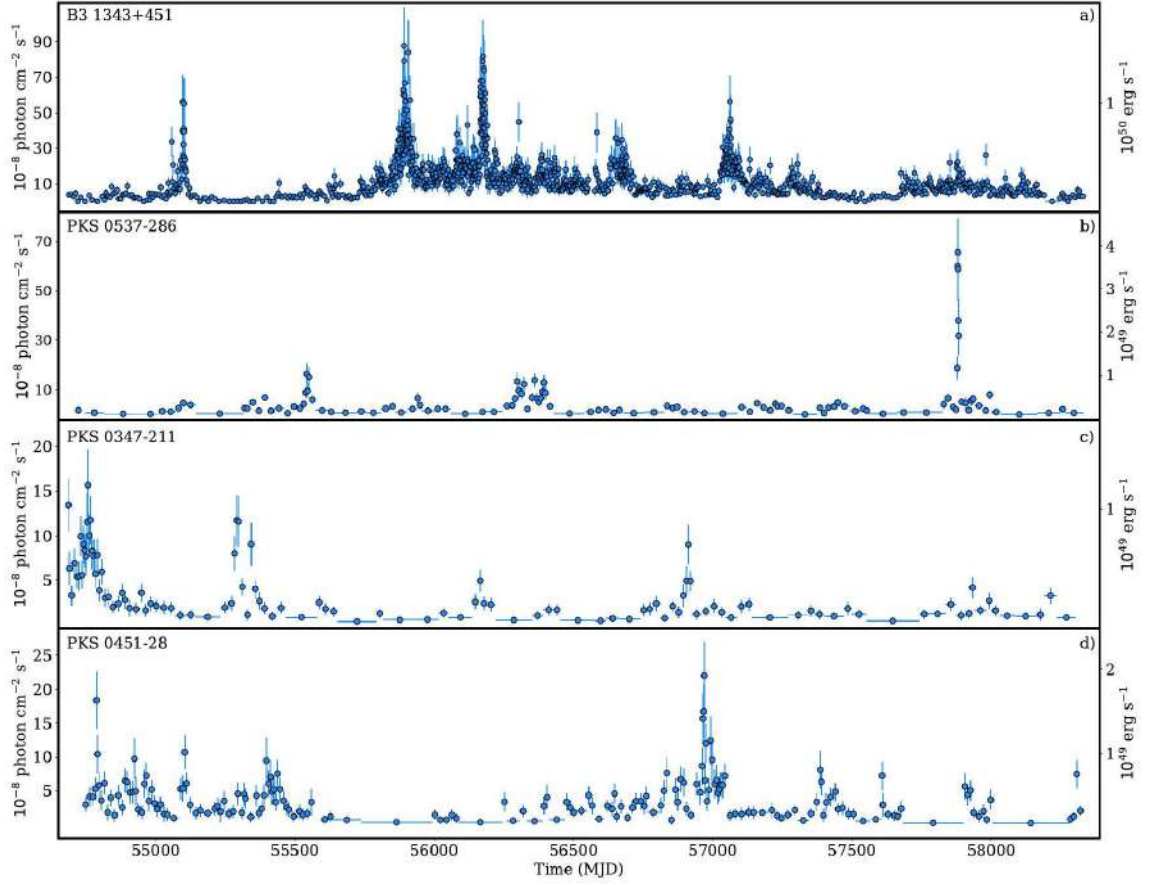


Figure 2.2 γ -ray light curve of B3 1343+451, PKS 0537-286, PKS 0347-211, and PKS 0451-28 for the period from August 2008 to August 2018 calculated using adaptively-binned timescales.

+3629, GB6 J0733+0456, B2 0743+25, PMN J1441-1523 and TXS 1616+517 in month scales. For all these sources, $P(\chi^2) < 2.16 \times 10^{-4}$ was estimated. The γ -ray light curves of these sources with an evident increase in the flux are shown in Figure 2.3. For example, during MJD 57729.16 ± 3.5 and MJD 57736.16 ± 3.5 , the γ -ray flux of PKS 0438-43 above 100 MeV increased 15.2 – 29.3 times as compared to its average flux and was $(3.40 \pm 0.59) \times 10^{-7}$ photon $\text{cm}^{-2}\text{s}^{-1}$ and $(6.57 \pm 0.86) \times 10^{-7}$ photon $\text{cm}^{-2}\text{s}^{-1}$, respectively. Likewise, the 7-d averaged peak values of the γ -ray flux of B3 0908+416B, OD 166, TXS 0800+618 and TXS 0907+230 were $(3.12 \pm 0.37) \times 10^{-7}$ photon $\text{cm}^{-2}\text{s}^{-1}$, $(2.50 \pm 0.45) \times 10^{-7}$ photon $\text{cm}^{-2}\text{s}^{-1}$, $(2.73 \pm 0.39) \times 10^{-7}$ photon $\text{cm}^{-2}\text{s}^{-1}$ and $(1.32 \pm 0.34) \times 10^{-7}$ photon $\text{cm}^{-2}\text{s}^{-1}$, respectively, which exceed the corresponding values given in Table 2.1.

The most distant γ -ray flaring blazar observed so far is MG3 J163554+3629 at $z = 3.65$; this source was reported to be in an active state on 2018 July 7, when its daily averaged peak value of γ -ray flux was $(6.4 \pm 1.15) \times 10^{-7}$ photon $\text{cm}^{-2}\text{s}^{-1}$ [77]. The monthly

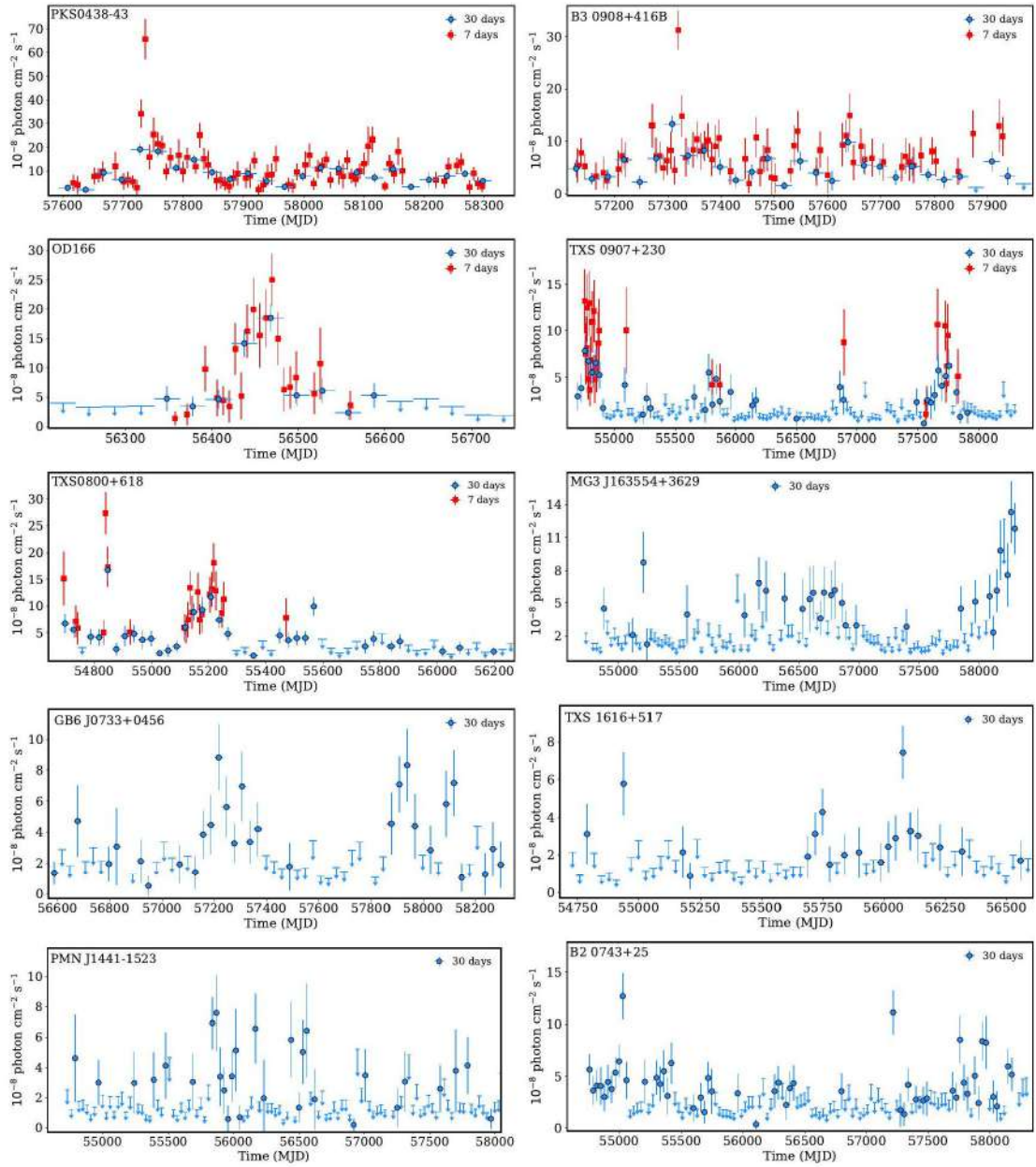


Figure 2.3 7-d (red) and 30-d (blue) binned light curves of PKS 0438-43, B3 0908+416B, OD 166, TXS 0907+230, TXS 0800+618, MG3 J163554+3629, GB6 J0733+0456, TXS 1616+517, PMNJ 1441-1523 and B2 0743+25.

averaged maximum γ -ray flux of $(1.33 \pm 0.28) \times 10^{-7}$ photon $\text{cm}^{-2}\text{s}^{-1}$ was observed on MJD 58267.66 ± 15 (May-June 2018). The source was also bright in γ -rays with a flux of $(1.18 \pm 0.23) \times 10^{-7}$ photon $\text{cm}^{-2}\text{s}^{-1}$ during June-July 2018 when the maximum daily averaged flux was observed [77].

For the considered sources, the γ -ray photon index evolution in time has also been investigated. The photon index is defined by the processes responsible for particle are estimated with large uncertainties which introduces difficulties for investigation of their

variability. Therefore, the γ -ray light curves produced in 30 and 7 d (when available) are used to search for photon index variation, except for B3 1343+451 for which a 3-d binned light curve has been used. Moreover, in the light curves only the periods when the source detection was $TS > 25$ were considered, otherwise the large uncertainties on the photon index estimation would not allow to make definite conclusions. The simple χ^2 test shows that among the considered sources only the photon index of B3 1343+451, PKS 0451-28, B3 0908+416B and TXS 0907+230 varies in time: the variation is highly significant for B3 1343+451 and PKS 0451-28 with $P(\chi^2) = 6.9 \times 10^{-4}$ and $P(\chi^2) \leq 10^{-5}$, respectively, and $P(\chi^2) \simeq 0.015$ for B3 0908+416B and TXS 0907+230. The evolution of the photon index of these sources in time is shown in Figure 2.5 where the horizontal line corresponds to the averaged photon index estimated in ten years (Table 2.1). The photon index of B3 1343+451 clearly varies, the hardest spectrum being observed on MJD 58089.16 \pm 1.5 with $\Gamma_\gamma = 1.73 \pm 0.24$; in total there are 60 periods when $\Gamma_\gamma < 2.0$. Interestingly, the γ -ray spectrum of the source was hard with 1.95 ± 0.07 when it was in a bright γ -ray flaring state on MJD 56172.16 \pm 1.5. The γ -ray spectrum of PKS 0451-28 is usually soft but in the 30-d binned light curve the periods when $\Gamma_\gamma = 2.06 \pm 0.07$ and $\Gamma_\gamma = 2.17 \pm 0.15$ are observed on MJD 56977.66 \pm 15 and 58297.66 \pm 15, respectively. The first period overlaps with the large γ -ray flare evident in the adaptively binned light curve (see Figure 2.2 a). The hardening of the γ -ray spectrum of B3 0908+416B on MJD 57517.66 \pm 15 is remarkable when the Γ_γ changed to 1.84 ± 0.25 compared to 2.42 ± 0.05 averaged over 10 yr. TXS 0907+230 is the most distant object in our sample ($z = 2.66$) with occasional hardening of its γ -ray spectrum. The 7-d binned light curve of TXS 0907+230 shows that there are three periods (on MJD 54798.16 \pm 3.5, 54805.16 \pm 3.5 and 54826.16 \pm 3.5) when its γ -ray emission appears with an unusually hard γ -ray spectrum with $\Gamma_\gamma = 1.72 \pm 0.23$, 1.90 ± 0.21 and 1.72 ± 0.15 . Yet, in the monthly binned light curve, in the bin covering these periods, Γ_γ is 1.88 ± 0.10 with a detection significance of 12.5σ . Even if the γ -ray photon index of MG3 J163554+3629 and PMN J0226+0937 appeared to be constant, hardening of their γ -ray spectra were occasionally observed. For example, for MG3 J163554+3629 $\Gamma_\gamma = 2.29 \pm 0.13$ (with 11.1σ) was observed from MJD 58282 to 58312, likewise, for PMN J0226+0937 Γ_γ was 1.80 ± 0.16 (with 9.7σ) on MJD 54892-54922. The hard γ -ray spectra of the

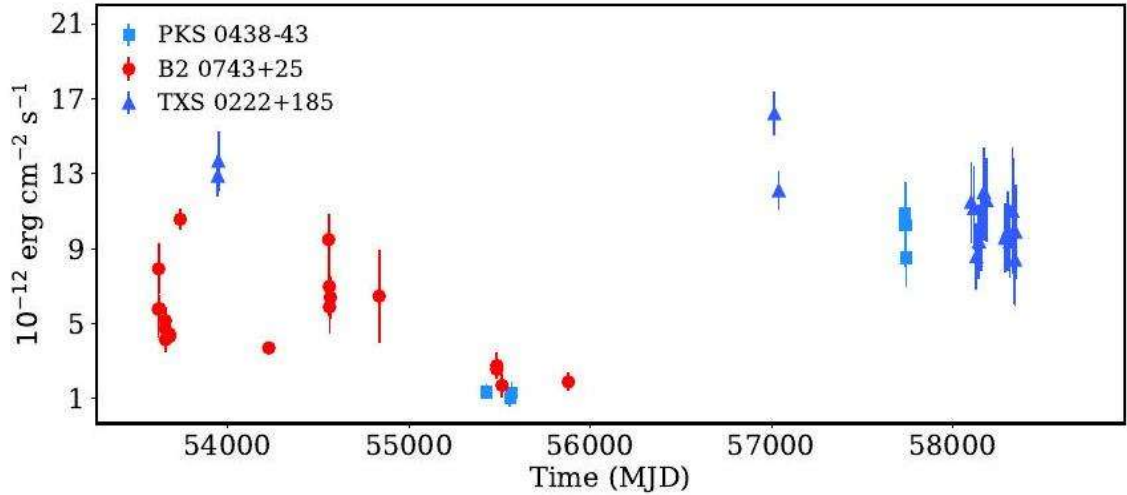


Figure 2.4 The 0.3-10 keV X-ray fluxes of PKS 0438-43, B2 0743+25 and TXS 0222 + 185 measured by Swift-XRT.

sources discussed above are shown in Figure 2.6 in magenta; substantial changes in the γ -ray spectrum are evident.

Such a hard γ -ray spectrum is more typical for BL Lacs, but it has also been occasionally observed for the FSRQs during the flares (e.g., see [78, 64, 67, 79, 57, 80]).

In addition, γ -ray light curves with 30-d binning above 1 GeV are produced to investigate the flux and photon index variation in the GeV band. The periods when the source emission is significant above 1 GeV are also relevant for studying absorption through interaction with EBL photons. There are only a few periods when the considered sources have been detected above 1 GeV with a sufficient significance ($> 5\sigma$). The emission, in these periods, is mostly characterized by a soft γ -ray spectrum, implying these are the same components as those at lower energies. However, the periods when the sources were detected by Fermi-LAT correspond to only a small fraction of the total bins (30-d binning), so the poor statistics did not allow us to investigate the possible flux variation or photon index hardening above 1 GeV.

2.6 THE ORIGIN OF MULTIWAVLENGTH EMISSION

The multiwavelength emission from blazars produced when the accelerated electrons [4, 5, 6, 7, 9, 8] or protons [81, 82, 83, 84, 11, 10, 13, 12] interact with the magnetic and photon fields, contain valuable information necessary for understanding the physics of their jets. The currently proposed models can explain a single SED snapshot, but they cannot self consistently explain the dynamical evolution of the radiation and origin of the flares. The

flares are most likely caused by changes in the radiating particles or in the emission region [85] and their origin can be investigated only with contemporaneous multiwavelength data. During the γ -ray flaring of the considered sources (Figure 2.2 and Figure 2.3), contemporaneous Swift data are available only for PKS 0438-43 and TXS 0800+618. However, the Swift observations in these periods show that the X-ray photon index and flux did not change, being the same as those given in Table 2.3, whereas in the optical/UV bands these sources were detected only in one or two UVOT filters with large uncertainties in the flux estimation. So, it is not clear whether or not the low energy component changed or remained the same during the γ -ray flares. This introduces uncertainties for the theoretical modeling and does not allow to model the SEDs of these two objects during their γ -ray flaring. Moreover, as there are no multiwavelength data during the γ -ray flares of the other sources and our goal is to constrain the main physical parameters of distant blazar jets, only the averaged multiwavelength SEDs have been used in the modeling which represent the typical state of the sources.

To understand the origin of the broadband emission of the considered sources, we have used a simple one-zone leptonic model. In this model, the emission region is assumed to be a spherical blob of radius of R moving in the blazar jet with a bulk Lorentz factor of Γ_j at a viewing angle of θ . The emitting region is filled with a uniformly tangled magnetic field B and with a homogeneous population of relativistic electrons (and positrons), the nonthermal energy distribution of which is described by a power-law with an exponential cut-off at higher energies as:

$$N(\gamma) \sim \gamma^{-\alpha} \exp\left(-\frac{\gamma}{\gamma_{cut}}\right) \gamma > \gamma_{min} \quad (2.2)$$

where γ is the Lorentz factor of electrons in the blob rest frame, and α is the power-law index. γ_{min} and γ_{cut} are the Lorentz factors corresponding to the minimum and cutoff energy of the electron distribution in the emission region. The total energy of the electrons in the emitting region is defined as $U_e = m_e c^2 \int \gamma N_e(\gamma) d\gamma$. The energy distribution of electrons given by Eq. 2.2 is formed when the emitting particles are accelerated with a limiting process at higher energies (e.g., cooling or limited efficiency of the acceleration process). The power-law index (α) defines the properties of the acceleration mechanism [86, 87, 88, 89], and γ_{cut} allows

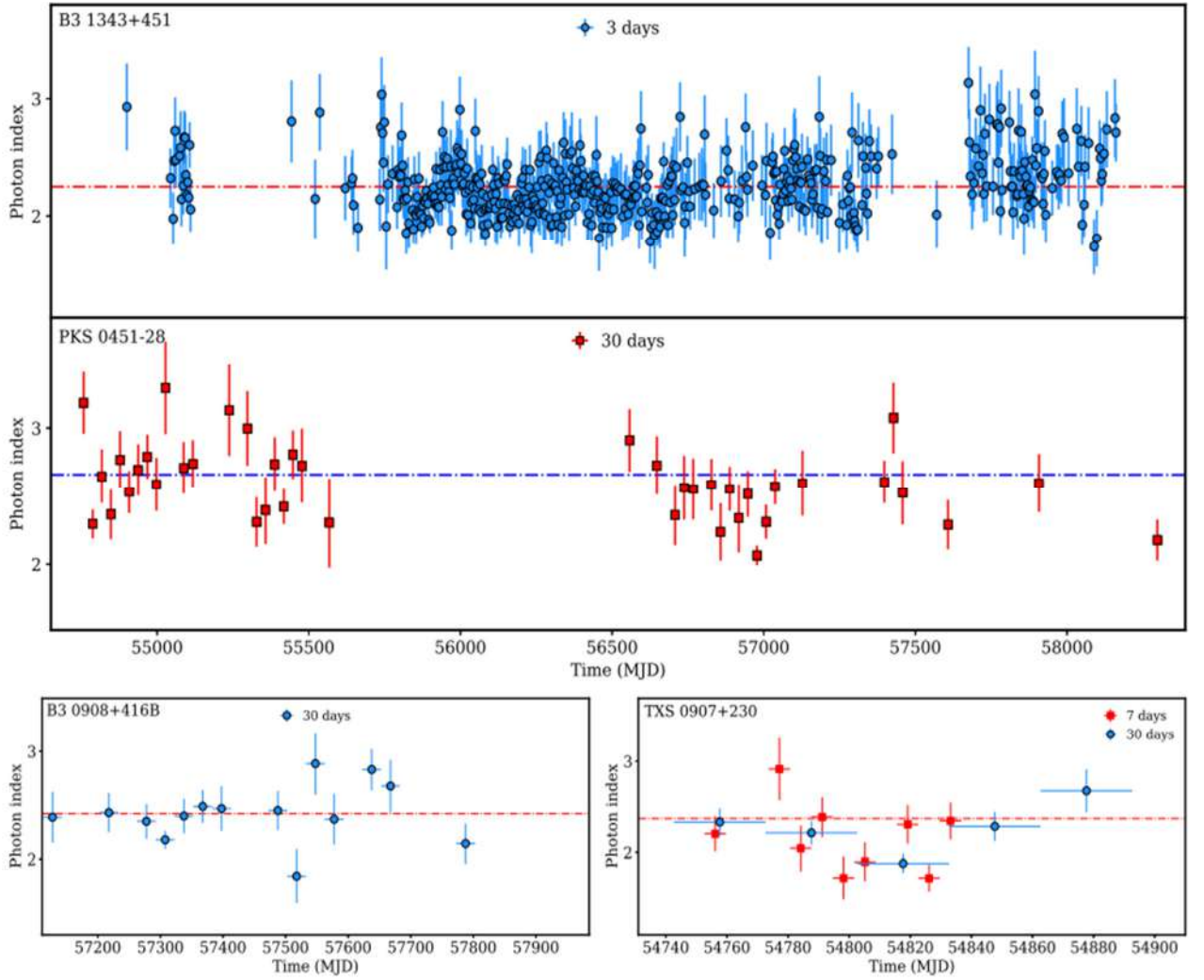


Figure 2.5 The evolution of the γ -ray photon indexes of B3 1343+451, PKS 0451-28, B3 0908+416B and TXS 0907+230 in time.

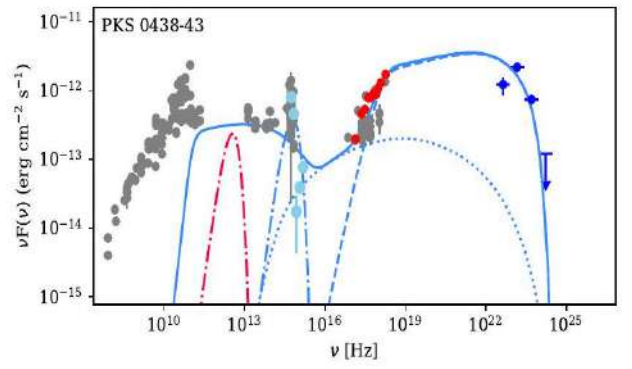
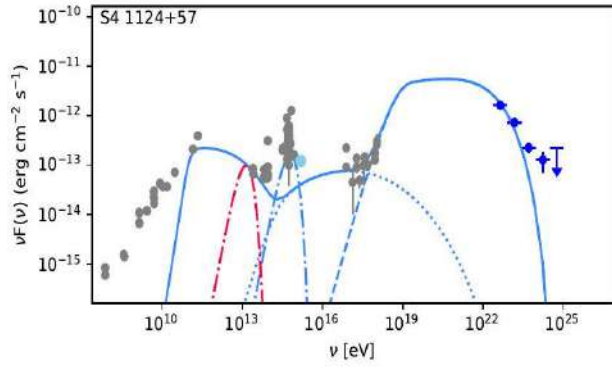
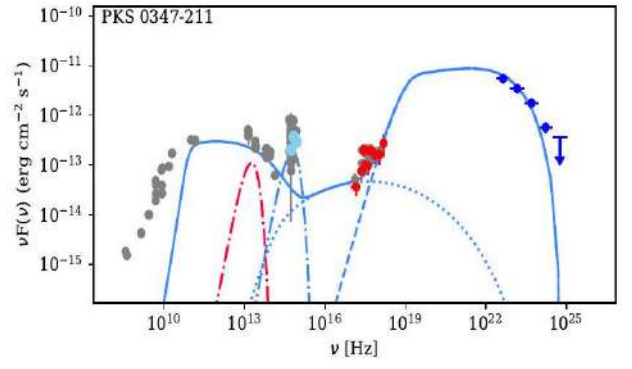
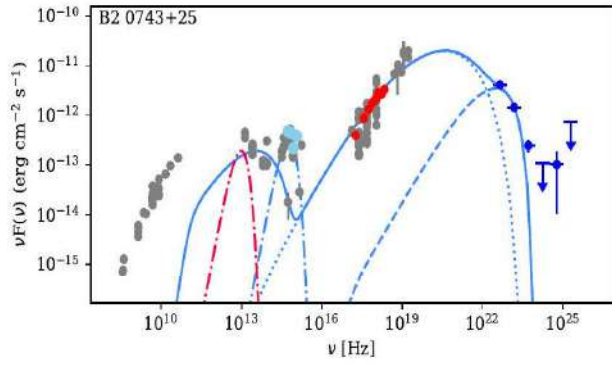
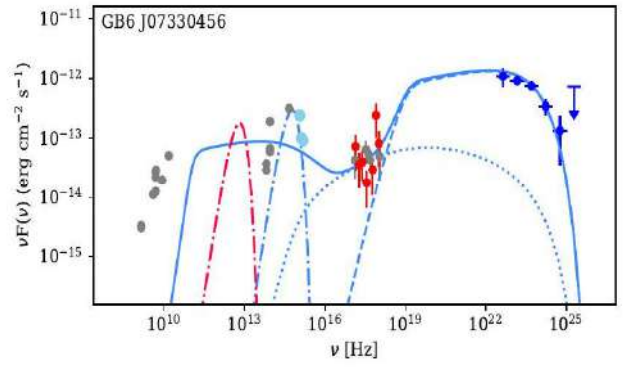
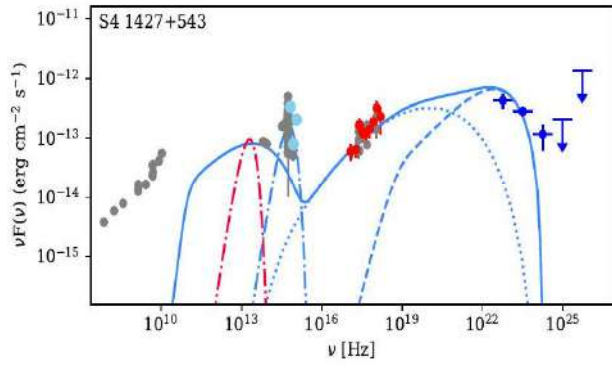
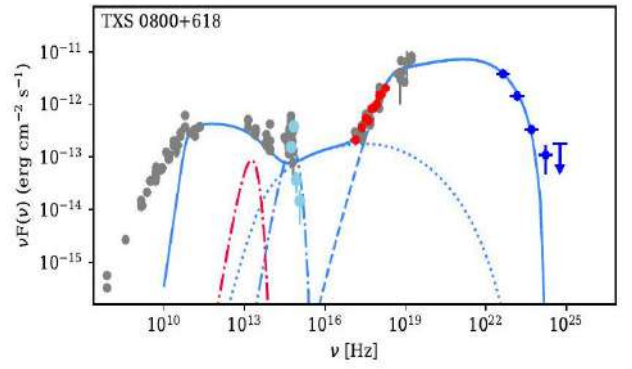
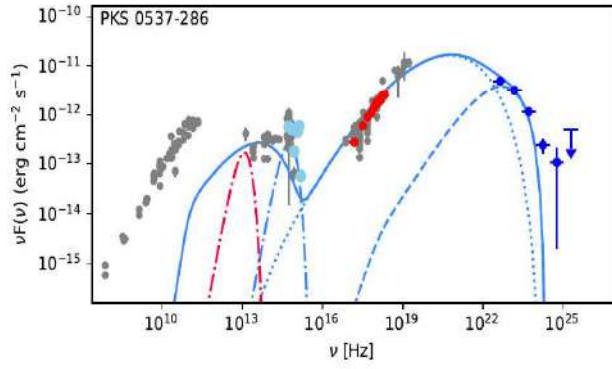
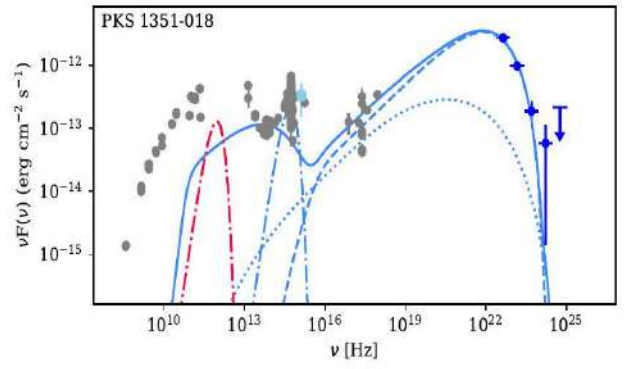
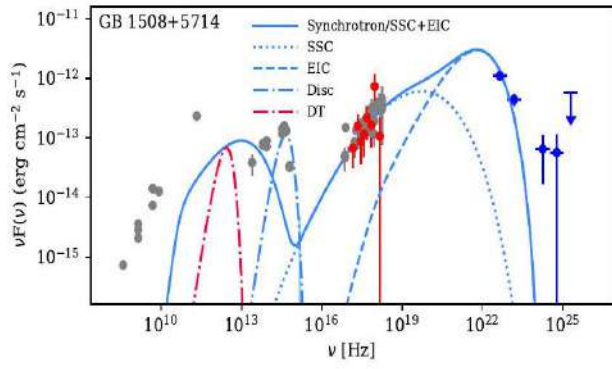
constraining the cooling process of the particles and the state of plasma in the jet [90, 79]. In this interpretation, the parameters of the emitting region are the radius, Doppler factor ($\Gamma = \delta$, for small viewing angles), and magnetic field. The magnetic field is a free parameter during the fitting (assuming its density $B^2/8\pi$ scales with U_e), while in principle a constraint on the other two parameters can be derived from the data. For example, a lower limit on δ can be imposed using high resolution radio data or the emitting region size can be constrained from $R \leq \delta \times c \times t/(1+z)$, provided the minimum variability time is known. Unfortunately, both constraints cannot be assessed for all the sources given in Table 2.1, so both parameters have been left free during the fitting. In this case, R is constrained from the observed Compton Dominance (CD- the IC to the synchrotron peak luminosities ratio) and from

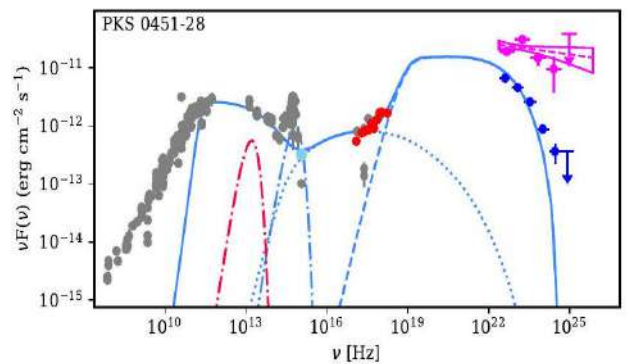
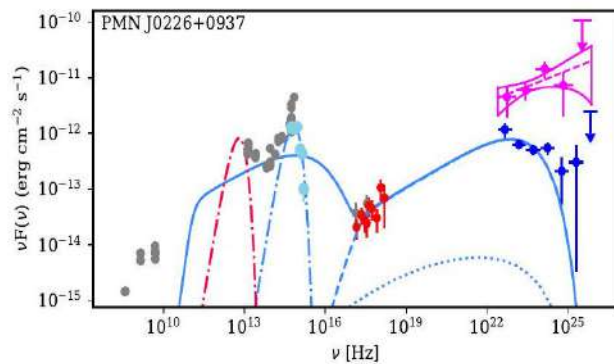
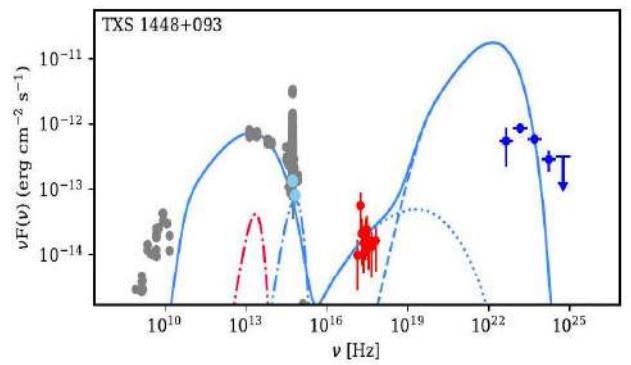
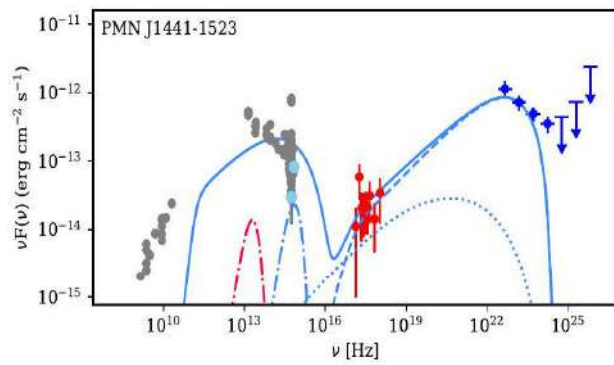
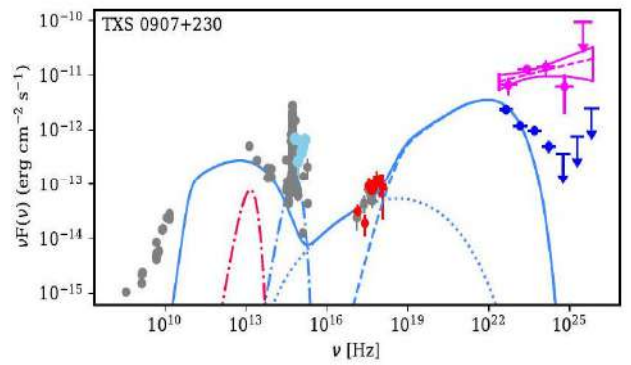
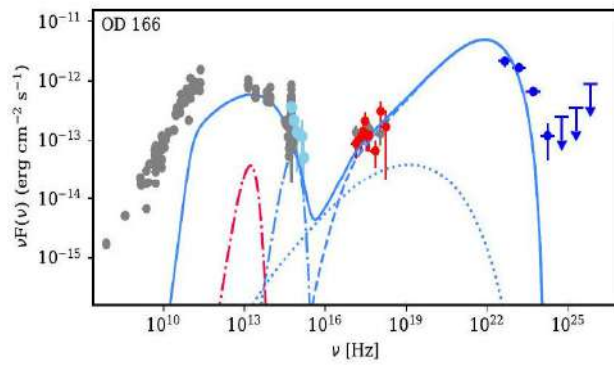
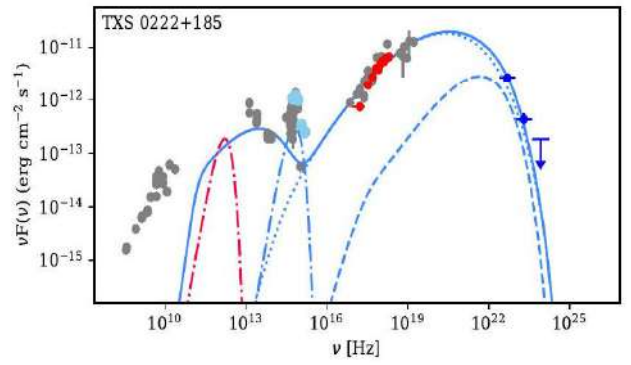
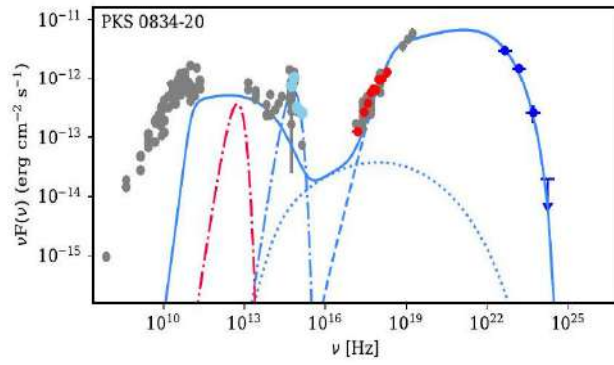
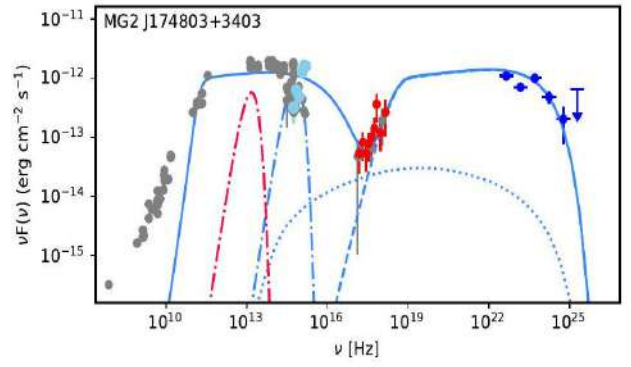
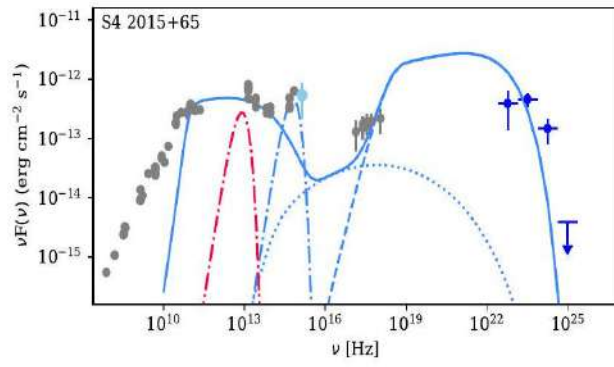
polynomial fitting of the data (see the documentation of JetSet³).

In the modeling it is assumed that the low-energy peak (from radio to optical/UV) is due to synchrotron emission from ultra-relativistic electrons in the jet with an energy distribution as given by Eq. 2.2. Instead, the HE peak is due to the IC scattering of internal (SSC; [4, 5, 6]) or external photons (EIC; [7, 9, 8]). The IC scattering of external photons is considered, since the SEDs of FSRQs are better explained by EIC, as shown by the previous studies (e.g., [91, 92, 93, 94, 67]), and the CD is evident in the SEDs of the considered sources (Figure 2.6). Localization of the emission region in the jet is an open question and along the jet, depending on the distance from the central black hole, different photon fields can be dominant for the IC scattering [32]. Here we assume that the emitting region is outside the broad-line region (BLR) where the dominant photon field is the IR emission from the dusty torus. Sikora et al. [95] showed that in MeV blazar SEDs the shift of the peak of the HE component to lower energies is most likely due to the comptonization of IR photons from the dusty torus. The IR radiation from the dusty torus is assumed to have a blackbody spectrum with a luminosity of $L_{\text{IR}} = 0.6L_{\text{disc}}$ (see Ahnen et al. [91]) where L_{disc} is the accretion disk luminosity, which fills a volume that for simplicity is approximated as a spherical shell with a radius of $R_{\text{IR}} = 2.5 \times 10^{18}(L_{\text{d}}/10^{45})^{1/2}$ cm [35] with the energy density of $u_{\text{IR}} = 0.6L_{\text{d}}/4\pi R_{\text{IR}}^2 \delta^2$ in the co-moving frame of the jet. In Ghisellini et al. [50] and [56], the HE component in the SED of distant blazars was modeled by IC scattering of BLR reflected photons, adopting a smooth broken power-law shape of the emitting electrons. We refer the reader to these papers for details on the modeling when BLR reflected photons are considered.

The broadband SEDs have been modeled using the JetSet version 1.1.2 numerical leptonic code [96, 97, 98]. The free model parameters (those of the emitting electrons, δ , R and B) are constrained by using the Minuit optimizer. The emission directly due to accretion emerges primarily in the UV band, showing a UV excess in the SED, which is modeled by adding a blackbody component [74]. Fitting of this excess allows us to estimate the disc photons temperature and luminosity. When the excess UV component is not distinguished, an upper limit is derived by requiring that the disc emission does not exceed the observed

³ <https://jetset.readthedocs.io/en/latest>





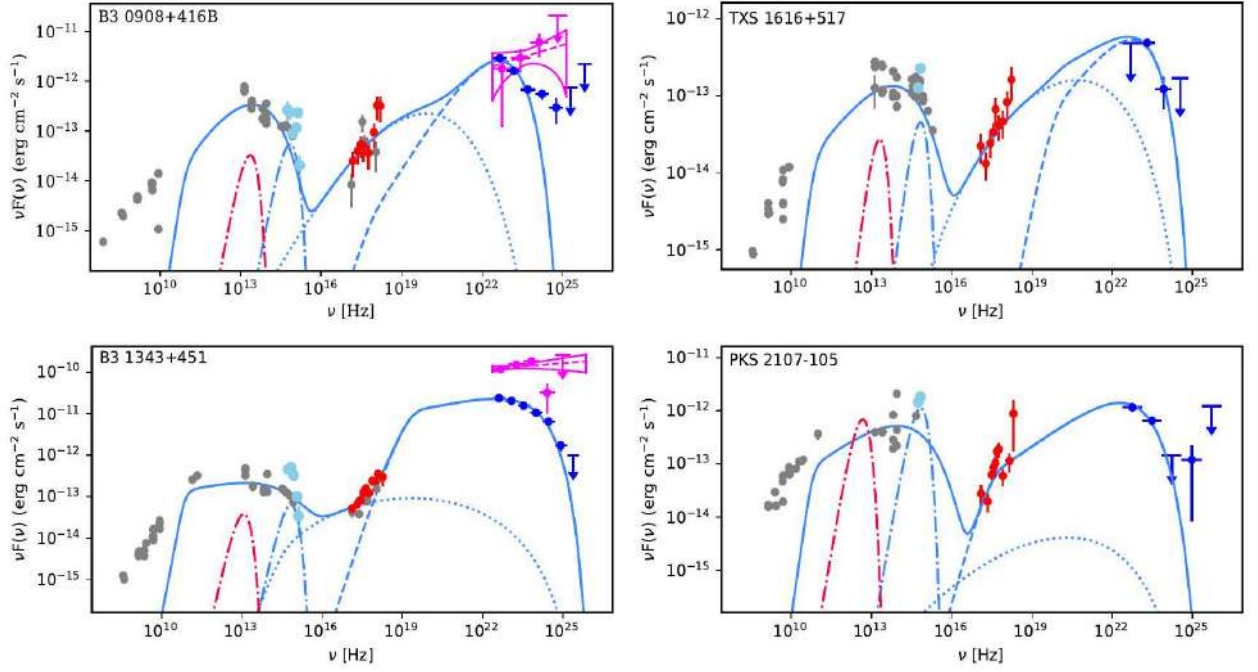


Figure 2.6 Modeling of the broadband SEDs of the considered sources. The Swift UVOT, XRT and Fermi-LAT data obtained here are shown with cyan, red and blue, respectively, while the archival data are in gray.

nonthermal emission from the jet.

SED MODELING RESULTS: The SEDs modeling results are presented in Figure 2.6 and the corresponding parameters in Table 2.5. The archival data from the Space Science Data Center⁴ are in gray, while the optical/UV, X-ray, and γ -ray data, obtained here, are shown in cyan, red, and blue, respectively. The radio data are not included in the SED fits but are considered only as upper limits. The observed radio emission is assumed to originate from a different and extended region. The hard γ -ray emission spectra of TXS 0907+230, PMN J0226+0937, PKS 0451-28, B3 0908+416B, and B3 1343+451 are in magenta, showing that the γ -ray flux increases and their spectra extend to higher energies. As high redshift blazars are considered ($z > 2.5$), their optical/UV flux could be affected by absorption of neutral hydrogen in intervening Lyman- α absorption systems. Following Ghisellini et al. [50] this was corrected using the mean attenuation from Ghisellini et al. [45] which was computed for six wavelengths approximately centered in the UVOT filters.

The SEDs in Figure 2.6 contain enough data from radio to HE γ -ray bands to shape both low and high energy peaks. The applied model reproduces the multiwavelength data relatively

⁴ <https://www.ssdsc.asi.it/>

well for almost all the sources. The γ -ray data of TXS 1448+093 are not well explained by the model because in this case the optical/UV data are clearly constraining the HE tail of the electron distribution and if considering $\alpha > 2.0$ (softer than the estimated spectrum with $\alpha = 1.52 \pm 0.15$), the flux predicted by the model will be lower than the data. Due to the large uncertainties in the S4 2015+65 γ -ray data the modeling is difficult, so the best possible one is shown. The electron power-law index is defined by the X-ray data (through $\alpha = 2\Gamma_X - 1$ relation [99]) and depending on whether the SSC or EIC component is dominating in the X-ray band, different values for α are obtained. When the X-ray spectrum is hard and the SSC component is dominating, the energy distribution of the emitting electrons has a hard spectrum as well. For example, for GB 1508+5714, PKS 0537-286, B2 0743+25, TXS 0222+185 and B3 0908+416B, $\alpha = 1.17 \pm 0.07$, 1.33 ± 0.07 , 1.13 ± 0.19 , 1.62 ± 0.05 and 1.31 ± 0.25 were estimated which shows that the emission is due to newly accelerated electrons. The X-ray emission from S4 1427+543 and TXS 1616+517 is also dominated by the SSC component but because of large uncertainty in the X-ray photon index and flux estimations, correspondingly $\alpha = 2.04 \pm 0.10$ and 2.09 ± 0.09 have been obtained. On the contrary, when the emission in the X-ray and γ -ray bands is only defined by the EIC component then $\alpha > 2.2$; e.g., $\alpha = 2.75 \pm 0.04$ and 2.70 ± 0.06 are correspondingly estimated for TXS 0800+618 and PKS 0834-20. Correspondingly, γ_{\min} and γ_{cut} are in the range of 2.58 – 93.28 and $(1.01 - 15.73) \times 10^3$ (excluding TXS 1448+093). The SSC bump in the X-ray band is sensitive to γ_{\min} values [74, 100, 101] and those estimated here are well within the range usually estimated for the FSRQs (see Fig. 4 in [101]). As expected, [102], lower values of γ_{\min} are estimated when the X-rays are produced only by the EIC component: e.g., $\gamma_{\min} = 2.68 \pm 0.36$ and 2.58 ± 0.15 are correspondingly estimated for PKS 1351-018 and OD 166. The HE tails of both synchrotron and IC components are well defined by the optical/UV and γ -ray data, respectively, allowing precise estimation of $\gamma_{\text{cut}} = (1.01 - 15.73) \times 10^3$. γ_{cut} is in a strong dependence on α , and its highest value, $(15.73 \pm 1.60) \times 10^3$ was estimated when $\alpha = 2.80 \pm 0.04$ (the SED of GB6 J0733+0456 in Figure 2.6). Meanwhile, when $\alpha = 2.2 - 2.5$, the highest γ_{cut} is $(8.67 \pm 0.48) \times 10^3$ for B3 1343+451.

The modeling shows that the magnetic field in the emitting region is within 0.10 – 1.74 G.

The highest values of $1.74 \pm 0.12, 1.68 \pm 0.14, 1.45 \pm 0.09$ and 1.15 ± 0.05 G are estimated for PMN J0226+0937, PMN J1441-1523, MG2 J174803+3403, and OD 166, respectively. The estimated Doppler factor is from $\delta = 10.00$ to $\delta = 27.42$ with a mean of $\delta = 19.09$. Although, these are higher than the average values estimated for FSRQs (e.g., [103, 104]), they are well within the range of physically realistic values (e.g., see [105]). The emitting region size is within $R = (0.70 - 9.48) \times 10^{16}$ cm except for TXS 0800+618 and S4 2015+65 for which $R = 1.55 \times 10^{17}$ cm and 1.35×10^{17} cm, respectively. The values estimated for R are consistent with the γ -ray flux variation in a day or several day scales and suggest that the multiwavelength emission is produced in the sub-parsec scale regions of the jet.

The energetics of the considered sources can be estimated using the modeling results. First, the available data allows a straightforward estimation of the disc luminosity of GB 1508+5714, PKS 1351-108, PKS 0537-286, TXS 0800+618, S4 1427+543, GB6 J0733+0456, B2 0743+25, PKS 0347-211, S41124+57, PKS 043843, S4 2015+65, PKS 0834

Table 2.5: Parameters obtained from the modeling of multiwavelength SEDs. [1]: object name. [2]: Doppler factor. [3]: Slope of electron energy distribution. [4] and [5]: the Lorentz factors corresponding to the minimum and cutoff energy of the electron distribution. [6]: Magnetic field in units of G. [7] Radius of the emitting region in units of 10^{16} cm. [8] and [9]: Electron and magnetic field energy densities. [10]: accretion disk luminosity in units of 10^{46} erg s^{-1} . [11] and [12]: The power of the jet in the form of the relativistic electrons (L_e) and magnetic field (L_B) in units of 10^{45} erg s^{-1} and 10^{43} erg s^{-1} , respectively.

Sources [1]	δ [2]	α [3]	γ_{\min} [4]	γ_{cut} [5]	B [6]	R [7]	U_e [8]	U_B [9]	L_d [10]	L_e [11]	L_B [12]
GB 1508+5714	15.72 ± 1.29	1.17 ± 0.07	26.90 ± 2.88	1.30 ± 0.10	0.19 ± 0.02	2.28	0.50	1.49	3.02	2.43	0.73
PKS 1351-018	20.47 ± 2.49	2.16 ± 0.11	2.68 ± 0.36	4.99 ± 0.71	0.20 ± 0.02	2.29	0.54	1.66	4.04	2.68	0.82
PKS 0537-286	11.50 ± 0.57	1.33 ± 0.07	15.70 ± 1.49	2.45 ± 0.16	0.28 ± 0.02	1.14	5.93	3.21	3.44	7.31	0.40
TXS 0800+618	14.04 ± 0.56	2.75 ± 0.04	13.98 ± 0.86	2.20 ± 0.02	0.26 ± 0.01	15.5	0.06	2.73	1.65	13.49	61.84
S4 1427+543	10.00 ± 0.37	2.04 ± 0.10	29.00 ± 2.55	2.79 ± 0.27	0.53 ± 0.04	1.90	0.63	10.02	1.83	2.14	3.75
GB6 J0733+0456	16.28 ± 1.36	2.80 ± 0.04	47.90 ± 3.42	15.73 ± 1.60	0.16 ± 0.03	2.98	0.12	6.22	3.40	0.98	5.20
PKS 0347-211	26.00 ± 1.02	2.79 ± 0.02	23.09 ± 1.12	2.62 ± 0.16	0.20 ± 0.01	8.15	0.03	1.61	1.99	1.72	10.08
B2 0743+25	10.02 ± 0.45	1.13 ± 0.19	7.66 ± 0.22	2.03 ± 0.08	0.36 ± 0.01	0.70	16.90	0.003	3.58	7.80	0.24
S4 1124+57	22.17 ± 1.37	2.78 ± 0.04	22.92 ± 1.45	1.28 ± 0.10	0.22 ± 0.01	5.15	0.14	1.95	1.69	3.39	4.87
PKS 0438-43	18.17 ± 1.29	2.78 ± 0.04	23.13 ± 1.54	7.19 ± 0.58	0.34 ± 0.02	5.42	0.12	4.52	3.91	3.33	12.52
S4 2015+65	17.85 ± 1.32	2.73 ± 0.05	20.63 ± 1.64	2.75 ± 0.29	0.46 ± 0.03	13.50	0.07	8.41	4.55	1.26	14.44
MG2 J174803+3403	24.50 ± 2.06	2.87 ± 0.06	14.67 ± 1.58	1.40 ± 0.49	1.45 ± 0.09	7.41	0.004	83.98	8.87	0.23	434.69
PKS 0834-20	27.42 ± 0.97	2.70 ± 0.06	20.57 ± 1.51	2.13 ± 0.18	0.37 ± 0.02	6.83	0.02	5.44	5.51	0.70	23.92
TXS 0222+185	10.03 ± 0.28	1.62 ± 0.05	19.56 ± 0.98	2.38 ± 0.10	0.35 ± 0.02	1.07	10.28	5.04	2.71	11.10	0.54
OD 166	19.02 ± 0.84	1.96 ± 0.04	2.58 ± 0.15	1.01 ± 0.03	1.15 ± 0.05	4.32	0.01	0.52	0.53	0.25	92.38
TXS 0907+230	21.66 ± 1.66	2.23 ± 0.11	20.26 ± 1.84	1.44 ± 0.10	0.31 ± 0.02	5.23	0.03	3.72	1.09	0.70	5.96
PMN J1441-1523	17.01 ± 1.50	2.19 ± 0.07	2.86 ± 0.29	3.31 ± 0.46	1.68 ± 0.14	1.47	0.07	112.38	0.17	0.14	22.85
TXS 1448+093	17.90 ± 1.13	1.52 ± 0.15	49.64 ± 5.82	0.84 ± 0.06	0.70 ± 0.05	7.96	0.003	19.44	0.56	0.17	115.93
PMN J0226+0937	25.02 ± 1.98	2.41 ± 0.04	5.37 ± 0.59	8.32 ± 0.62	1.74 ± 0.12	3.09	0.03	119.86	10.94	0.03	107.98
PKS 0451-28	26.14 ± 1.27	2.90 ± 0.28	21.93 ± 1.3	2.19 ± 0.01	0.45 ± 0.03	5.90	0.11	8.01	7.20	3.59	26.32
B3 0908+416B	23.22 ± 1.72	1.31 ± 0.25	6.41 ± 0.72	1.11 ± 0.10	0.39 ± 0.03	1.76	0.09	6.10	0.43	0.26	1.78
TXS 1616+517	10.11 ± 0.31	2.09 ± 0.09	93.28 ± 4.15	4.34 ± 0.36	0.52 ± 0.02	3.59	0.06	10.79	0.35	0.70	13.11
B3 1343+451	26.55 ± 1.04	2.48 ± 0.04	16.49 ± 1.31	8.67 ± 0.48	0.10 ± 0.01	4.16	0.11	0.42	0.48	1.76	0.68
PKS 2107-105	27.32 ± 1.34	2.30 ± 0.06	7.45 ± 0.90	3.63 ± 0.39	0.67 ± 0.05	9.48	0.0006	17.73	8.30	0.05	150.16

-20, TXS 0222+185, TXS 0907+230, PMN J0226+0937, PKS 0451-28 and PKS 2107-105, under the assumption that the disc has a black body spectrum. The estimation shows that $L_d \simeq (1.09 - 10.94) \times 10^{46} \text{ erg s}^{-1}$ with a highest value of $L_d \simeq 1.09 \times 10^{47} \text{ erg s}^{-1}$ estimated for PMN J0226+0937. Such high luminosities are obtained as very powerful blazars are considered here, and they are of the same order as those usually estimated for bright FSRQs [78] and distant blazars [50, 48]. The jet power in the form of the magnetic field (L_B) and relativistic electrons (L_e) is calculated as $L = \pi R^2 c \Gamma^2 U_i$, where U_i is either electron (U_e) or magnetic field (U_B) energy density, using the parameters from Table 2.5. The corresponding values are given in Table 2.5, showing that L_e is in the range of $(0.03 - 13.49) \times 10^{45} \text{ erg s}^{-1}$ while L_B in $(0.24 - 434.69) \times 10^{44} \text{ erg s}^{-1}$. L_B and L_e are of the same order with $L_e/L_B = 2.92$ and 0.61 for PKS 0834-20 and PMN J14411523 respectively, while for MG2 J174803+3403, OD 166, TXS 1448+093, PMN J0226+0937, PKS 2107-105 $L_B/L_e = 3.7 - 36.0$. For the other sources of Table 2.5, L_e exceeds L_B , the largest deviation of $L_e/L_B \geq 1800$ being found for PKS 0537-286, B2 0743+25 and TXS 0222+185, which are the only sources when the hard X-ray emission above the Swift XRT band is modeled with a SSC component and the EIC is dominating at higher energies. However, we note that the luminosities can be higher when the SEDs in the flaring periods are modeled.

2.7 DISCUSSION AND CONCLUSION

Fermi-LAT has detected MeV/GeV emission from ~ 2500 blazars, which are bright emitters across the whole electromagnetic spectrum. Fermi-LAT has sufficient sensitivity to detect blazars farther than $z = 2.0$, which are among the most powerful objects in the Universe. The distant objects ($z > 2.0$) represent a small fraction of the total observed sources (3.75 per cent), but their investigation is crucial for the study of the powerful relativistic outflows and measurement of the EBL photon density. We selected the most distant blazars ($z > 2.5$) from 4FGL and studied their multiwavelength emission properties by analyzing Fermi-LAT, Swift XRT and UVOT data. Also, the origin of their multiwavelength emission is investigated through theoretical modeling of the broadband SEDs.

In the X-ray and γ -ray bands, the spectra of the considered sources have different properties; except for TXS 1448+093, the X-ray spectrum of the other sources is hard with

$\Gamma_X = 1.01 - 1.86$ while in the γ -ray band $\Gamma_\gamma > 2.2$. Thus, the X-ray and γ -ray data are determining that the second peak in the SED is within $10^6 - 10^8$ eV. The γ -ray flux of the considered sources is from 4.84×10^{-10} to 1.50×10^{-7} photon $\text{cm}^{-2}\text{s}^{-1}$, and in the $\Gamma_\gamma - L_\gamma$ plane, they occupy the area more typical for bright blazars, which is natural, since the sources at large distances should be powerful enough to be detected. The two BL Lacs included in the sample, 87GB 214302.1+095227 and MG1 J154930+1708, are relatively faint, $\simeq (0.48 - 1.37) \times 10^{-9}$ photon $\text{cm}^{-2}\text{s}^{-1}$, although it is already unusual to observe BL Lacs at large distances.

In the $F_X - \Gamma_X$ plane the considered sources occupy the region of hard X-ray spectra ($\Gamma_X < 2.0$) and a flux from 7.94×10^{-14} erg $\text{cm}^{-2}\text{s}^{-1}$ to 1.17×10^{-11} erg $\text{cm}^{-2}\text{s}^{-1}$. PKS 0451-28, TXS 0222+185, PKS 0834-20, PKS 0537-286, TXS 0800+618, B2 0743+25 and PKS 0438-43 are separated from the others with a comparably high X-ray flux $F_{X\text{-ray}} \geq 2.13 \times 10^{-12}$ erg $\text{cm}^{-2}\text{s}^{-1}$. In the X-ray band, statistically significant flux variation is found for PKS 0438-43 and B2 0743+25 while there is an indication of variability for TXS 0222+185; during the bright X-ray periods, their flux exceeds 10^{-11} erg $\text{cm}^{-2}\text{s}^{-1}$.

The γ -ray flux variability can be investigated based on the available data. The most distant flaring blazars are MG3 J163554+3629 and PKS 0537-286 at $z = 3.65$ and $z = 3.10$, respectively. Though γ -ray flux amplification is observed in the 30-d bin light curve of MG3 J163554+3629, the γ -ray flares are more drastic and evident for PKS 0537-286. The adaptively binned light curve PKS 0537-286 shows several bright γ -ray flaring periods with a maximum flux of $(1.29 \pm 0.26) \times 10^{-7}$ photon $\text{cm}^{-2}\text{s}^{-1}$ above 100 MeV, observed on MJD 57879.2 in a time bin having a width of ~ 16.0 hours. For the distance of PKS 0537-286, such flux amplification can be useful for investigation of the $\gamma\gamma$ attenuation, but the photon index is $\Gamma_\gamma = 2.64 \pm 0.27$, so the flare is dominated by sub-GeV photons. The γ -ray flux of B3 1343+451 increases in sub-day scales and that of PKS 0347-211 ($z = 2.94$) and PKS 0451-28 ($z = 2.56$) in day scales. B3 1343+451 is among the top 30 bright blazars observed by Fermi-LAT, showing multiple periods of enhanced γ -ray emission when the average luminosity of $(2 - 4) \times 10^{48}$ erg s^{-1} increased up to 1.5×10^{50} erg s^{-1} . The peak γ -ray flux of $(1.82 \pm 0.45) \times 10^{-6}$ photon $\text{cm}^{-2}\text{s}^{-1}$ above 100 MeV was observed on MJD 55891.7 which is ≥ 36.4

times higher than the γ -ray flux in quiescent state. The χ^2 test showed that the γ -ray emission of B3 0908+416B, TXS 0800+618, PKS 0438-43, OD 166 and TXS 0907+230 is variable in week scales while that of MG3 J163554+3629, GB6 J0733+0456, B2 0743+25, PMN J1441-1523 and TXS 1616+517 in month scales.

The γ -ray photon index of B3 1343+451, PKS 0451-28, B3 0908+416B and TXS 0907+230 varies in time, and their γ -ray emission sometimes appears with a hard γ -ray spectrum. The averaged γ -ray photon index of these sources determines that the peak of the HE component to be below 10^8 eV whereas the hard γ -ray spectrum indicates that the peak is shifted to higher energies. During the flares, different processes can cause the shift of the low-energy or HE peaks. For example, both components will be shifted to HEs when the particles are effectively re-accelerated, resulting in higher electron cutoff energy (γ_{cut}). It is expected that only the HE component will increase when due to the changes in the location of the emitting region the external photon fields are starting to dominate [85]. In order to understand the origin of the change in the emission components, extensive multiwavelength observations are required which is not the case for the sources considered here. We note that such changes have already been observed in the previous studies of blazars (e.g., [106, 91, 92, 64]).

The main parameters characterizing the jets of the considered sources are derived by modeling the multiwavelength SEDs. The CD observed in the spectrum of almost all the considered sources implies that the electrons are losing energy mainly by interacting with the external photons. In the framework of the single-zone scenario, the observed X-ray and γ -ray data are satisfactorily explained taking into account IC scattering of synchrotron and IR photons which in its turn allows to constrain the parameters of the emitting electrons. The power-law index of the electrons is from ~ 1.13 to 2.90, which is within the range expected from the standard particle acceleration theories. For example, in the diffuse shock particle acceleration, the formed particle spectra can be from very hard (-1) to very steep, depending on the shock speed, nature of particle scattering, magnitude of turbulence, shock field obliquity, and other parameters [107]. On the other hand, the optical/UV and γ -ray data strongly constrain the cut-off energy of electrons; the particles are effectively accelerated up

to $\sim 10^{12}$ eV. The cooling of emitting particles defines the cut-off energy formed when the acceleration and cooling time scales are equal. Considering the electrons are mostly cooling by interacting with IR photons, and equating the radiative cooling time $t_{\text{cool}} \sim \frac{3m_e c}{4\sigma'_T u'_{\text{IR}} \gamma'_e}$ with the electron acceleration time $t_{\text{acc}} \simeq \eta_0 \frac{m_e c \gamma'_e}{eB}$ [108] one gets that for 10^{12} eV electrons these timescales are equal when $\eta^{-1} = 5 \times 10^{-4}$. In other words, the maximum electron energy, if limited solely by the radiative energy losses, might be expected to be much higher than that observed, since often $\eta^{-1} \geq 10^{-2}$ is expected (e.g., [27]). Therefore, the cutoff is most likely limited by the physical size of the emitting zone. For a given set of parameters, $R, B,$ and $\delta, \gamma_{\text{min}}$ is < 93 and lower values of γ_{min} are estimated when the X-rays are produced only by EIC. This shows that the process responsible for the particle acceleration picks up almost all electrons.

The total jet luminosity (defined as $L = L_e + L_B$) is $\leq 1.41 \times 10^{46}$ erg s^{-1} . which is of the same order as that usually calculated for blazars [109]. Thus, the jet power of distant and nearby blazars do not differ substantially. The estimated disc luminosity is within $L_d \simeq (1.09 - 10.94) \times 10^{46}$ erg s^{-1} , more typical for powerful blazars. The disc and jet luminosities are of the same order for TXS 0800+618 and TXS 0222+185 ($L_{\text{disc}}/L_{\text{jet}} = 1.17 - 2.44$) while for the others L_{disc} is higher than L_{jet} . However, we note that the protons with unknown content in jet are not included in the computation of L_{jet} , so in principle higher L_{jet} are expected which could be of the same order as L_{disc} [110]. Yet, when the accretion disc luminosity and temperature are well measured, an approximate value of the black hole mass can be derived following Ghisellini et al. [111, 112]. In general, the black hole mass can be well estimated from the optical spectroscopy [113] or from fitting the blue bump at the optical/UV band [114, 103]. The maximum temperature (and hence the νF_ν peak of the disc luminosity) of the standard multi-colour accretion disc temperature profile occurs at $5R_S$ where R_S is Schwarzschild radius. Taking into account that the peak temperature scales as $T_{\text{disc}} \sim (L_{\text{disc}}/R_S)^{1/4}$ [111], R_S can be estimated from which the black hole mass can be derived. The black hole mass estimated for the sources with a clear blue-bump in their SED is in the narrow range of $(1.69 - 5.35) \times 10^9 M_\odot$ where the highest black hole mass of $5.35 \times 10^9 M_\odot$ is estimated for PMN J0226+0937 which has also the highest disc luminosity. The virial black

hole mass of GB 1508+5714, PKS 1351-018, S4 1427+543 and B2 0743+25 is also estimated in the quasar catalog of Shen et al. [115] and is $(3.23 \pm 0.40) \times 10^8 M_{\odot}$, $(8.91 \pm 0.64) \times 10^8 M_{\odot}$, $(1.80 \pm 0.17) \times 10^8 M_{\odot}$ and $(3.89 \pm 0.26) \times 10^9 M_{\odot}$, respectively. In the case of B2 0743+25, both methods produce similar results, $3.06 \times 10^9 M_{\odot}$ and $(3.89 - 0.26) \times 10^9 M_{\odot}$, while for the other sources the masses obtained using optical spectroscopy are slightly lower. Such differences are expected, since both methods rely on a fitting or approximations. For the considered sources, the Eddington luminosity is within $(2.12 - 5.87) \times 10^{48} \text{ erg s}^{-1}$ and the ratio $L_{\text{disc}}/L_{\text{Edd}}$ ranges from 0.05 to 0.16 (e.g., see [109]).

2.8 SUMMARY

The origin of the multiwavelength emission from distant blazars ($z > 2.5$) has been investigated using the Fermi-LAT data accumulated in 2008-2018 and Swift XRT/UVOT data observed in the last fifteen years. The main results are summarized as follows:

i) Twenty-six out of the thirty-three considered sources are FSRQs, five BCUs, and only two are BL Lacs. The two BL Lacs are also the faintest objects in the sample with a flux of $(0.48 - 1.66) \times 10^{-9} \text{ photon cm}^{-2} \text{ s}^{-1}$ while the others have a flux from $2.73 \times 10^{-9} \text{ photon cm}^{-2} \text{ s}^{-1}$ to $\sim 1.50 \times 10^{-7} \text{ photon cm}^{-2} \text{ s}^{-1}$.

ii) Except for the two BL Lacs, the photon index of all the considered sources ranges from 2.18 to 3.05. Only, the γ -ray indexes of B3 1343+451, PKS 0451-28, B3 0908+416B and TXS 0907+230 are found to vary in time. The hardest γ -ray spectra of B3 1343+451, B3 0908+416B and TXS 0907+230 are with indexes of 1.73 ± 0.24 , 1.84 ± 0.25 , and 1.72 ± 0.15 , respectively, while that of PKS 0451-28, with 2.06 ± 0.07 .

iii) The Swift XRT observations show a significant X-ray emission only from the FSRQs considered here. Only a few counts have been detected from the other sources, even if some of them have been observed by Swift several times. The X-ray photon index of distant FSRQs is $\Gamma_X = 1.1 - 1.8$ and the flux is spanning from $\sim 5 \times 10^{-14} \text{ erg cm}^{-2} \text{ s}^{-1}$ to $10^{-11} \text{ erg cm}^{-2} \text{ s}^{-1}$.

iv) The brightest X-ray source in the sample is TXS 0222+185 ($z = 2.69$) with a flux of $(1.19 \pm 0.04) \times 10^{-11} \text{ erg cm}^{-2} \text{ s}^{-1}$. The X-ray emission from only PKS 0438-43, B2 0743+25 and TXS 0222+185 showed a substantial flux increase in some observations, whereas the X-ray emission from other sources is relatively constant in different years.

v) The γ -ray variability of the considered sources has been investigated using the data accumulated for ten years. Fourteen sources from the sample show a variable γ -ray emission on short and long timescales. The γ -ray flux of B3 1343+451 ($z = 2.53$) and PKS 0537-286 ($z = 3.10$) increases in sub-day scales, that of PKS 0347-211 ($z = 2.94$) and PKS 0451-28 ($z = 2.56$) in day scales. The γ -ray emission of B3 0908+416B, TXS 0800+618, PKS 0438-43, OD 166 and TXS 0907+230 is variable in a week scale while that of MG3 J163554+3629, GB6 J0733+0456, B2 0743+25, PMN J1441-1523 and TXS 1616+517 in a month scale. The most distant γ -ray blazar flaring on short time scales is PKS 0537-286 ($z = 3.10$) when its flux increased up to $(1.29 \pm 0.26) \times 10^{-6}$ photon $\text{cm}^{-2} \text{s}^{-1}$ above 100 MeV within a time bin having a width of ~ 16.0 hours. The γ -ray flux of B3 1343+45 increased significantly from its average level in multiple periods with a maximum flux of $(1.82 \pm 0.45) \times 10^{-6}$ photon $\text{cm}^{-2} \text{s}^{-1}$ above 100 MeV, accompanied by moderate hardening of the spectra.

vi) In the $\Gamma_\gamma - L_\gamma$ plane, the majority of the considered sources occupy the narrow range of $\Gamma_\gamma = 2.2 - 3.1$ and $L_\gamma = (0.10 - 5.54) \times 10^{48}$ erg s^{-1} which is more typical for the brightest blazars. However, during γ -ray flares, the luminosity of variable sources is significantly beyond this boundary, changing within $(10^{49} - 10^{50})$ erg s^{-1} . For example, the luminosity of B3 1343+451 increases ~ 36.4 times and corresponds to $L_\gamma = 1.5 \times 10^{50}$ erg s^{-1} , being among the highest values so far observed in the γ -ray band.

vii) The SEDs were modeled within a one-zone leptonic scenario, considering the IC scattering of both synchrotron and IR photons from the dusty torus. The X-ray and γ -ray data allowed to constrain the peak of the HE component (within $10^6 - 10^8$ eV) as well as the power-law index and cut-off energy of the radiating electrons; the index and the cutoff energy are within the range of $1.13 - 2.90$ and $(1.01 - 15.73) \times 10^3$, respectively. The radius of the emitting region is estimated to be ≤ 0.05 pc while the magnetic field and the Doppler factor are correspondingly within $0.10 - 1.74$ G and $10.00 - 27.42$.

viii) The jet luminosity is estimated to be $\leq 1.41 \times 10^{46}$ erg s^{-1} , which is of the order of the values usually obtained for blazars. For all the sources, except for TXS 0800+618 and TXS 0222+185 for which $L_{\text{disc}}/L_{\text{jet}} = 1.17 - 2.44$, the jet luminosity is lower than that of the disc $L_d \simeq (1.09 - 10.94) \times 10^{46}$ erg s^{-1} which is estimated by fitting the UV excess. The black hole

masses are estimated to be within $(1.69 - 5.35) \times 10^9 M_{\odot}$ so the disc luminosity is 5 – 16 per cent of the Eddington luminosity.

3 ORIGIN OF MULTIWAVELENGTH EMISSION FROM FLARING HIGH REDSHIFT BLAZAR PKS 0537-286

3.1 INTRODUCTION

The new possibility of extensive multiwavelength observations coupled with multi-messenger observations have the potential to widen our understanding of blazars. Being powerful emitters, blazars are frequently monitored in all the accessible wavelengths which resulted in accumulation of a substantial amount of data.

Due to the extreme luminosities of blazars, even very high redshift ones can be observed (e.g., see [54]). The observation of distant blazars is of particular interest as they allow i) to study the relativistic jets as well as their connection with accretion disk/black hole in the early epochs of the Universe, ii) to measure the suppression of the γ -ray flux which can be used to estimate or constraint the density of the extragalactic background light (EBL) [116, 117, 118] and understand its cosmological evolution, iii) to investigate, in general, the properties of γ -ray emitting active galactic nuclei (AGN), which is important for the understanding of the cosmological evolution of the γ -ray background [119].

Due to their faintness, high redshift blazars are rather difficult to observe and identify, limiting the number of already associated high redshift blazars. For example, in the fourth catalog of AGNs detected by Fermi-LAT (data release 3 (DR3) [120]) only 110 blazars are observed beyond $z = 2.0$ and only 10 beyond $z = 3.0$. The most distant blazar observed in the γ -ray band is GB1 508+5714 at $z = 4.31$. The physical properties of these high redshift blazars have been frequently investigated using multifrequency data (e.g. [111, 50, 49, 48, 56, 54, 51, 57]). For example, in Paliya et al. [121] by studying nine γ -ray emitting blazars and 133 candidate blazars with soft X-ray spectra it is shown that these high redshift blazars host massive black holes ($M_{\text{BH}} > 10^9 M_{\odot}$) and have an accretion disk luminosity of $> 10^{46} \text{ erg s}^{-1}$. Or, in Sahakyan et al. [122], by studying the spectral and temporal properties of thirty-three distant blazars ($z > 2.5$) and modeling their SEDs, it is found that the emission region size is $\leq 0.05 \text{ pc}$, while the magnetic field and the Doppler factor are correspondingly within $0.10 - 1.74 \text{ G}$ and $10.0 - 27.4$.

Although the number of observed high redshift blazars is not high enough to perform statistically sound population studies, the investigation of the properties of individual objects provides interesting pieces to understand the general physics of high redshift blazars. The multiwavelength monitoring of several high redshift blazars opens wide opportunities for investigation of their multiwavelength spectral and temporal properties as well as for performing detailed theoretical modeling and interpretation of the results. For example, the continuous monitoring of these sources in the HE γ -ray band by Fermi-LAT [123] allows to select various emission states, or their observations in the X-ray band with Neil Gehrels Swift Observatory ([47], hereafter Swift), and Nuclear Spectroscopic Telescope Array (NuSTAR; [124]) combined with the γ -ray data allows a precise estimation of the second emission component peak, or the data in the optical/UV bands can be used to constrain the HE tail of the synchrotron component and/or the direct thermal emission from the accretion disk [50]. Therefore, the data available in different bands can be used to put tighter constraints on the physics of individual high redshift blazars.

Here, we present a broad-band study of PKS 0537-286; at $z = 3.10$ [125] it is one of the brightest high redshift blazars. It was observed in the X-ray band with various instruments (e.g., Einstein observatory [126], ASCA [127, 128], ROSAT [129], etc.) showing a particularly hard X-ray spectrum (~ 1.2). In the γ -ray band, with an energy flux of $(1.44 \pm 0.006) \times 10^{-11} \text{ erg cm}^{-2}\text{s}^{-1}$ in the fourth catalog of Fermi-LAT AGNs [[120], DR3;], it is the brightest blazar beyond $z = 3.0$. Moreover, in several occasions γ -ray flares were observed when the daily flux was above $10^{-6} \text{ photon cm}^{-2}\text{s}^{-1}$ [75, 130, 131] which makes PKS 0537-286 the most distant γ -ray flaring blazar [51, 132]. The broadband emission from PKS 0537-286 was successfully modeled within a one-zone synchrotron and external IC scenario where the excess in optical/UV band was interpreted as emission from bright thermal accretion disk [133].

In general, the peak of the second component in the SED of high redshift blazars is at MeV energies, which implies their HE γ -ray spectrum is soft, so they are not ideal sources for γ -ray observations. Therefore, the observation of the γ -ray flaring activity of distant blazars, which is crucial for testing different emission scenarios of relativistic jets, is even more

interesting as compared with that of the nearby sources. Motivated (i) by the availability of multiwavelength data from PKS 0537-286 observations since 2008 in the HE γ -ray band by Fermi-LAT, multiple observations of PKS 0537-286 by Swift X-Ray Telescope (XRT) and Ultra-violet Optical Telescope (UVOT) instruments and two observations of PKS 0537-286 with NuSTAR, and (ii) by the observed multiple flaring activities of PKS 0537-286, we decided to investigate the spectral and temporal properties of PKS 0537-286 by analyzing the data accumulated in the optical/UV, X-ray and γ -ray bands and put, through theoretical modeling, a constraint on the physical processes responsible for the PKS 0537-286 emission in the quiescent and flaring states.

3.2 FERMI-LAT OBSERVATIONS AND DATA ANALYSES

Fermi-LAT is by default in the all sky scanning mode which allows to study the HE properties of various sources, including blazars. For more details on the LAT see Atwood et al. [123].

We have analyzed the γ -ray data collected between 2008 August 4 and 2022 September 9 (MET=239557417–686130659). The data was reduced and analyzed following the standard procedures described in the Fermi-LAT documentation with FERMITOOLS version 2.0.8 using P8R3_SOURCE_V3 instrument response functions. The events in the energy range from 100 MeV to 300 GeV are selected from a circular region of interest (ROI) of 12° radius centered at the γ -ray location of PKS 0537-286 (RA = 89.99, Dec = -28.65), retrieving only events classified as *'evclass=128'* and *'evtype=3'*. A zenith angle cut less than 90° was introduced to remove the secondary γ -rays from the earth limb. The model file that includes point-like sources and background models was created based on the Fermi-LAT fourth source catalog (4FGL) incremental version (DR3; [120]), which is based on 12 years of initial Fermi-LAT operation and includes best-fit spectral parameters of all known 4FGL γ -ray sources in the ROI. The sources which are within 17° from the PKS 0537-286 location were included in the model file; the spectral parameters of the sources within $12^\circ - 17^\circ$ are fixed to their values reported in 4FGL while they are left free for the sources falling within $< 12^\circ$ radius. The galactic background and isotropic galactic emissions were modeled with the latest version available files, *gll_iem_v07* and *iso_P8R3_SOURCE_V3_v1*, respectively.

The γ -ray analysis is performed with *gtlike* tool, following the binned likelihood method. Initially, the spectrum of PKS 0537-286 was modeled with a log-parabolic model as in 4FGL. However, the fit was also performed when assuming a power-law model for PKS 0537-286 γ -ray emission and the resulting model file was used in the light-curve calculations, because for shorter periods a power-law can be a good approximation of the spectrum. The significance of the source emission is estimated using test statistic (TS), which is defined by $TS = 2(\ln L_1 - \ln L_0)$ where L_1 and L_0 are maximum likelihoods with and without the source, respectively [61].

In order to investigate the variability pattern of the source, the light curves were generated by two different methods. Initially, the whole-time interval was divided into 5-d intervals and the photon index and flux of PKS 0537-286 were estimated by the unbinned analysis method from *gtlike* tool. Next, in order to obtain a deeper insight into the γ -ray flux evolution in time, the adaptively binned light curve was computed [62]. In this method, the bin widths above the optimal energy (E_{opt}) are adjusted to have fixed uncertainty, so in the case of flux increase shorter intervals are estimated, whereas in the quiescent/normal states time bins are wider. This method has been proven to be a powerful tool in finding flaring periods in blazars [e.g., see [63, 134, 64, 69, 66, 67, 65, 135, 136, 137].

The adaptively binned light curve ($> E_{opt} = 168.19$ MeV) is shown in Figure 3.1 upper panel. Up to MJD 57740 the γ -ray flux was in its average level of $(1 - 3) \times 10^{-8}$ photon $\text{cm}^{-2}\text{s}^{-1}$ with no significant changes, while then, in several occasions, the γ -ray flux increased substantially. The light curve with 5-d (> 100 MeV) and adaptive bins ($> E_{opt} = 168.19$ MeV) for the period when the source was active in the γ -ray band are shown correspondingly in Figure 3.1 panels (a) and (b). The first flaring period was between MJD 57876-57883 when the flux increased with a maximum of $(5.26 \pm 1.13) \times 10^{-7}$ photon $\text{cm}^{-2}\text{s}^{-1}$. Starting from MJD 59170, the source entered an active emission state with several bright flaring periods between MJD 59204-59233, MJD 59301-59411 and MJD 59721-59738. The maximum γ -ray flux of the source, $(6.32 \pm 1.11) \times 10^{-7}$ photon $\text{cm}^{-2}\text{s}^{-1}$ was also observed in these γ -ray flaring periods.

Figure 3.1 panel (c) shows the γ -ray photon index estimated for the adaptively binned

periods; it varies in time as well. In the non-flaring periods, the γ -ray spectrum is characterized by a soft spectrum with a mean of $\Gamma \simeq 2.83$ but the photon index hardens during the bright periods as can be seen from Figure 3.1 panel c. For example, during the first flare between MJD 57876-57883 the hardest index of 2.49 ± 0.23 was observed on MJD 57879.9 or during the second flare between MJD 59204-59233 the hardest index was 2.25 ± 0.21 when the source was in an active state with a flux of $(6.12 \pm 1.22) \times 10^{-7}$ photon $\text{cm}^{-2}\text{s}^{-1}$. During the hardest γ -ray emission period, 2.23 ± 0.18 was detected on MJD 59322 which is unusual for this source.

3.3 NUSTAR DATA ANALYSIS

NuSTAR is a hard X-ray telescope sensitive in the 3-79 keV energy range [124]. NuSTAR with two focal plane modules (FPMs), FPMA and FPMB, observed PKS 0537-286 on 28 December 2020 (MJD 59211.99) and on 24 October 2020 (MJD 59146.17) for 97.1 ks and 24.3 ks, respectively. It should be noted that around these observations PKS 0537-286 was also monitored with Swift (see dashed blue lines in Figure 3.1 panel (d)), so the X-ray spectrum of the source can be obtained in a large range of 0.3-79 keV.

The NuSTAR data was analyzed applying the standard procedure and using NuSTAR_Spectra tool developed in Middei et al. [138]. NuSTAR_Spectra script downloads calibrated and filtered event files from the SSDC repository, uses XIMAGE package to precisely locate the source's coordinate then extracts high-level scientific products for the detected sources using NUPRODUCTS routine. The script automatically sets the source extraction region radius depending on the source counts (usually in the range of 30-70 arcsec). The background is computed in an annulus centered on the source with a minimum separation of 50 arcsec between the inner and outer radii. Then, a spectral analysis is performed using the XSPEC package [139] adopting Cash statistics [71]. More details on NuSTAR_Spectra are available in Middei et al. [138].

The analysis shows that the X-ray photon index of PKS 0537-286 is the same in both observations – 1.26 ± 0.06 and 1.26 ± 0.02 on MJD 59146.17 and MJD 59211.99, respectively. The X-ray flux between 3 and 10 keV measured on MJD 59146.17 is $F_{3-10 \text{ keV}} = (2.72 \pm 0.06) \times 10^{-12}$ erg $\text{cm}^{-2}\text{s}^{-1}$ and on MJD 59211.99, it increased by about a factor of two,

$F_{3-10 \text{ keV}} = (5.10 \pm 0.04) \times 10^{-12} \text{ erg cm}^{-2}\text{s}^{-1}$. Similarly, the flux between 10-30 keV also increased in these two observations, being correspondingly $F_{10-30 \text{ keV}} = (5.79 \pm 0.20) \times 10^{-12} \text{ erg cm}^{-2}\text{s}^{-1}$ and $F_{10-30 \text{ keV}} = (1.08 \pm 0.01) \times 10^{-11} \text{ erg cm}^{-2}\text{s}^{-1}$. This shows that the source in the 3.0-30 keV range was in an enhanced state on 2020 December 28.

3.4 SWIFT DATA ANALYSIS

Swift is a space-based observatory with three main instruments onboard, namely burst alert telescope (BAT) sensitive in the energy range of 3.0-150.0 keV, XRT sensitive in the energy range of 0.3-10.0 keV, and UVOT sensitive in the optical/UV band 170 - 650 nm [47]. Swift performed 29 observations of PKS 0537-286 among which nine observations were performed before the launch of Fermi-LAT. However, in order to investigate the flux changes in different years, we have analyzed all the data from Swift observations of PKS 0537-286.

SWIFT XRT: All the XRT observations were processed with Swift_xrtproc tool applying standard analysis procedure [140]. Swift_xrtproc downloads the raw data for each snapshot and for the whole observation, generates exposure maps and calibrated data product using the XRTPIPELINE task adopting standard parameters and filtering criteria. The source region counts are estimated from a circle of a radius of 20 pixels while the background counts from an annular region centered around the source with a radius sufficiently large to avoid contamination from source photons. The resultant ungrouped data is loaded in XSPEC [139] for spectral fitting using Cash statistics [71], modeling the source spectrum as power-law and log-parabola. As a result, the X-ray photon index in the energy range 0.3-10 keV and the flux in various bands are estimated.

The 2-10 keV X-ray flux variation is shown in Figure 3.1 panel (d). Although in the X-ray band there is a limited number of observations, the flux variation is evident. The X-ray emission of the source in the 2.0-10 keV band was at the level of $\sim 3.0 \times 10^{-12} \text{ erg cm}^{-2}\text{s}^{-1}$ but during the bright periods it is $\geq 5.0 \times 10^{-12} \text{ erg cm}^{-2}\text{s}^{-1}$. The highest X-ray flux of $(8.34 \pm 3.59) \times 10^{-12} \text{ erg cm}^{-2}\text{s}^{-1}$ was observed on MJD 59213.18. The X-ray spectrum of the source is hard (Figure 3.1 panel e) and during all the observations $\Gamma_{\text{X-ray}} \leq 1.38$. Therefore, as it is typical for FSRQs, the X-ray band defines the rising part of the second component in the SED.

SWIFT UVOT: In the same periods, UVOT observed PKS 0537-286 in V (500-600 nm), B (380- 500 nm), U (300- 400 nm), W1 (220-400 nm), M2 (200-280 nm) and W2 (180-260 nm) filters. All the available 28 observations were downloaded and reduced using HEASoft version 6.29 with the latest release of HEASARC CALDB. Photometry was computed using a five-arcsecond source region centered on the sky position of PKS 0537-286 and the background counts are estimated from a twenty-arcsecond region away from the source. The magnitudes were derived using `uvotsource` tool, then the fluxes were obtained using the conversion factors provided by Poole et al. [70] which were corrected for extinction using the reddening coefficient $E(B - V)$ from the Infrared Science Archive⁵.

Figure 3.1 panel (f) shows the light curve of PKS 0537-286 in optical/UV bands. The source is relatively faint in all the filters with the flux around $\approx 10^{-13}$ erg cm⁻²s⁻¹. In some cases, coinciding with the flares in the γ -ray band, the flux increased several times. The highest flux of the source was observed in V-band; on MJD 59213.18 and MJD 59732.67 it was $(1.08 \pm 0.37) \times 10^{-12}$ erg cm⁻²s⁻¹ and $(1.38 \pm 0.26) \times 10^{-12}$ erg cm⁻²s⁻¹, respectively. In addition, VOU-Blazar tool, which allows to search and collect all spectral information accessible through virtual observatory services and build the multiwavelength SEDs of blazars was used to investigate the source emission properties in the infrared band [141]. In particular, data extracted from the Wide-field Infrared Survey Explorer (WISE) and NEOWISE surveys [142] show that the source emission at 3.4 and 4.6 μ m wavelengths (infrared) was at the level of several times 10^{-13} erg cm⁻²s⁻¹.

3.1 MULTIWAVELENGTH SEDS

The data analyzed in this study allows to build the SEDs of PKS 0537-286 in different periods. The single snapshot SED provides substantial information on the source emission properties whereas the variation of these SEDs in time is crucial for understanding the dynamical changes in the emission components. For this purpose, we generated SED/Light curve animation of PKS 0537-286 by showing the γ -ray spectra with all available data sets. For each adaptively binned interval we performed γ -ray spectral analysis using the unbinned likelihood method implemented in *gtlike* tool. Then, for each γ -ray period, together with the

⁵ <http://irsa.ipac.caltech.edu/applications/DUST/>

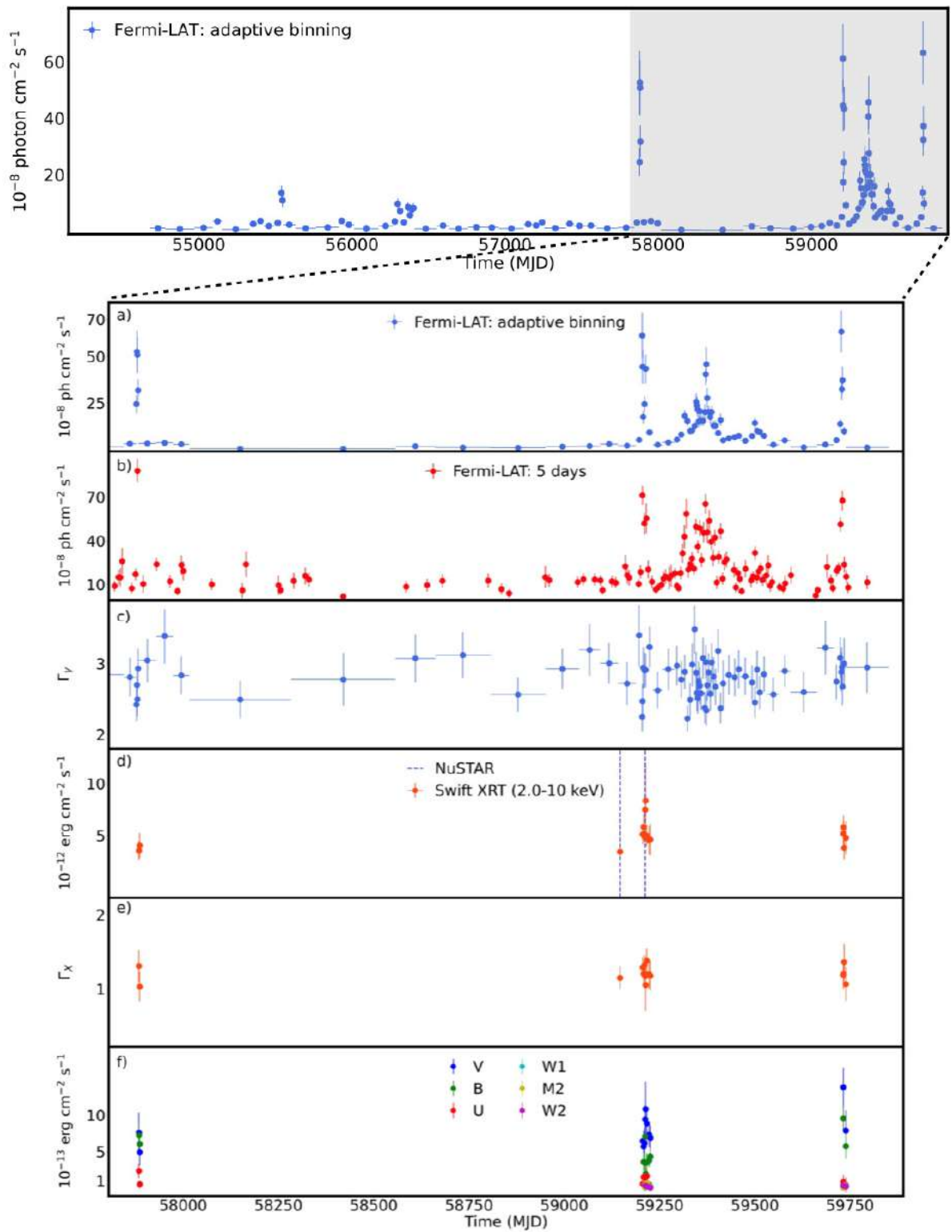


Figure 3.1 Multiwavelength light curve of PKS 0537-286. Top panel shows the long-term adaptively binned γ -ray light curve above 168.19 MeV. The other panels show the light curves after MJD 57800 (16 February 2017) when the source was active in the γ -ray band. (a) adaptively binned γ -ray light curve, (b) 5-day binned γ -ray light curve (> 100 MeV), (c) γ -ray photon index measured for the adaptive time bins, (d) and (e) X-ray flux (2-10 keV) and photon index in different Swift observations. The dashed blue lines show the NuSTAR observation times. (f) Swift UVOT fluxes in V, B, U, W1, M2, and W2 bands.

γ -ray data we plotted the Swift XRT, NuSTAR and Swift UVOT data as well as archival data extracted with VOU-blazar tool. By going from one to another γ -ray period we can investigate the changes in the multiwavelength SED of PKS 0537-286.

The SED/light curve animation is available here <https://youtu.be/4UPqf-C7EWc>. As the blazar is at $z = 3.10$ the UVOT flux could be affected by absorption of neutral hydrogen in intervening Lyman- α absorption systems (e.g, [50]) which was corrected using the attenuation calculated in [45] for the UVOT filters. The SED/light curve animation shows the high amplitude changes observed in the γ -ray band; the gray background data points show the γ -ray flux estimated in different periods. Also, the spectral hardening in several bright γ -ray periods can be seen.

3.2 ORIGIN OF BROADBAND EMISSION

In the previous section, the generated multiwavelength SEDs show the features of PKS 0537-286 emission in different periods. It is especially important to investigate the processes taking place in the jet of high redshift blazars as they could provide information on the jet plasma state in the early Universe. For this reason, the following periods were considered for modeling:

(i) The SED between MJD 55150-55330 when the source was in the quiescent state, i.e., the γ -ray flux above 100 MeV was $(2.77 \pm 0.84) \times 10^{-8}$ photon $\text{cm}^{-2}\text{s}^{-1}$ and the 2-10 keV X-ray flux was $(3.29 \pm 1.11) \times 10^{-12}$ erg $\text{cm}^{-2}\text{s}^{-1}$. (ii) The SED between MJD 59208-59212 when the source was bright in the γ -ray and X-ray (2-10 keV) bands with corresponding fluxes of $(5.46 \pm 0.83) \times 10^{-8}$ photon $\text{cm}^{-2}\text{s}^{-1}$ and $(7.47 \pm 1.18) \times 10^{-12}$ erg $\text{cm}^{-2}\text{s}^{-1}$. This

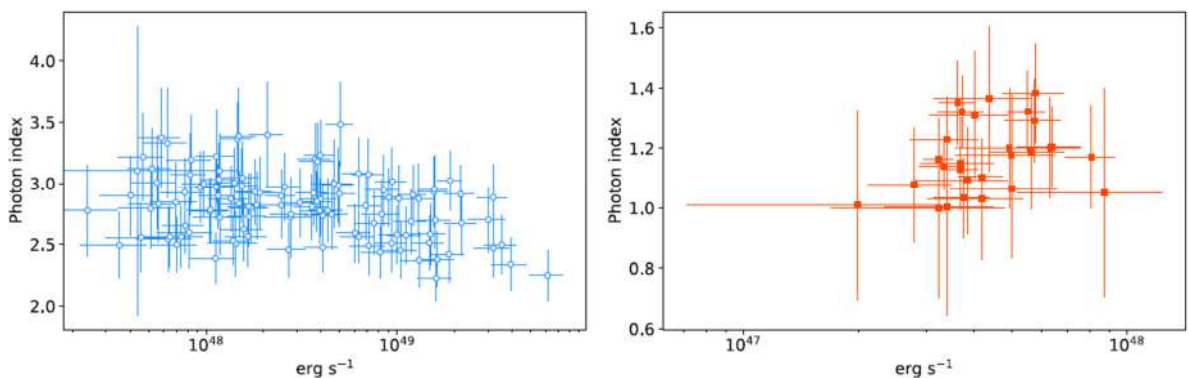


Figure 3.2. The luminosity versus the spectral index in the γ -ray (left-hand panel) and X-ray bands (right-hand panel).

period coincides with the NuSTAR observation on MJD 59211.99 which showed that the source was in an elevated X-ray emission state also in the 3-30 keV range.

The broadband SEDs were modeled using a one-zone leptonic scenario. In this model, it is assumed that the emission originates from a spherical blob of radius R moving with a bulk Lorentz factor of Γ at a small inclination angle of θ with respect to the observer. Due to the relativistic motion and small θ the radiation will be Doppler amplified by a factor of $\delta \simeq \Gamma$. The emission region magnetized with a field strength of B is filled with relativistic electrons whose energy distribution is given by,

$$N_e = N_0 \gamma^{-p} \exp\left(-\frac{\gamma}{\gamma_{cut}}\right) \quad \gamma > \gamma_{min} \quad (3.1)$$

where $\gamma = E_e/m_e c^2$ is the electron Lorentz factor, p is the power-law index, γ_{min} and γ_{cut} are the minimum and cut-off energy, respectively. The parameter N_0 defines the electron energy density through $U_e = m_e c^2 \int \gamma N_e(\gamma) d\gamma$.

The electrons with energy distribution given by Eq. 3.1 undergo synchrotron losses under the magnetic field, producing the data observed between radio to X-ray bands. Instead, the second component in the SED, from X-rays to γ -rays, is from the IC scattering of internal and external photons on the same population of the electrons. When the electrons upscatter the synchrotron photons, the second component is explained by the SSC component [4, 6, 5]. Alternatively, if the emission region is within the BLR, the second component can be due to external Compton scattering of direct disk radiation (EIC-disk; [143, 144]) and/or due to external Compton scattering of photon reflected from BLR clouds (EIC-BLR; [9]). Instead, if the jet energy dissipation occurs at larger distances it can be due to external Compton scattering of dusty torus photons (EIC-torus; [7]).

Here, for a general view we consider three different scenarios: i) the broadband emission from PKS 0537-286 is entirely due to synchrotron/SSC radiation, ii) the jet dissipation region is close to the central black hole, and SSC, EIC-disk and EIC-BLR are contributing to the HE component and iii) the emission region is beyond the BLR and the HE component is due to EIC-torus. It is assumed that BLR is a spherical shell (e.g., [145]) with lower and upper boundaries of $0.9 \times R_{BLR}$ and $1.2 \times R_{BLR}$, respectively. R_{BLR} is assumed to scale as $R_{BLR} = 10^{17} L_{disc,45}^{0.5} \text{ cm}$ where $L_{disc,45} = L_{disc}/10^{45} \text{ erg s}^{-1}$ is the accretion disk luminosity [103].

Similarly, we assume that the distance of dusty torus is $2 \times 10^{18} L_{\text{disc},45}^{0.5}$ [103] which emits $\eta = 0.5$ fraction of disk luminosity in the IR range for which we adopted $T_{\text{torus}} = 10^3$ K effective temperature. The disk luminosity and effective temperature are correspondingly $8.7 \times 10^{46} \text{ erg s}^{-1}$ and $T_{\text{disk}} = 1.9 \times 10^4$ K estimated by fitting the thermal blue-bump component in the SED with a black-body component.

The remaining free model parameters are p , γ_{min} , γ_{cut} , U_e , B and R which should be constrained during the fitting. The SED fitting is performed using publicly available code JetSet which is a numerical code allowing to fit the radiative models to data and obtain the parameters statistically better explaining them [146, 97, 96, 147]. These parameters are initially constrained by using the Minuit optimizer and then improved by Markov Chain Monte Carlo (MCMC) sampling of their distributions. We applied the EBL model from Franceschini et al. [118] to correct the attenuation in the HE γ -ray band, but as the γ -ray data extends to several tens of GeV it affects only the model extrapolation to higher energies.

3.3 RESULTS AND DISCUSSIONS

At $z = 3.10$, PKS 0537-286 is one of the most powerful FSRQs in the extragalactic γ -ray sky; the time-averaged γ -ray luminosity of the source is $1.90 \times 10^{48} \text{ erg s}^{-1}$ (assuming a distance of 27.08 Gpc). However, in several occasions, the source shows bright γ -ray flares when the flux substantially increases and the spectrum hardens. Figure 3.2 left panel shows the γ -ray luminosity of PKS 0537-286 versus the photon index. During the bright periods, the luminosity increases, being above $10^{49} \text{ erg s}^{-1}$; the maximum γ -ray luminosity corresponds to $6.14 \times 10^{49} \text{ erg s}^{-1}$. It should be noted that among 113 adaptively binned intervals, the source luminosity was above $10^{49} \text{ erg s}^{-1}$ in 25 intervals amounting 61.8 days when extreme γ -ray luminosity was observed. Photon index hardening with increasing luminosity/flux can be noticed in Figure 3.2 left panel. In order to test possible correlation/anti-correlation between the luminosity and photon index, a Pearson correlation test was applied which yielded -0.39 with a probability of $P = 1.2 \times 10^{-5}$. This indicates moderate anti-correlation between the luminosity and photon index, that is when the source emission becomes brighter the photon index hardens (harder-when-brighter trend). It should be noted that for blazars such trend is frequently observed in different bands (e.g. [76, 148,

66, 67, 149, 137, 135]) which can be interpreted as interplay between acceleration and cooling of the electrons [86].

PKS 0537-286 shows also interesting features in the X-ray band. The X-ray photon index versus the 0.3–10 keV X-ray luminosity is shown in Figure 3.2 right panel. The X-ray emission is characterized by a hard spectrum ($\Gamma_{\text{X-ray}} < 1.38$) with a high luminosity ($> 10^{47}$ erg s $^{-1}$). It should be noted that XMM-Newton observations of PKS 0537-286 also showed a high luminosity of 2×10^{47} erg s $^{-1}$. with a spectral index of 1.27 ± 0.02 [150]. There is no evidence of softening or hardening when the source gets brighter in the X-ray band; the highest luminosity in the X-ray luminosity was 1.40×10^{48} erg s $^{-1}$ on MJD 59211.99 and 7.47×10^{47} erg s $^{-1}$. on MJD 59146.17.

The SED of PKS 0537-286 was assembled in the flaring and quiescent periods (see Figure 3.3). Comparing and contrasting the jet parameters obtained through modeling of the SED in different periods is crucial, allowing to understand the processes at work in the jet of PKS 0537-286.

SYNCHROTRON/SSC EMISSION FROM THE JET: Figure 3.3 panels (a) and (b) show the results of the modeling when the entire emission is due to synchrotron/SSC emission from a compact region of the jet when the source is in a quiescent and flaring state, respectively. The corresponding model parameters are given in Table 3.1. In the quiescent state, the SED modeling shows that the spectral slope of the emitting particle distribution is 1.8 ± 0.1 and their distribution extends up to $(1.2 \pm 0.1) \times 10^4$. The strength of the magnetic field is found to be $(9.3 \pm 0.8) \times 10^{-3}$ G. The emission region size is $(2.0 \pm 0.1) \times 10^{17}$ cm, which is consistent with the flux variability of $t_{\text{var}} = (1 + z) \times R/c \delta \approx 18.7$ days. The Doppler boosting factor is 16.8 ± 1.2 which is not different from the values usually estimated for FSRQs (e.g., see [103]). In this case, the synchrotron component decreases at $< 10^{14}$ Hz and it does not take into account the observed optical/UV data which are interpreted as thermal emission from the accretion disk (see the next subsection).

In the flaring period (Figure 3.3 panel b), the SED modeling shows that the emitting electrons have a harder spectrum with $p = 1.6 \pm 0.03$ as compared with that in the quiescent state. The electrons are accelerated up to $\gamma_{\text{cut}} = (1.1 \pm 0.1) \times 10^4$ which is not significantly

different from that in the quiescent state. In the flaring state, the magnetic field also increased, $B = (1.7 \pm 0.1) \times 10^{-2}$ G, which is caused by the increase of the synchrotron flux. Also, the Doppler boosting factor increased from 16.8 ± 1.2 to 24.9 ± 1.1 in order to explain the slight shift of the HE peak towards higher energies; above 100 MeV the γ -ray spectrum in the flaring period has a photon index of $\Gamma_\gamma = 2.73 \pm 0.17$ as compared with that of $\Gamma_\gamma = 2.91 \pm 0.16$ in the quiescent state. The modeling shows that during the flare, the emission is produced from a smaller region with a radius of $(1.6 \pm 0.1) \times 10^{17}$ cm corresponding to $t_{\text{var}} \simeq 10.0$ days, which indicates that the flaring emission is from a compact and faster moving region.

EMITTING REGION WITHIN THE BLR: Figure 3.3 panels (c) and (d) show the SED modeling assuming the jet dissipation occurred close to the central source. In this case, the density of disk-emitted and BLR-reflected photons in the jet frame (taking into account Doppler amplification) is comparable with or larger than that of synchrotron photons so their IC scattering has a non-negligible contribution. The thermal emission from the accretion disk, modeled as a black body, is shown with a pink dashed line. In the quiescent state (Figure 3.3 panel c), the low-energy component of the spectrum (up to 10^{16} Hz) can be reasonably well explained by combined synchrotron and black body components. The data in the X-ray band is mostly dominated by the EIC-disk component (blue dashed line in Figure 3.3) with SSC contributing in the soft X-ray band, whereas the emission in the γ -ray band is due to EIC-disk and EIC- BLR components (blue dashed and purple dot-dot-dashed lines in Figure 3.3, respectively). As compared with the synchrotron/SSC model, the distribution of the electrons is narrower with $p = 2.3 \pm 0.2$ and $\gamma_{\text{cut}} = (0.3 \pm 0.1) \times 10^3$, because the average energy of the external photons is larger than that of the synchrotron one. The Doppler boosting factor is $\delta = 13.4 \pm 1.3$ but the magnetic field is significantly larger, $B = 3.5 \pm 0.4$ G. Since the flux in the HE band depends on the photon and particle density and the content of external photons is higher (inferred from the observed high Compton dominance, i.e., the ratio between the peak flux of IC and synchrotron components), the number of emitting electrons is reduced; to produce the synchrotron emission at the same level higher magnetic field is required. The emission is produced in a more compact region with a radius of (0.2 ± 0.02)

$\times 10^{17}$ cm, smaller than $R_{\text{BLR}} = 9.3 \times 10^{17}$ cm.

During the flaring period, in the optical/UV band, the synchrotron emission from the jet dominates over the thermal emission from the accretion disk (Figure 3.3 panel d). As the synchrotron emission extends to higher frequencies, the SSC component makes a non-negligible contribution in the X-ray band (orange dot-dashed line in Figure 3.3 panel d). The

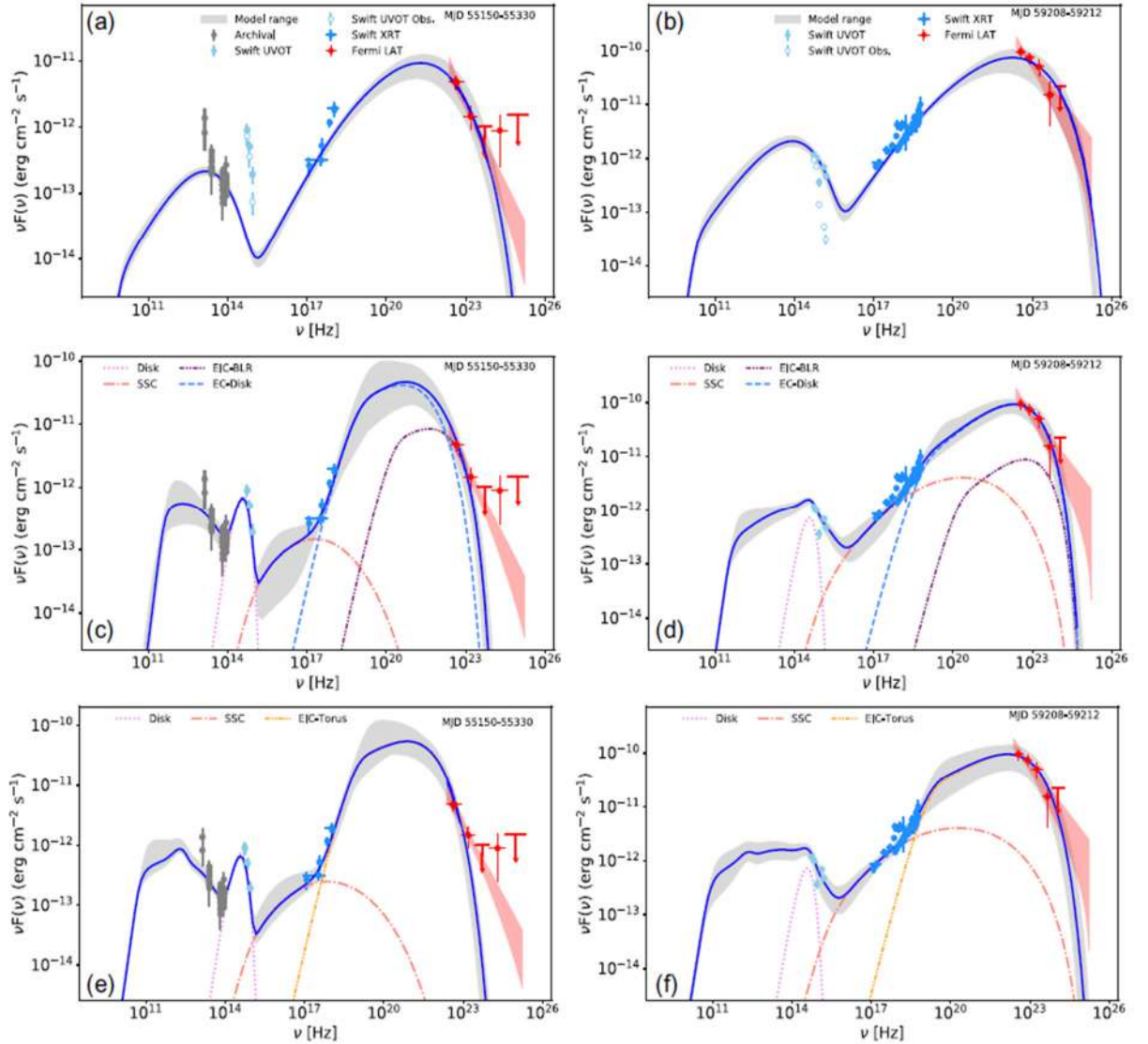


Figure 3.3 The broad-band SEDs of PKS 0537 –286 in the quiescent (left-hand panels) and flaring (right-hand panels) states. Panels (a) and (b) correspond to SED modeling when the emission is entirely due to synchrotron/SSC radiation. The SED modeling when the emission region is within the BLR is shown in panels (c) and (d), while in panels (e) and (f), it is outside the BLR. The blue solid curve shows the sum of all components and the grey shaded area is the uncertainty region from MCMC sampling of the parameters. The color code of the other components is given in the legends. In panels (a) and (b), the observed and absorption-corrected Swift UVOT fluxes are shown with empty and filled light blue circles, respectively.

γ -ray emission is mostly due to the EIC-disk component (blue dashed line in Figure 3.3 panel d) and EIC-BLR contributes at higher γ -ray energies (purple dot-dot-dashed line in Figure 3.3 panel d). In this case, the electron distribution is nearly flat with $p = 2.2 \pm 0.1$ and extends up to $(2.5 \pm 0.2) \times 10^3$. The increase of the energy up to which the electrons are effectively accelerated (γ_{cut}) resulted in the shift of the synchrotron component to higher frequencies and domination over the disk thermal emission. The Doppler boosting is $\delta = 11.4 \pm 0.7$, the magnetic field is $B = 3.0 \pm 0.2$ G and the emission region radius is $(0.1 \pm 0.01) \times 10^{17}$ cm. This is smaller than that estimated in the quiescent state and corresponds to 1.5 days variability.

EMITTING REGION OUTSIDE BLR: Figure 3.3 panels (e) and (f) show PKS 0537-286 SED modeling assuming the emission region is beyond the BLR. In the quiescent state, the HE component is entirely dominated by EIC-torus (yellow dot-dot-dashed line in Figure 3.3 panel e) and SSC contributing in the soft X-ray band (orange dot-dashed line in Figure 3.3 panel e). In the flaring state, the peak of the SSC component is around $\sim 10^{22}$ Hz (orange dot-dashed line in Figure 3.3 panel f) making a non-negligible contribution to the X-ray band, but again, the HE γ -ray data is solely explained by the EIC-torus component (yellow dot-dot-dashed line in Figure 3.3 panel f). The model parameters given in Table 3.1 show that in the quiescent and flaring states the electron distribution has a similar power-law index $p \simeq 2.4$, but in the flaring state the cut-off energy is larger, $\gamma_{\text{cut}} = (6.7 \pm 0.7) \times 10^3$ as compared to $\gamma_{\text{cut}} = (1.3 \pm 0.1) \times 10^3$. This is because (i) the synchrotron component should extend beyond the optical/UV band and (ii) during the flare the γ -ray spectrum is harder, shifting this component towards higher frequencies. Also, the modeling shows that the Doppler

Table 3.1: Parameters best describing the PKS 0537-286 multiwavelength emission in the scenarios shown in Figure 3.3.

	SSC		EIC-BLR		EIC Torus	
	quiescent	flare	quiescent	flare	quiescent	flare
p	1.8 ± 0.1	1.6 ± 0.03	2.3 ± 0.2	2.2 ± 0.1	2.4 ± 0.1	2.4 ± 0.1
$\gamma_{\text{cut}}/10^3$	11.8 ± 0.8	11.5 ± 0.6	0.3 ± 0.1	2.5 ± 0.2	1.3 ± 0.1	6.7 ± 0.7
γ_{min}	9.5 ± 1.0	1.3 ± 0.1	26.1 ± 3.8	30.1 ± 2.5	65.7 ± 3.4	103.9 ± 9.0
δ	16.8 ± 1.2	24.9 ± 1.1	13.4 ± 1.3	11.4 ± 0.7	15.3 ± 0.7	14.2 ± 1.0
$B[\text{G}]$	$(9.3 \pm 0.8) \times 10^{-3}$	$(1.7 \pm 0.1) \times 10^{-2}$	3.5 ± 0.4	3.0 ± 0.2	0.2 ± 0.01	0.2 ± 0.02
$R[\text{cm}]/10^{17}$	2.0 ± 0.1	1.6 ± 0.1	0.2 ± 0.02	0.1 ± 0.01	2.0 ± 0.1	1.4 ± 0.1
$L_e[\text{erg s}^{-1}]$	1.2×10^{47}	1.2×10^{47}	1.3×10^{45}	2.0×10^{45}	1.1×10^{46}	1.3×10^{46}
$L_B[\text{erg s}^{-1}]$	3.5×10^{42}	1.8×10^{43}	2.2×10^{45}	5.3×10^{44}	1.3×10^{45}	7.9×10^{44}

boosting and magnetic field do not substantially change, correspondingly being $\delta = 15.3 \pm 0.7$ and $B = 0.2 \pm 0.01$ G and $\delta = 14.2 \pm 1.0$ and $B = 0.2 \pm 0.02$ G for the flaring and quiescent states. However, again in the flaring state, the emission region has a slightly smaller radius $(1.4 \pm 0.1) \times 10^{17}$ cm as compared with $(2.0 \pm 0.1) \times 10^{17}$ cm.

JET LUMINOSITY: The parameters estimated during the modeling are used to compute the jet luminosity. The jet power carried by the electrons, calculated as $L_e = \pi c R_b^2 \Gamma^2 U_e$, and by magnetic field, calculated as $L_B = \pi c R_b^2 \Gamma^2 U_B$ are given in Table 3.1. In the case of synchrotron/SSC scenario (Figure 3.3 panels a and b), the jet should be strongly particle dominated with a luminosity of the order of $\approx 10^{47}$ erg s⁻¹ where the magnetic luminosity has a marginal contribution ($L_e/L_B \approx 3 \times 10^4$). This is natural, given the SED of PKS 0537-286 in both quiescent and flaring periods shows strong Compton dominance. Relatively high luminosity is also estimated in the modeling when the emitting region is outside the BLR; $L_e + L_B = 1.2 \times 10^{46}$ erg s⁻¹ with $L_e/L_B = 8.1$ and $L_e + L_B = 1.4 \times 10^{46}$ erg s⁻¹ with $L_e/L_B \approx 17$ for the quiescent and flaring states, respectively. When the emitting region is within the BLR, a lower jet luminosity is required, $L_e + L_B = 6.3 \times 10^{45}$ erg s⁻¹ and $L_e + L_B = 2.5 \times 10^{45}$ erg s⁻¹ for the quiescent and flaring states, respectively, and the system is close to equipartition with $L_e/L_B = 0.5$ and $L_e/L_B = 3.7$ for the quiescent and flaring states, respectively.

Also, the total kinetic energy of the jet, defined as $L_{\text{kin}} = L_e + L_B + L_{p,\text{cold}}$, can be evaluated. Assuming a proton-to-electron comoving number density ratio of $N_p/N_e \approx 0.1$, in the most energy demanding model (synchrotron/SSC) $L_{\text{kin}} = 3.2 \times 10^{47}$ erg s⁻¹ and $L_{\text{kin}} = 4.4 \times 10^{47}$ erg s⁻¹ are estimated for the quiescent and flaring states, respectively. In the most optimistic scenario (EIC-BLR), $L_{\text{kin}} = 1.1 \times 10^{46}$ erg s⁻¹ and $L_{\text{kin}} = 6.0 \times 10^{45}$ erg s⁻¹ for the quiescent and flaring states, respectively. In this case, even if assuming $N_p/N_e \approx 1$, one would obtain $L_{\text{kin}} = 4.8 \times 10^{46}$ erg s⁻¹ and $L_{\text{kin}} = 3.8 \times 10^{46}$ erg s⁻¹ for the quiescent and flaring states, respectively. It is interesting that this luminosity is still lower than the disk luminosity estimated from the optical/UV data fitting. However, considering that the presence of the pairs can reduce the jet power (e.g., [151]), the estimated jet luminosity will be by several factors lower than the accretion disk luminosity.

In Bottacini et al. [133], the broadband SED of PKS 0537-286 was modeled assuming the particles are injected into the emitting region, which is inside the BLR, and interact with the internal and external photon fields. The disk luminosity was estimated to be $1.7 \times 10^{47} \text{ erg s}^{-1}$ and $8.4 \times 10^{46} \text{ erg s}^{-1}$ by fitting the data observed in 2008 and 2006, respectively; the latter value is similar to the disk luminosity estimated in the current study. Their modeling showed that L_e is in the range of $(2.5 - 4.0) \times 10^{46} \text{ erg s}^{-1}$ and L_B in $(1.0 - 2.0) \times 10^{45} \text{ erg s}^{-1}$. L_e is slightly larger than that estimated in the current study (see Table 3.1) which is related with different assumptions made in the modeling (e.g., emitting region radius, Doppler boosting factor, etc.).

3.4 SUMMARY

In this work, we have performed a broadband study of the high redshift blazar PKS 0537-286. The main findings are summarized as follows:

(i) PKS 0537-286 is among the highest redshift blazars detected by Fermi-LAT. Its γ -ray emission, monitored since 2008, appeared relatively constant until 2017, then multiple powerful γ -ray flares were observed. Starting from MJD 59170, the source was in an enhanced γ -ray emission state when the γ -ray luminosity reached $6.14 \times 10^{49} \text{ erg s}^{-1}$. During the considered fourteen years, the γ -ray luminosity of the source exceeded $10^{49} \text{ erg s}^{-1}$ for 61.8 days in total.

(ii) The γ -ray photon index of the source varies as well. The mean of the γ -ray photon index during non-flaring periods is $\simeq 2.83$ which substantially hardens during the flares: the hardest index of 2.23 ± 0.18 was observed on MJD 59322. There is a moderate anti-correlation between the γ -ray photon index and luminosity.

(iii) The source is very luminous in the X-ray band with a 0.3 – 10 keV luminosity between $10^{47} - 10^{48} \text{ erg s}^{-1}$ and with a hard spectrum ($\Gamma_{X\text{-ray}} < 1.38$). The available NuSTAR observations show that the hard X-ray spectrum extends up to 30 keV with $\Gamma_{X\text{-ray}} = 1.26$ with a luminosity between $(0.75 - 1.40) \times 10^{48} \text{ erg s}^{-1}$.

(iv) In order to understand the underlying physical processes at work in the jet of PKS 0537-286, the SEDs during the quiescent and flaring states were reproduced using a simple one-zone leptonic emission model considering different locations of the emission region. In

the quiescent state, the combined synchrotron and thermal accretion disk components can explain the IR-optical-UV data, whereas X-ray to HE γ -ray data are due to IC scattering of the disk and BLR-reflected photons. Instead, in the flaring state, the jet synchrotron emission dominates in the optical/UV band and the X-ray to HE γ -ray emission is due to combination of SSC, EIC-disk and EIC-BLR components. The modeling in the quiescent to flaring states showed that the flare was caused by the electron distribution changes, i.e., the electron power-law index hardened to $p = 2.2 \pm 0.1$ and the cut-off energy was $\gamma_{\text{cut}} = (2.5 \pm 0.2) \times 10^3$.

(v) From the required jet energy point of view, the model with the emission region within the BLR is preferred. During the flaring event, the emitting region is nearly in equipartition with $L_e/L_B = 3.7$ and the jet total luminosity is $L_{\text{tot}} = 3.8 \times 10^{46} \text{ erg s}^{-1}$ when assuming a proton-to-electron comoving number density ratio of $N_p/N_e \simeq 1$. This luminosity is slightly lower than the accretion disk luminosity of $L_{\text{disc}} = 8.7 \times 10^{46} \text{ erg s}^{-1}$ estimated through fitting of UV/optical data.

Among the high red-shift blazars, PKS 0537-286 is exceptional, having a reach multiwavelength data set (especially in the X-ray and γ -ray bands) which allows to investigate the processes taking place in the jet. Further multiwavelength monitoring of such distant and powerful sources will improve our understanding of the radiative processes at work in the relativistic jets in the early Universe.

4 EXPLORING THE ORIGIN OF MULTIWAVELENGTH EMISSION FROM HIGH REDSHIFT BLAZAR B3 1343 + 451

4.1 INTRODUCTION

Blazars are a class of active galactic nuclei (AGN) that emit intense radiation across the entire electromagnetic spectrum. They are characterized by strong and variable emission from a relativistic jet that is oriented towards the Earth. One of the most distinct characteristics of blazar emission is rapid and high amplitude variability across the whole electromagnetic spectrum. The most dramatic and short time scale changes have been observed in the γ -ray band. For example, Brown [152] showed that during the γ -ray flares of PKS 1510-089 the flux doubling timescale was as short as 1.3 ± 0.12 hr or Ackermann et al. [2] showed that the flux doubling times of 3C 279 2015 June flare was less than 5 minutes. Interestingly, in the γ -ray band, the emission from NGC 1275 radio galaxy is also variable in short time scales, 1.21 ± 0.22 hr, which had never been previously observed for any radio galaxy [66, 65]. Considering simple light travel considerations, this strongly constrains the emitting region size, suggesting the radiation comes from the sub-parsec scale regions of the jet. Therefore, the observations of blazars contain valuable information on the initial sub-parsec-scale region of their jets.

The distant blazar B3 1343+451 is among the FSRQs detected by Fermi-LAT. During the recent years, it was reported [153, 154] that several times this source was in the high emission/bright flaring state in the γ -ray band which is interesting considering the distance of B3 1343+451 ($z = 2.534$). Also, the source was monitored by the Neil Gehrels Swift observatory (Swift) several times in various years, providing the data in optical/UV and X-ray bands. Combining this with a large amount of data available in the γ -ray band (more than ten years) will allow a detailed investigation of the origin of multiwavelength emission from B3 1343 + 451. Moreover, for some periods the source was in a flaring state which allows to constrain the emitting region size and location, magnetic field, electron energy distribution, and so on which makes B3 1343+451 an ideal object for exploring the physics of the jets of distant FSRQs.

4.2 DATA ANALYSIS

The data accumulated in the HE γ -ray band by Fermi-LAT is crucial for understanding the nature of variable emission from the blazars. The γ -ray data, being continuously accumulated since 2008, allows to identify different emission states of the sources, compare them with the observations in the other bands and build contemporaneous SEDs necessary for the theoretical modeling. In order to investigate the origin of the emission from B3 1343 + 451, initially the available γ -ray data have been analyzed.

FERMI-LAT DATA EXTRACTION AND ANALYSES: Fermi-LAT on board the Fermi satellite is a pair-conversion telescope, operating since August 4, 2008, and is designed to detect HE γ -rays in the energy range from 20 MeV to 300 GeV [123]. In this study, the data set collected during the first ten years of Fermi-LAT operation, from August 4, 2008, to August 4, 2018 (MET 239557417- 555033605) was used. The data were analyzed with the standard Fermi Science Tools 1.2.1 software package using the most recent reprocessed PASS eight events and spacecraft data in the energy range from 100 MeV to 500 GeV and using P8R3_SOURCE_V2 instrument response function. The entire data set is filtered with *gtselect* and *gtmktime* tools and only the events with a high probability of being photons ‘*evclass=128*’, ‘*evtype=3*’ have been considered. The zenith angle cutoff 90° is made to exclude atmospheric γ -rays from the Earth limb that can be a significant source of background.

The photons from a circular region with a radius of 12° around the γ -ray position of B3 1343+451 (RA, Dec) = (206.394, 44.884) have been extracted. These photons are then binned with the *gtbin* tool with a stereographic projection into pixels of $0.1^\circ \times 0.1^\circ$ and into 37 equal logarithmically-spaced energy bins. The model for which the likelihood is calculated is a combination of point-like sources within a $16.5^\circ \times 16.5^\circ$ square region of interest (ROI) and diffuse Galactic and extragalactic models which were modeled using the standard *gll_iem_v06* and *iso_P8R2_SOURCE_V6_v06* models. The model file describing ROI was created using the Fermi-LAT fourth source catalog (4FGL; [36]) which contains sources within ROI $+5^\circ$ from B3 1343 + 451. The normalization of background models, as well as fluxes and spectral indexes of the sources within the ROI, are considered as free parameters during the analysis, while for the sources outside the ROI the spectral slopes and normalizations were

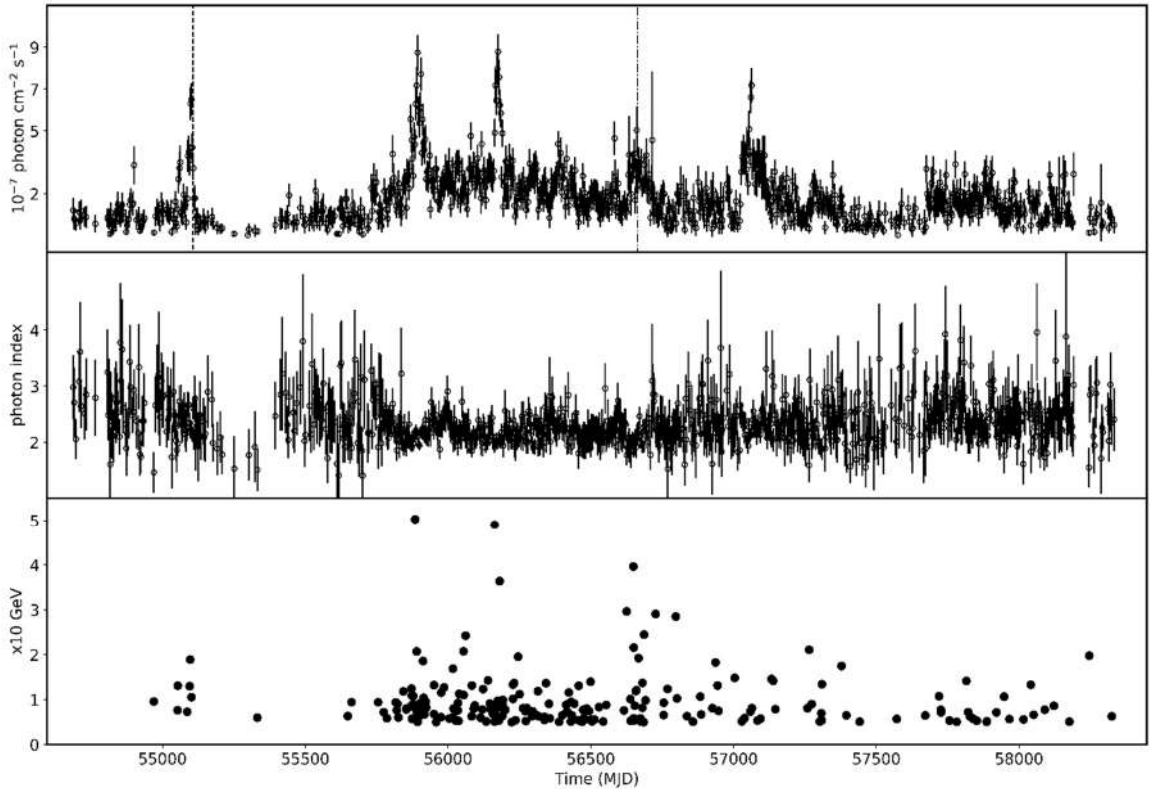


Figure 4.1 The evolution of γ -ray flux and spectral index of B3 1343+451 in time computed using 3-day bins. The lower panel shows the arrival time of HE photons (with energy > 5 GeV).

fixed to the values given in the 4FGL catalog. Initially, for the whole time period, the binned likelihood analysis is performed by *gtlike* tool modeling the γ -ray spectrum of B3 1343+451 using a log-parabola [155] as in 4FGL.

After constraining the parameters of all sources included in the model, the analysis is repeated assuming a power-law shape for the γ -ray spectrum of B3 1343 + 451. The output model is used in the light-curve calculations, as for the short periods the power-law model better represents the spectrum. The γ -ray light curves were calculated by repeating the same analysis for shorter time periods applying an unbinned maximum likelihood analysis method considering photons from 0.1 to 300 GeV energy range. In the model file obtained from the whole-time analysis, the photon indexes of all background sources are fixed to the best guess values in order to reduce the uncertainties in the flux estimations, but the normalization of sources within the ROI are free to vary. Since no variability is expected for the underlying background diffuse emission, we fixed their parameters to the average values obtained in the ten-year analysis.

The γ -ray light curve of B3 1343+451 computed for three-day bins above 100 MeV is

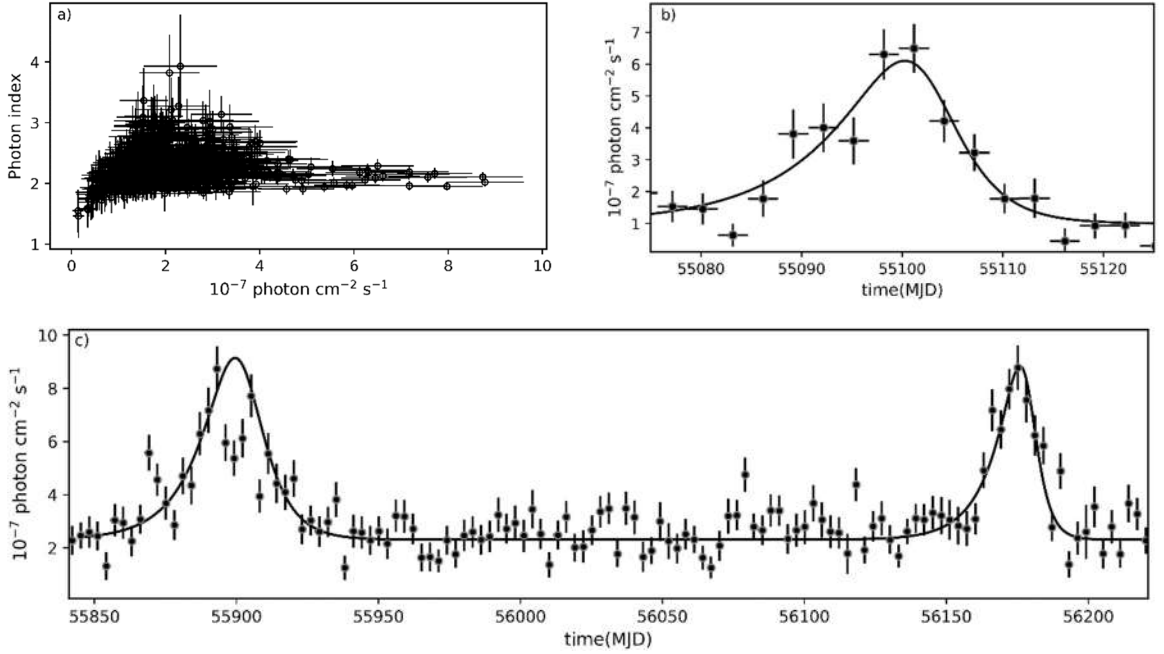


Figure 4.2 Upper left: B3 1343+451 γ -ray photon index vs. flux in three-day bins. Upper right and lower panels: the flare time profile analyses.

shown in Figure 4.1. Several bright γ -ray emission states of the source can be identified, namely from MJD 55083 to 55116, from 55839 to 55965, from 56160 to 56235 and from 57021 to 57126. Interestingly, during the prolonged γ -ray active period from MJD 55720 to 57230, not only two major flares from the source were observed but also the flux increased from its average level and remained so for nearly 500 days. The peak flux of $(8.78 \pm 0.83) \times 10^{-7}$ photon $\text{cm}^{-2}\text{s}^{-1}$ with a photon index of $\Gamma = 2.02 \pm 0.07$ was observed on MJD 56175 within three days with a detection significance of 25.1σ . Another substantial increase of the γ -ray flux has been observed on MJD 55893 when the flux was $(8.73 \pm 0.85) \times 10^{-7}$ photon $\text{cm}^{-2}\text{s}^{-1}$ with $\Gamma = 2.10 \pm 0.08$ photon index and with 24.0σ detection significance. The γ -ray photon index variation in time computed for three-day bins is shown in the middle panel of Figure 4.1. Most of the time, the photon index varies around its averaged value reported in 4FGL (2.14 from the log-parabolic fit), but in some periods hardening and softening are evident. The hardest photon index of $\Gamma = 1.73 \pm 0.24$ has been observed on MJD 58089 with 6.2σ while the softest one 3.13 ± 0.31 was observed on MJD 57675. Unfortunately, in some periods the uncertainties in the photon index estimation are relatively large, which does not allow to make a definite conclusion on the variability of the spectral index.

The evolution of the γ -ray photon index was further investigated by plotting it versus flux

Table 4.1: Parameter values best explaining the flares.

t_m (MJD)	$t_r \pm \text{err}$ (days)	$t_d \pm \text{err}$ (days)	F_c $\times 10^{-7}$ photon cm^{-2} s^{-1}	F_0 $\times 10^{-7}$ photon cm^{-2} s^{-1}
55102.3 ± 1.59	7.91 ± 1.84	3.38 ± 0.84	0.99 ± 0.18	9.42 ± 1.21
55901.3 ± 3.97	11.34 ± 2.85	7.66 ± 2.19	2.31 ± 0.08	13.41 ± 2.67
56178.3 ± 2.32	9.21 ± 2.43	3.64 ± 1.24	2.31 ± 0.08	11.85 ± 2.00

(Figure 4.2 a) considering only the time bins when the detection significance was above 4.0σ . From the plot, the averaged photon index and flux are $\sim 2 \times 10^{-7}$ photon $\text{cm}^{-2}\text{s}^{-1}$ and ~ 2.1 , respectively. There is a hint of spectral hardening as the source gets brighter, i.e., during the bright periods the photon index of the source is relatively harder. In the γ -ray band such behavior has already been observed from several blazars (e.g., [156, 148, 67]) and radio galaxies (e.g., NGC 1275 [66]). Such evolution of the spectral index and flux is expected when accelerated HE electrons are cooled down (e.g., [157]). However, the linear-Pearson correlation test yields to $r_p = 0.05$ with p-value being 0.19. This implies there is a marginal linear correlation between the flux and photon index but it is not statistically significant.

During the three outbursts in the γ -ray band (the first three peaks in Figure 4.1 upper panel) the rising and decaying shapes of the flares can be well constrained by the data. The temporal evolution of each flare has been studied separately. For this purpose, we performed a time profile fitting of these flares by a sum of exponentials which gives the rise and decay times of each peak [158],

$$F(t) = F_c + F_0 \left(\exp\left(\frac{t_0 - t}{t_r}\right) + \exp\left(\frac{t - t_0}{t_d}\right) \right)^{-1} \quad (4.1)$$

where F_0 is the flux at t_0 representing the approximate flare amplitude, F_c is the quiescent flux, t_r and t_d are the rise and decay times of the flare, respectively. The light curve was fitted with the nonlinear optimization python package lmfit⁶.

The fitting parameters are summarized in Table 4.1 and the corresponding fit is shown in Figure 4.2 b) and c). The time profiles show asymmetric structures in all flares, showing a slow rise and a fast decay trend. The rise time of the first flare is 7.91 ± 1.84 days dropping within 3.38 ± 0.84 days. The time peak of the first flare, $t_p = t_0 + t_r t_d (t_r + t_d) \ln(t_d / t_r)$ is at

⁶ <https://lmfit.github.io/lmfit-py/>

Table 4.2: Fermi-LAT spectral analyses results.

Period	Flux ^a	Γ_γ	σ
low	0.44 ± 0.03	2.46 ± 0.05	25.0
F1	6.39 ± 0.57	2.22 ± 0.08	23.5
F2	9.04 ± 0.63	2.12 ± 0.06	23.5
F3	8.68 ± 0.50	2.00 ± 0.04	23.8
F4	2.79 ± 0.12	2.08 ± 0.03	50.8

Notes: ^a γ -ray in units of $\times 10^{-7}$ photon $\text{cm}^{-2} \text{s}^{-1}$

MJD 55100.3 with a flare amplitude of $(9.42 \pm 1.21) \times 10^{-7}$ photon $\text{cm}^{-2} \text{s}^{-1}$. The next flares are fitted together with the same constant level of the flux to reduce the number of free parameters. These flares reach the peaks within 11.34 ± 2.85 and 9.21 ± 2.43 days, respectively, then the second one quickly drops to its average level within 3.64 ± 1.24 days while the decay of the other flare is relatively slow, 7.66 ± 2.19 (Table 4.1). The time peak of the flares are at MJD 55899.5 and MJD 56175.98 with amplitudes of $(13.41 \pm 2.67) \times 10^{-7}$ and $(11.85 \pm 2.00) \times 10^{-7}$ photon $\text{cm}^{-2} \text{s}^{-1}$, respectively. The shortest flux doubling or halving timescales, computed by $t_{r,d} \times \ln 2$, is ~ 2.34 days.

The arrival time of the highest-energy events (> 5 GeV) from the direction of B3 1343 + 451, calculated using the *gtsrcprob* tool, is shown in the lower panel of Figure 4.1. The HE photons are mostly at MJD 55720 -57230; the maximum 50.3 GeV is at MJD 55884 with a 2.6σ probability is associated with B3 1343+451.

SWIFT XRT/UVOT DATA ANALYSES: B3 1343+451 was observed three times by *Swift*, in 2009 and in 2014. The data from two of the instruments onboard *Swift*, the UltraViolet and Optical Telescope (UVOT) and from the X-Ray Telescope (XRT), have been analyzed. The Swift-XRT observations were made in the photon counting mode and the source count rate was always below $0.5 \text{ counts s}^{-1}$, so no pile-up correction was necessary. The data were analyzed using the XRTDAS software package distributed by HEASARC as part of the HEASoft package (v.6.25). The source spectrum region was defined as a circle with a radius of 20 pixels (47") at the center of the source, while the background region was defined as an annulus centered at the source with its inner and outer radii being 51 (120") and 85 pixels (200"), respectively. The Cash statistics [71] on ungrouped data was used; the individual spectra in the 0.3-10.0 keV range were fitted with XSPEC v12.10.1, adopting an absorbed

power-law model with $N_{\text{H}} = 1.78 \times 10^{20} \text{cm}^{-2}$ column density. Unfortunately, the number of counts in the single observations was relatively low, ~ 30 , not allowing to estimate the parameters with a statistical significance. For example, for Obsid 38469006, the X-ray photon index and flux have been estimated to be 1.43 ± 0.27 and $(6.57 \pm 2.41) \times 10^{-13} \text{erg cm}^{-2} \text{s}^{-1}$, respectively. In order to increase the photon statistics, three sequential observations made in January 2014 (Obsid 38469004, 38469005 and 38469006) as well as two sequential observations made in October 2009 (Obsid 38469002 and 38469003) were merged to obtain the averaged X-ray spectra of the source in two different years. As a result, the X-ray photon index was 1.35 ± 0.29 in 2009 and 1.20 ± 0.21 in 2014. Similarly, the fluxes in 2009 and 2014 were $(4.06 \pm 1.19) \times 10^{-13} \text{erg cm}^{-2} \text{s}^{-1}$ and $(7.54 \pm 1.64) \times 10^{-13} \text{erg cm}^{-2} \text{s}^{-1}$ respectively. Even if the photon index did not change significantly, taking into account the uncertainties, there had been a slight increase in the X-ray flux in 2014.

In the analysis of the Swift UVOT data, the source counts were extracted from an aperture of 5.0" radius around the source while the background counts were taken from the neighboring circular region having a radius of 20" and not being contaminated by nearby sources. The magnitudes were computed using the *uvotsource* tool (HEASOFT v6.25) then corrected [70] using the reddening coefficient from the Infrared Science Archive⁷. Like the XRT data analyses, the sequential observations made in 2009 and 2014 were merged to

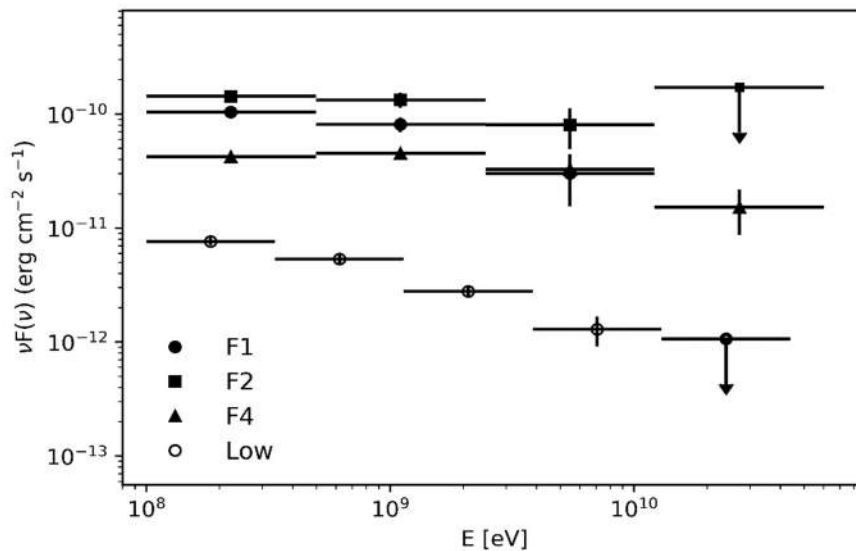


Figure 4.3 The γ -ray spectra of B3 1343+451 for flaring (F1, F2 and F4) and low states.

⁷ <https://irsa.ipac.caltech.edu/applications/DUST/>

reduce the flux estimation uncertainties. The optical/UV flux derived in these two periods is shown in Figure 4.4.

SPECTRAL ANALYSES: For the spectral analyses the data from the following periods are considered:

Low state: MJD 55125-55722, when the source was not flaring in the γ -ray and had a typical average flux.

Flare 1 (F1): MJD 55096.5-55102.5, corresponding to the highest peak of the flare on MJD 55100, coinciding with the Swift observations in 2009.

Flare 2 (F2) and Flare 3 (F3): 3 days period centered on MJD 55893 and on MJD 56175, corresponding to bright γ -ray states.

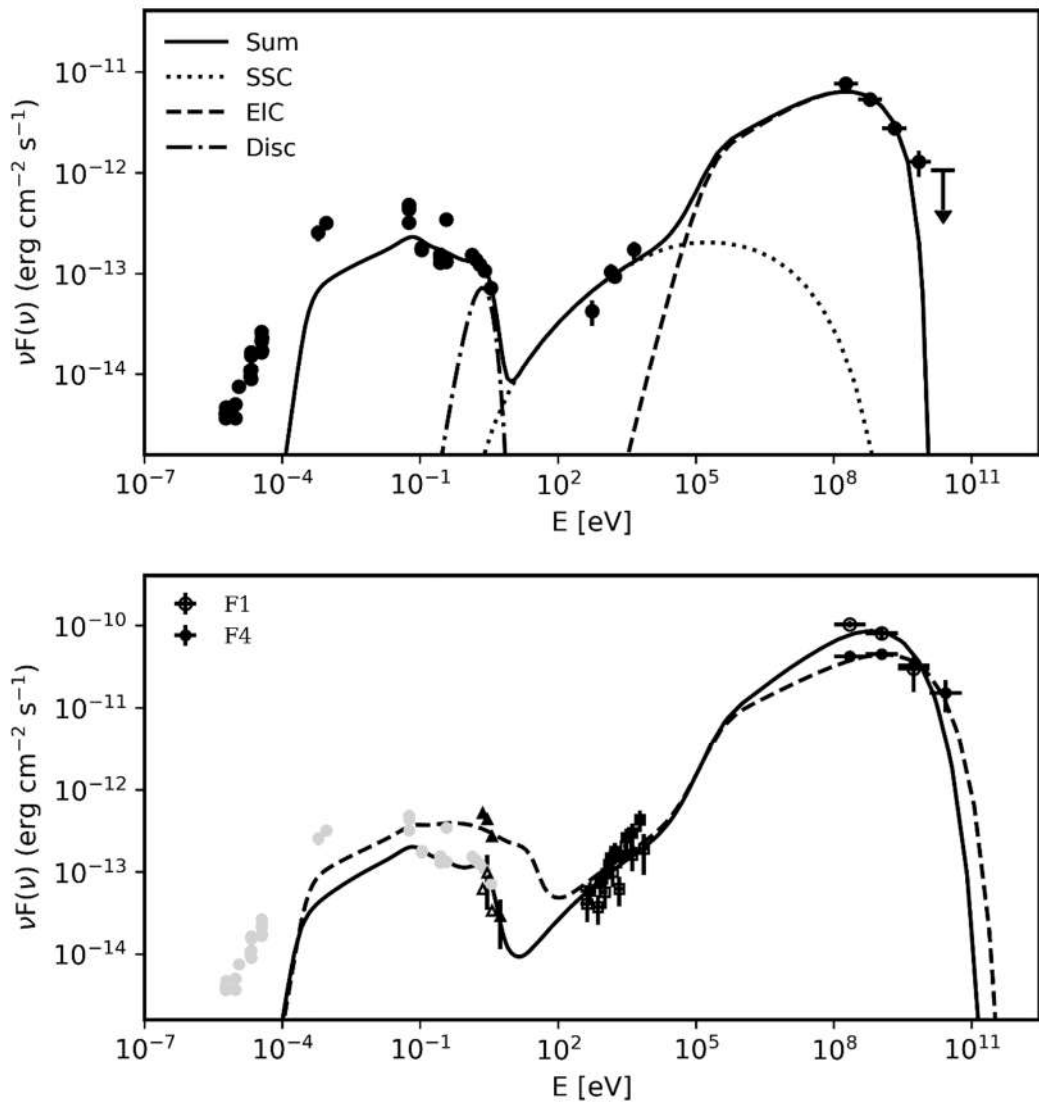


Figure 4.4 Modeling of the broadband SEDs of B3 1343+451 during the quiescent (upper panel) and flaring states (F1 and F4 lower panel). The model parameters are given in Table 4.3.

Flare 4 (F4): MJD 56629.5-56707.5, corresponding to another flaring γ -ray state with available quasi-simultaneous Swift observation in 2014.

The spectrum of B3 1343+451 was modeled with a power-law function ($dN/dE \sim N_0 E^{-\alpha}$) with the normalization (N_0) and index (α) as free parameters. The best matches between the spectral models and events are obtained with an unbinned likelihood analysis implemented in *gtlike*. Then, the SEDs are calculated by fixing the power-law index of B3 1343 + 451 and running *gtlike* separately for smaller energy bins of equal width in the log scale. The corresponding spectra are shown in Figure 4.3 (except for F3 when the spectrum is similar to that of F2) and the results of analyses are given in Table 4.2 .

The γ -ray spectrum in all periods extends up to ~ 10 GeV (for F4 up to ~ 60 GeV). The photon index is soft during the low state, $\Gamma_\gamma = 2.46 \pm 0.05$, which hardens during the flaring periods. The hardest photon index of $\Gamma_\gamma = 2.00 \pm 0.04$ was observed during F3. During the F1, F2 and F3 flares, the source had a high flux of $(8.0 - 9.0) \times 10^{-7}$ photon $\text{cm}^{-2}\text{s}^{-1}$ which drops to $(2.79 \pm 0.12) \times 10^{-7}$ photon $\text{cm}^{-2}\text{s}^{-1}$ during F4. The flux at the low state is ~ 20 times lower and corresponding to the baseline flux of the source emission in the γ -ray band.

4.3 MODELING THE SED

The SED of B3 1343+451 during the quiescent (low), and flaring (F1 and F4) periods are shown in Figure 4.4. The γ -ray data are shown with black circles while for the F1 and F4 flares, the available optical/UV and X-ray data analyzed in Section 2 are shown with black triangles and squares, respectively. The data of F1 are shown with empty marks. The archival data from the ASI science data center are shown in gray. The broadband SED of B3 1343+451 shows a typical double-peaked structure: a low energy component, peaking in the optical through X-rays, originates from synchrotron emission of electrons and a high energy component, peaking in the γ -ray, probably originating from Compton scattering of the seed photon field, either internal (synchrotron self-Compton [SSC] [6, 5, 4]) or external to the jet (external Compton [EIC] [9, 7]). In all periods the ratio of the IC to synchrotron luminosity is larger than one. In the Thomson regime, this ratio approximately corresponds to $L_{\text{IC}}/L_{\text{S}} \sim U_{\text{photon}}/U_{\text{B}}$ where U_{photon} and U_{B} are the energy density of the photon and magnetic fields, respectively. $U_{\text{photon}} > U_{\text{B}}$ condition is satisfied when the density of the

Table 4.3: Parameters best describing the SEDs.

	Quiescent	F1	F4
δ	20	30	30
p	2.39	2.08	2.38
γ_{\min}	62.78	62.78	62.78
γ_{cut}	4683.34	4884.00	12095.01
$B(\text{G})$	0.18	0.04	0.10
$U_e(\text{erg cm}^{-3})$	0.10	0.13	0.09
$U_B(\text{erg cm}^{-3})$	1.34×10^{-3}	8.09×10^{-5}	3.61×10^{-4}
$L_e(\text{erg s}^{-1})$	1.12×10^{45}	1.51×10^{45}	1.04×10^{45}
$L_B(\text{erg s}^{-1})$	1.49×10^{43}	8.96×10^{41}	4.00×10^{42}

external photons exceed (photons from BLR or dusty torus) the density of synchrotron photons, so the HE component is entirely described by EIC scattering. It should be noted that SSC and SSC+EIC mechanisms were also successful in explaining the multiwavelength emission from radio galaxies [159, 69, 160]. Since the previous studies of bright FSRQs showed that the regions outside the BLR are more favorable for the γ -ray emission [67, 64], in this study we assume that the dissipation region of the jet R_{diss} is outside the BLR and infrared emission from dusty torus is the dominant external photon field. The SED of B3 1343+451 is modeled within the commonly applied one-zone emission scenario which assumes the broadband spectrum is produced from a single region of the jet during its propagation. Unlike the two-zone models, when the acceleration and emission of particles occur in different regions, in this case the accelerated electrons are cooling by synchrotron and IC emission in a compact spherical region of the jet (with a radius of R) which moves with relativistic velocities (Γ_{jet}). Thus, the emission will be boosted by $\delta = [\Gamma_{\text{jet}}(1 - \beta \cos\theta)]^{-1}$ ($\delta = \Gamma$ for small θ), and will appear brighter for the observer. The analyses of a large sample of γ -ray emitting FSRQs show that bright blazars have a mean bulk Lorentz factor of $\Gamma > 15$ [103], so for B3 1343+451 we assume $\delta = 20$. The radius of the emitting region can be inferred from the observed flux doubling timescale of ~ 2.34 days from the $R \leq \delta \times c \times t/(1 + z) = 3.43 \times 10^{16} \text{cm}$ relation. This region carries a magnetic field with an intensity of B and a population of relativistic electrons for which a power-law with exponential energy distribution,

$N_e(\gamma_e) \sim (\gamma_e)^{-p} \text{Exp}[-\gamma_e/\gamma_{\text{cut}}]$ within γ_{min} and γ_{max} , is assumed. This electron spectrum is naturally formed within the first-order Fermi acceleration (diffuse shock acceleration [107, 87]), under dominant radiative cooling and/or a decreasing chance for HE particles to cross the shock front a large number of times. The EIC scattering of external photons is taken into account assuming that the IR radiation from the dusty torus which has a blackbody spectrum with a luminosity that scales with the disc luminosity as ηL_{disc} ($\eta = 0.6$ [161]) and fills a volume that for simplicity is approximated as a spherical shell with a radius of $R_{\text{IR}} = 2.5 \times 10^{18} (L_{\text{disc}}/10^{45}) \text{ cm}$ [161]. The disc luminosity is $L_{\text{disc}} = 5.38 \times 10^{45} \text{ erg s}^{-1}$, estimated by fitting the blue-bump seen in the data (Figure 4.4) which is the accretion disc emission component. The parameters best describing the data are estimated *through minuit optimization*⁸ [98, 97, 96].

THE SED IN QUIESCENT STATE: Initially, the SED in the quiescent state is modeled (Figure 4.4 upper panel) to estimate the baseline energy of the jet as well as the radiating particle energy distributions. The model parameters are given in Table 4.3. Since the radio emission is produced from the low-energy electrons which can diffuse larger distances, these data are not included in the fit and are considered as upper limits. In this case, the X-ray to γ -ray data is interpreted as IC up-scattering of synchrotron (dot-dashed line in Figure 4.4 upper panel) and torus (dashed line in Figure 4.4 upper panel) photons. The absence of high-quality X-ray data hardens the precise estimation of the power-law index of the electrons and $p = 2.39$ is defined by SSC fitting to X-ray data. When $\gamma_{\text{min}} = 62.78$, $\gamma_{\text{cut}} = 4683.34$ and $\gamma_{\text{max}} = 1.04 \times 10^4$, the EIC component peaks around GeV energies, explaining the γ -ray data. In the emitting region, the magnetic field is $B = 0.18 \text{ G}$ with a density lower than that of electrons $U_e/U_B = 74.6$ which implies that even if the system is not perfect in equipartition ($U_e/U_B = 1$), there is no large deviation between electron and magnetic field energy densities (for some blazars U_e/U_B can be as high as 1000).

THE SED IN THE FLARING STATES: The multiwavelength SEDs during the flaring states are shown in Figure 4.4 (lower panel). In the flaring states, the γ -ray flux significantly increased making the Compton dominance of the source stronger and evident. Such amplification of

⁸ <https://jetset.readthedocs.io/en/latest/>

the emission spectra can be due to changes either in the emission region parameters, e.g., in the magnetic field, emitting region size, bulk Lorentz factor and others, and/or particle energy distribution. In principle, if the emission comes from a newly formed blob (e.g., ejected from the accretion disc) all the parameters describing the emitting region can be changed at the same time. To claim such global changes in the jet, sensitive radio observations are required which are missing in this case. The evolution of multiwavelength emission spectra in dependence with various parameters is performed in Paggi et al. [85]. Their Fig.1 (e) shows that large magnitude variations are possible in the γ -ray band when the bulk Lorentz factor of the emission region increases. This is evident especially in the case of EIC scenario, since the density of external photons in the comoving frame of the jet depends on the Doppler boosting factor (δ^2). Thus, in order to model the SEDs observed during the flaring periods, we assume that the Doppler boosting factor has increased and corresponds to $\delta = 30$.

During the fit, all the parameters describing the source (e.g., the luminosity of the torus, its radius, temperature, etc.) are fixed to the values obtained during the fit of the averaged state, while the parameters of the magnetic field and emitting electrons are left free to vary. Also, γ_{\min} was fixed since it is obtained by requiring the model does not overproduce the radio data which are the same in all cases. X-ray to γ -ray data are again interpreted by the sum of SSC and EIC components (for the clarity only the sum of these components is depicted in Figure 4.4 lower panel) and the X-ray spectra can be explained when $p = 2.08$ and $p = 2.38$ for the flares F1 and F4, respectively. As the γ -ray spectrum during F4 is characterized by a harder photon index which extends to higher energies, larger $\gamma_{\text{cut}} = 12095.01$ is estimated as compared with F1 ($\gamma_{\text{cut}} = 4884.00$). In order to account the increase on the γ -ray flux, higher energy densities of electrons are estimated (see Table 4.3) which results in lower magnetic field (0.04 and 0.10 for F1 and F4, respectively) to keep the flux of the lower component at the same level since the synchrotron emission depends on the total energy of electrons and magnetic field. During the flaring states, the jet of B3 1343+451 becomes more particle dominated with $U_e/U_B > 900$, which is natural considering the ratio of IC to synchrotron luminosity increases.

JET ENERGETICS: The jet power in the form of the magnetic field and electron kinetic energy

is calculated by $L_B = \pi c R_b^2 \Gamma^2 U_B$ and $L_e = \pi c R_b^2 \Gamma^2 U_e$, respectively (presented in Table 4.3). The jet luminosity on the form of the magnetic field (L_B) decreases from $1.5 \times 10^{43} \text{ erg s}^{-1}$ to $9.0 \times 10^{41} \text{ erg s}^{-1}$ while L_e does not vary much, remaining around $1.5 \times 10^{45} \text{ erg s}^{-1}$. This is because at flaring states the energy distribution of electrons extends to larger energies, i.e., has a larger γ_{cut} and or harder p , implying the total energy is distributed in more electrons.

4.4 RESULTS AND DISCUSSION

The results from γ -ray observations of the distant blazar B3 1343+451 from 2008 to 2018 are presented. The source was alternatingly in its active state, showing several prominent γ -ray flares. Starting from MJD 55720, within 500 days, the source was in a very active state when also its averaged flux increased as compared with normal states. During this period also two bright flares were observed, when the peak flux measured within a 3-day interval was $(8.78 \pm 0.83) \times 10^{-7} \text{ photon cm}^{-2} \text{ s}^{-1}$ with a photon index of $\Gamma = 2.02 \pm 0.07$ observed on MJD 56175. This corresponds to isotropic γ -ray luminosity of $L_\gamma = 5.63 \times 10^{49} \text{ erg s}^{-1}$ for the distance of B3 1343+451 (21.04 Gpc). This is of the same order with the highest luminosity of FSRQs observed in the γ -ray band so far. There is no evident variability of the γ -ray photon index but a period when $\Gamma = 1.73 \pm 0.24$ was observed on MJD 58089, which is not common for FSRQs. Although hard photon indexes have been occasionally observed during rapid flaring events in FSRQs [78], they are usually characterized by > 2.3 indexes. The hard emission spectrum is most likely related to the emission of new energetic particles that were either injected into the emitting region or re-accelerated. However, the linear-Pearson correlation test did not result in a statistically significant correlation or anti-correlation between the flux and photon index which would allow testing one of the theories.

During the bright γ -ray flares, the time profile analyses showed an asymmetric profile of the flares which can be explained assuming that the particles are accelerated during the rising phase of the flare (e.g., by shock acceleration) and cool down or escape from the emitting region during the decay phase. This is in agreement with the observed Compton dominance, implying the density of the external photons in the jet's comoving frame increased. The observed shortest flux halving timescale is ~ 2.34 days, implying the emission is produced

from a very compact region of the jet.

The analyses of Swift XRT data contemporaneous with the γ -ray flares on 2009 and 2014 show that the X-ray flux increased on 2014, $(7.54 \pm 1.64) \times 10^{-13} \text{ erg cm}^{-2}\text{s}^{-1}$, as compared with that of 2009, but the photon index did not change significantly, being hard in both periods. The increase of the X-ray is related to the similar increase observed in the γ -ray band which is most likely due to changes in the acceleration and cooling of the electrons.

The SEDs observed during quiescent and flaring states are modeled within one-zone leptonic models assuming that the jet dissipation occurs outside the BLR and considering both synchrotron and external photons for the IC scattering. In all periods, the SSC component can explain the X-ray data but the data in optical/UV bands (at 10^{15} Hz) limits the emitting electron maximum energy, and the SSC component cannot reach the HE γ -ray band. Instead, the γ -ray data can be explained only by considering the IC scattering of dusty torus photons (EIC). In the quiescent state, the electrons should be effectively accelerated up to 2.39 GeV ($m_e c^2 \gamma_{\text{cut}}$) with the power-law index of 2.39 in order to explain the observed data, while during F4 it should be up to 6.18 GeV. This is because in this period the γ -ray spectrum with a hard spectrum extends to higher energies as well as in the optical/UV band the spectrum slightly increases and shifts to higher energies (see Figure 4.4 lower panel). In the quiescent state the jet of B3 1343+451 is not far from the equipartition with $U_e/U_B = 74.6$, while during the flares it is required that $U_e/U_B \geq 900$. This is natural, considering that during the flares the IC to synchrotron luminosities ratio is $L_{\text{IC}}/L_S \approx 150$. The flares are interpreted to be due to the changes in the bulk Lorentz factor, i.e., the contribution comes from a blob that moves faster. In this interpretation, the SEDs can be reproduced not changing the source parameters (e.g., torus luminosity, radius, etc.) but only varying the magnetic field and emitting electron parameters. As a result, the total jet luminosity estimated in the quiescent and flaring states is almost of the same order, supporting the assumption that the flares were caused by the change in the velocity of the emitting region rather than from a new energetically dominant component.

4.5 CONCLUSION

The origin of multiwavelength emission from B3 1343+451 during the quiescent and flaring

states is investigated. In the γ -ray band, the flux varies within ~ 2.34 days with a peak flux of $(8.78 \pm 0.83) \times 10^{-7}$ photon $\text{cm}^{-2}\text{s}^{-1}$. Also, the photon index hardens as compared to its average value during the bright γ -ray periods.

The modeling of the SED of B3 1343+451 in the quiescent state allowed to constrain the properties of the jet when it is in the average emission state. The SED observed during the flares can be reproduced by changing the bulk Lorentz factor of the emission region and slightly changing the energy distribution of the emitting electrons, the total luminosity of the jet being constant. This implies that the flares are most likely produced in a different region as compared to the average state which does not dominate energetically but contains more energetic electrons.

In this thesis, two flaring periods of B3 1343+451 were modeled providing information on the properties of the source jet. Identification of flaring periods in other distant blazars and their theoretical modeling can help to understand the physics of distant blazar jets.

5 MULTIWAVELENGTH PROPERTIES OF SELECTED HIGH REDSHIFT BLAZARS

5.1 INTRODUCTION

Blazars are the dominant sources in the extragalactic γ -ray sky. Because of the relativistic amplification of their emission, sources even at high redshift are observed. For example, Fermi-LAT 12-Year Point Source Catalog (data release 3 (DR3); [162]) contains 38 blazars detected beyond $z = 2.5$ and 11 beyond $z = 3.0$. The investigation of multiwavelength properties of these high redshift blazars is especially important as they are the most powerful non-explosive astrophysical sources and their study can be crucial for understanding the jet formation and propagation around supermassive black holes.

Sahakyan et al. [122] already studied the multiwavelength characteristics of the majority of high redshift blazars (33) detected in the HE γ -ray band, with a redshift greater than 2.5. The selection of high redshift blazars in Sahakyan et al. [122] was based on the first eight years of Fermi-LAT observations, while the most recent available Fermi-LAT catalogue is now based on 12 years of data. Therefore, there are additional 7 sources which are newly classified as high redshift blazar. The list of these objects is given in Table 5.1 for each source providing its name, 4FGL associated name, its type and redshift. In order to investigate the multi wavelength properties of these newly classified high redshift blazars, the data accumulated from their observations in the optical/UV, X-ray and γ -ray bands was analyzed and the results were modeled within leptonic scenario.

Table 5.1: List of γ -ray emitting blazars with redshift beyond 2.5.

Associated name	4FGL name	Class	z
PKS 1830-211	J1833.6-2103	FSRQ	2.507
LQAC 247-061	J1628.8-6149	FSRQ	2.578
4C +41.32	J1625.7+4134	FSRQ	2.550
PKS 2311-452	J2313.9-4501	BCU	2.884
PMN J0833-0454	J0833.4-0458	FSRQ	3.450
PKS 2318-087	J2320.8-0823	FSRQ	3.164
TXS 0536+145	J0539.6+1432	FSRQ	2.690

5.2 DATA ANALYSIS

In the γ -ray band the selected sources were continuously monitored with Fermi-LAT since 2008. Also, they were observed multiple times in the optical/UV and X-ray bands with Swift telescope. All the available data in the mentioned bands were downloaded and analyzed to investigate the multiwavelength properties of the selected sources.

FERMI-LAT DATA ANALYSIS: As mentioned above onboard the Fermi Gamma-ray Space Telescope LAT is a pair-conversion telescope operating in the energy range from 30 MeV to 500 GeV. It scans the entire sky every ~ 3 hours, continuously monitoring the γ -ray emission from Galactic and extragalactic sources. More details on LAT instrument are given in Atwood et al. 2009 [123].

In the current study, the data accumulated between 2008 August 04 to 2022 December 04 (MET 239557417-691804805) were downloaded and analyzed using the standard Fermi ScienceTools version 1.2.1. The data was processed using the P8R3_SOURCE_V3 instrument response function for the PASS 8 data. The events in the energy range from 100 MeV to 500 GeV were downloaded from 12° region of interest (ROI) centered on the position of each source. In *gtselect* tool with a filter '*evclass 128*', '*evtype=3*' only the events which have high probability of being photons were selected. Also, a filter of zenith angle $>90^\circ$ was applied to remove contamination by photons from Earth's atmosphere. In the *gtmktime* tool a filter of "*(DATAQUAL > 0) &&(LATCONFIG==1)*" was applied to select good time intervals. Then the events are binned into $16.9^\circ \times 16.9^\circ$ square region into pixels of $0.1^\circ \times 0.1^\circ$ and into 37 equal logarithmically spaced energy bins with *gtbin* tool. For each source, the model file which describes the sources included in the region of interest was created using the Fermi-LAT fourth source catalog Data Release 3 (4FGL-DR3) [120]. The significance of the source detection is quantified using test statistic (TS), defined as $TS = 2\log(L_1/L_0)$, where L_0 and L_1 are the likelihoods of the model without source (null hypothesis) and the alternative likelihood (with source), respectively. The model file includes all sources within ROI $+ 5^\circ$ around the targets; the spectral parameters of the other sources which are within the ROI were left free while those that are outside were fixed to their catalog values. The model file includes also diffuse and isotropic backgrounds, which were modeled with standard *gll_iem_v07* and

iso_P8R3_SOURCE_V3_v1 models with the normalization considering as a free parameter. The entire data was initially analyzed using a binned maximum likelihood analysis implemented in *gtlike* tool.

After analyzing the data from the entire period, the γ -ray variability of the selected sources was investigated. Initially, the whole time period was divided into short equal periods and the unbinned likelihood analysis was applied to estimate the flux and the photon index. The duration of the time bin was selected based on the overall detection significance of the source. In general, several tens of days were selected to ensure that periods with source detection exceed the periods for which only upper limits were observed. As a next step, in order to better investigate the evaluation of γ -ray flux in time, the light curves were computed with the help of adaptive binning method. In this approach the time bin widths are non-equal and are defined by requiring a constant relative flux uncertainty. This implies that during the low flux state the time bins are longer instead are narrower when the source is in a flaring state. So, these light curves are informative allowing to investigate the flux variations in short time scales and identify flaring periods [67, 65, 69, 66, 134, 163].

The γ -ray light curves of selected sources are shown in Figure 5.1. For each source, when the light curve generated with adaptively binning method is with a reasonable time bins, the light curves generated with fixed bins (circle) and with adaptive bins are shown. The light curves for PKS 1830-211 and LQAC 247-061 were downloaded from the Fermi-LAT Light Curve Repository, as the ROI around these sources contain a lot of objects making difficult the analysis. The most variable source in the sample is PKS 1830-211 (see panel a in Figure 5.1) which shows high amplitude flux changes in 3-day binned light curve. The γ -ray emission of this source increases time to time but the largest flare was observed during MJD 58572-58605 when the flux increased up to $(1.74 \pm 0.04) \times 10^{-5}$ photon $\text{cm}^{-2}\text{s}^{-1}$ on MJD 58596.49. It should be noted that average flux of γ -ray emission from this source is $(1.01 \pm 0.19) \times 10^{-6}$ photon $\text{cm}^{-2}\text{s}^{-1}$ so the flux increases ~ 17.22 times. The time averaged γ -ray spectrum of PKS 1830-211 is well explained with the index of $\Gamma_{\gamma} = 2.66 \pm 0.34$ but during the brightening the hardest index of $\Gamma_{\gamma} = 2.22 \pm 0.03$ was observed on MJD 58596.49. The γ -ray light curve of LQAC 247-061 with 7-day bins shows (panel b in Figure 5.1) several flaring

periods although with smaller amplitudes as compared to PKS 1830-211: the maximum weekly flux of this source was $(5.87 \pm 1.34) \times 10^{-7}$ photon $\text{cm}^{-2}\text{s}^{-1}$ observed on MJD 59222.42. The adaptively binned light curve of TXS 0536+145 above 285.38 MeV (panel c Figure 5.1) shows that the source was in active emission state between MJD 55872-56138 when the flux above 285.38 MeV increased up to $(1.81 \pm 0.39) \times 10^{-7}$ photon $\text{cm}^{-2}\text{s}^{-1}$ on MJD 55945.22. On average the γ -ray spectral index of this source is around $\Gamma_{\gamma} = 2.68$ but during the flares occasionally it hardens, for example on MJD 56014.81 the index was $\Gamma_{\gamma} = 2.00 \pm 0.16$. Among the considered sources, the light curve generated with the help of adaptive binning method shows also 4C+41.32 has variable γ -ray emission (panel d in Figure 5.1); the averaged γ -ray flux of the source was $(3.24 \pm 0.94) \times 10^{-9}$ photon $\text{cm}^{-2}\text{s}^{-1}$ which increases up to $(5.75 \pm 0.12) \times 10^{-9}$ photon $\text{cm}^{-2}\text{s}^{-1}$ on MJD 56177.66. It should be noted that during this bright period the photon index hardened being $\Gamma_{\gamma} = 2.10 \pm 0.11$. For the other remaining three sources (PKS 2311-452, PKS 2318-087 and PMN J0833-0454) no flux changes were observed in long- and short-time scales.

SWIFT OBSERVATIONS OF SELECTED SOURCES: With three instruments on board the spacecraft (UVOT, XRT and BAT) Swift satellite launched in 2004 is a good instrument to study the multiwavelength emission from blazars because of its wide energy coverage. These observations are especially crucial for high redshift blazars which typically have the peak of HE component at sub-MeV band, so the X-ray observations can help to constrain the increasing spectrum of the HE component.

Among the considered sources, TXS 0536+145, PMN J0833-0454, LQAC 247-061 and PKS 1830-211 were at least once observed by Swift satellite. All these available data from XRT and UVOT observations were downloaded and analyzed. The XRT data were all processed using the Swift_xrtproc automatic tool [140]. This tool automatically downloads the Swift data either from SSDC archive⁹ or from Swift UK archive¹⁰ and processes them applying the standard methods for the analysis. In particular, the Level 1 raw data was processed using the XRTPIPELINE script, which included reducing, calibrating, and cleaning the data using

⁹ <https://www.ssdsc.asi.it>

¹⁰ <https://www.swift.ac.uk/archive/>

standard filtering criteria and the latest CALDB calibration files. The sources' counts were obtained from a circular region of a 20-pixel radius (47") centered on the sources' position, while background counts were taken from an annular ring centered at the source. Finally, the ungrouped data was loaded into XSPEC version 12.11 for spectral fitting, where the source spectrum was modeled as a power-law with Galactic absorption column density obtained from the N_{H} HEASARC tool¹¹ [164, 165, 166].

The Swift XRT data analysis results are presented in Table 5.2. For the sources TXS 0536+145 and LQAC 247-061, each have only 3 observations when the count rate was above 20 so the spectral analysis was executed and for PMN J0833-0454 only 2. The 2.0-10 keV X-ray flux of PMN J0833-0454 is at the level of $1.86 \times 10^{-13} \text{ erg cm}^{-2}\text{s}^{-1}$ instead the spectral index is $\Gamma_x = 1.90 \pm 0.53$ and $\Gamma_x = 2.17 \pm 0.47$ which is unusually soft for FSRQs. However, it should be noted that the peak of the synchrotron component of PMN J0833-0454 at higher frequencies between $10^{14} - 10^{15} \text{ Hz}$ which is not typical for FSRQs. Similarly, the 2.0-10 keV X-ray flux of TXS 0536+145 and LQAC 247-061 is between $(0.91 - 2.28) \times 10^{-12} \text{ erg cm}^{-2}\text{s}^{-1}$ and $(1.00 - 1.79) \times 10^{-12} \text{ erg cm}^{-2}\text{s}^{-1}$, respectively and their indexes are 1.45 – 1.88 and 1.05 – 1.39, respectively. PKS 1830-211 is the most variable source in the X-ray band; the variation of 2.0-10 keV X-ray flux and photon index is shown in Figure 5.2. In different observations the change of the flux is evident, the highest flux of $(2.41 \pm 0.44) \times 10^{-11} \text{ erg cm}^{-2}\text{s}^{-1}$ was observed on MJD 58583.10. The spectral index in the X-ray band is relatively hard changing from 0.34 ± 0.14 to 0.94 ± 0.25 (lower panel in Figure 5.2), so it defines the rising spectrum of the HE component.

Along with XRT observations, the considered sources were observed also in optical/UV bands with UVOT instrument. The Swift-UVOT data in six different filters, including three optical (V, B, and U) and three ultraviolet (W1, M2, and W2), was processed using the latest version of HEASoft, 6.29, and the HEASARC CALDB. A 5-arcsec radius region centered at the source was used to extract the source counts, while background counts were obtained from a region of 20-arcsec radius located away from the source. The uvotsource tool was used to determine the magnitude of the data, which was then corrected for effects of

¹¹ <https://heasarc.gsfc.nasa.gov/cgi-bin/Tools/w3nh/w3nh.pl>

reddening and galactic extinction using the $E(B-V)$ reddening coefficient available from the Infrared Science Archive¹². Among the considered sources, TXS 0536+145, PMN J0833-0454 and LQAC 247-061 are relatively weak in the optical/UV bands and no measurements were available.

Instead, PKS 1830-211 even being observed more than 90 times, at its position RA=278.42, Dec=-21.06 no significant counts are observed, however a significant source at the position of RA=278.42, Dec=-21.059 is present; however, no obvious association with PKS 1830-211 is available. Considering the complex nature of PKS 1830-211 and the region of the sky (it is possible microlensing/milli-lensing substructures with two foreground lensing galaxies), in

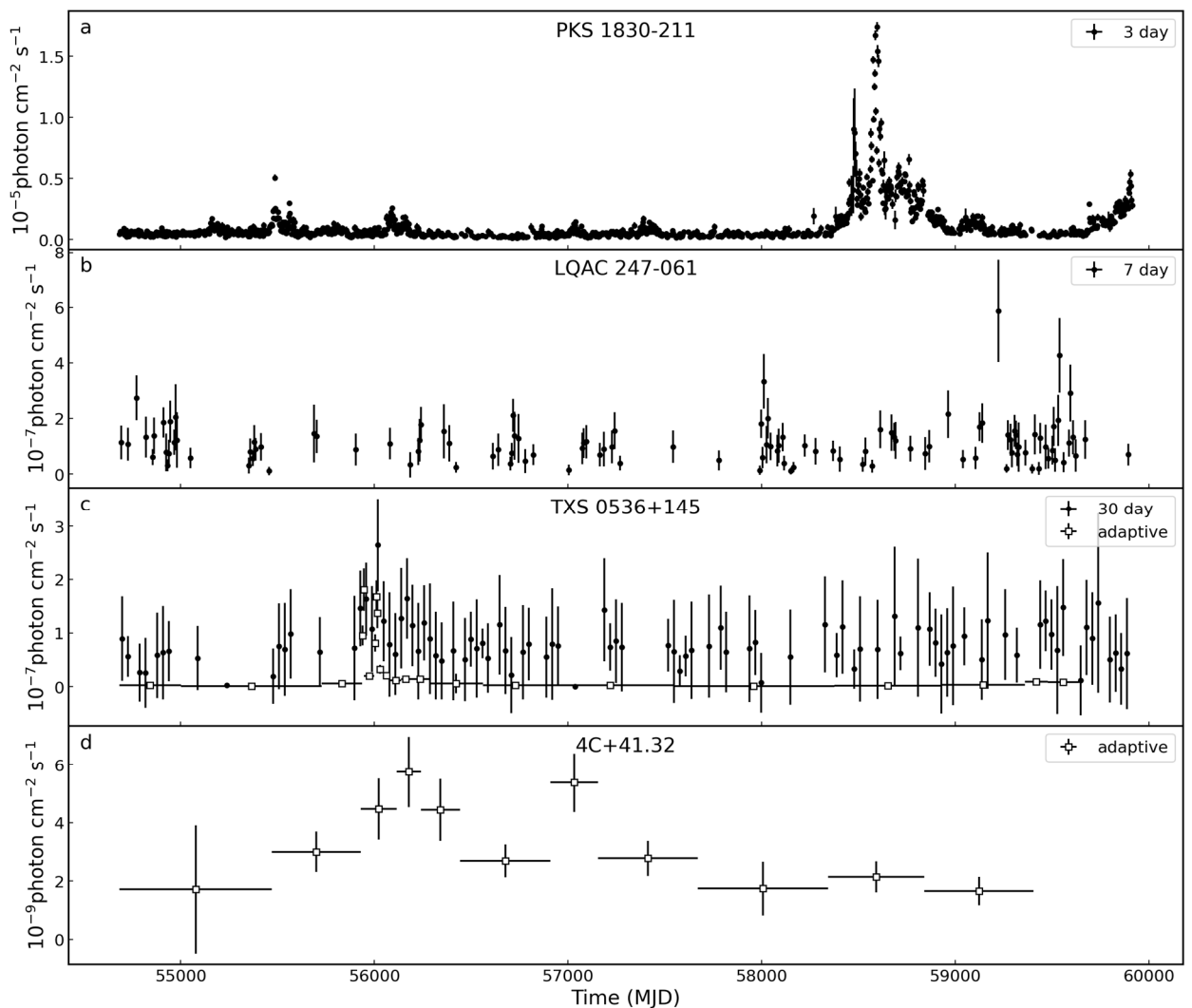


Figure 5.1 The γ -ray light curve of selected sources. The light curves generated with the help of adaptive binning are shown as empty squares while circles are regular/normal time binning.

¹² <http://irsa.ipac.caltech.edu/applications/DUST/>

order to avoid possible miss-association of the UVOT observations we dropped the UVOT data for this object.

5.3 MODELING OF MULTIWAVELENGTH SEDS

In order to investigate the origin of broadband emission from the considered sources, the data analyzed here were combined with the archival data retrieved using VOU-blazar tool [141]. This tool access over 70 catalogs and databases world-wide and returns all the available multifrequency data. The SEDs composed with data retrieved from VOU-blazar tool and analyzed here, are shown in Figure 5.3. Since no X-ray measurements are available for PKS 2311-452 and PKS 2318-087, they were not considered during the modeling.

All the considered sources shown the characteristic double peaked structure which is modeled within leptonic one-zone scenario. In this scenario, the electrons are injected and interact with a spherical region of radius R . The emitting region contains a tangled magnetic field of intensity B . This magnetized region, moves along the jet with a bulk Lorentz factor of Γ_{jet} making an angled of θ relative to the observer's line of sight.

For a small viewing angle, the emission is amplified by a beaming factor of $\Gamma_{\text{jet}} = \delta$. It is assumed that the emitting electrons have a power-law with an exponential cutoff energy distribution in the form of,

$$N(\gamma_e) = N_0 \gamma_e^{-p} \text{Exp}(-\gamma_e/\gamma_{\text{cut}}), \quad \gamma_e > \gamma_{\text{min}} \quad (5.1)$$

where p is the power-law index of the electrons, γ_{cut} is the cut-off energy and γ_{min} is the minimal energy. The total energy of the electrons (consequently, N_0 as well) is considered as a free parameter during the fitting.

In this interpretation, the first peak in the SED is accounted for by synchrotron radiation produced as a result of the interaction between the relativistic electrons and the magnetic field within the emitting region. The second peak, ranging from X-rays to HE γ -rays, arises from the IC scattering of synchrotron (SSC [6, 5, 4]) and BLR [67, 64] photons. The BLR is modeled as a spherical shell with a lower boundary of $R_{\text{in}} = 0.9 \times R_{\text{BLR}}$ and an outer boundary of $R_{\text{in}} = 1.2 \times R_{\text{BLR}}$ where $R_{\text{BLR}} = 10^{17} \times L_{\text{BLR}}/10^{45} \text{erg s}^{-1}$ [103]. It is assumed that L_{BLR} corresponds to 10% of the disk luminosity (L_{disk}). The disk emission is approximated as a mono-temperature black body which estimated by modeling the blue bump in the optical/UV

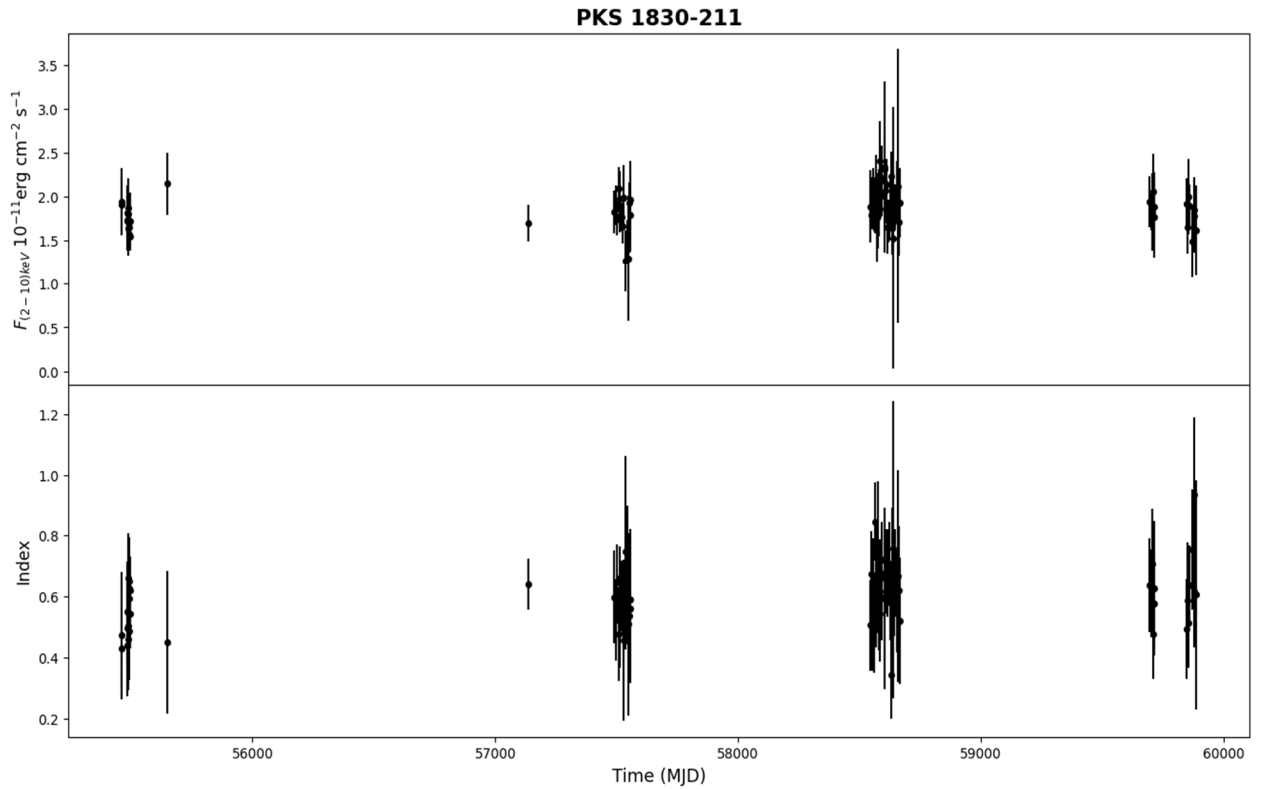


Figure 5.2 The variation of 2.0-10 keV X-ray flux and 0.3-10.0 keV X-ray photon index of PKS 1830-211.

band, if visible. An upper limit is derived by ensuring that the disk emission does not exceed the non-thermal emission observed from the jet, when the additional UV component is not distinguished.

During the SED modeling the free parameters to estimate are N_e , p , γ_{\min} , γ_{cut} , δ , R and B . These parameters were optimized, i.e., to find the optimal values of parameters best describing the data, using a publicly available code JetSet [98, 97, 96, 147].

RESULTS OF THE MODELING: The SEDs modeled with the synchrotron/SSC plus external Compton scattering of BLR photons is shown in Figure 5.3 and the corresponding parameters are in Table 5.3. The presented SEDs have sufficient data spanning from radio (archival) to HE γ -ray bands (analyzed here), which allows for shaping of both low and high energy peaks. The model utilized is able to effectively explain the multiwavelength data for nearly all of the sources.

There is discrepancy for PKS 1830-211, the low energy data are underestimated by the applied model. However, 1) the region around this source is rather complex so maybe some of the data are contaminated by the contribution from other sources and 2) the magnetic field and electron content (both affecting synchrotron component) are strongly constrained by the

Table 5.2: Swift XRT analysis results.

Object	Observation ID	Date	$F_{(2.0-10)\text{keV}}$	Index	C-Stat(d.o.f.)
PMN J0833-0454	00034962002	2017-12-13	0.17 ± 0.37	2.17 ± 0.47	0.98(34)
PMN J0833-0454	00034962003	2017-12-17	0.19 ± 0.23	1.91 ± 0.53	0.87(26)
LQAC 247 -061	00085339012	2015-05-08	1.78 ± 0.7	1.05 ± 0.47	0.83(37)
LQAC 247 -061	00085339014	2015-05-13	1.36 ± 0.47	1.39 ± 0.36	0.88(55)
LQAC 247 -061	00085339020	2015-06-03	1.02 ± 0.38	1.08 ± 0.4	0.77(55)
TXS 0536+145	00032331001	2012-04-04	2.28 ± 0.6	1.49 ± 0.32	1.14(75)
TXS 0536+145	00032331002	2012-04-18	0.91 ± 0.4	1.88 ± 0.36	0.99(58)
TXS 0536+145	00032331003	2012-11-15	1.4 ± 0.6	1.45 ± 0.31	0.62(79)
PKS 1830-211	00081222001	2015-04-25	17.01 ± 2.12	0.64 ± 0.08	1.77(461)
PKS 1830-211	00038422024	2016-05-18	16.68 ± 2.0	0.57 ± 0.09	1.56(438)
PKS 1830-211	00038422016	2016-04-19	18.55 ± 1.85	0.54 ± 0.1	1.23(424)
PKS 1830-211	00038422022	2016-05-06	17.79 ± 1.85	0.66 ± 0.1	1.57(390)
PKS 1830-211	00038422028	2016-06-05	15.69 ± 1.65	0.55 ± 0.11	1.22(374)
PKS 1830-211	00038422014	2010-10-27	17.27 ± 3.15	0.54 ± 0.11	1.37(357)
PKS 1830-211	00038422021	2016-05-04	18.81 ± 2.19	0.53 ± 0.11	1.7(354)
PKS 1830-211	00038422023	2016-05-11	17.64 ± 1.61	0.6 ± 0.11	1.29(348)
PKS 1830-211	00038422070	2019-06-02	16.94 ± 1.84	0.64 ± 0.12	1.39(347)
PKS 1830-211	00038422013	2010-10-26	15.51 ± 1.69	0.62 ± 0.11	1.38(347)

XRT flux in units of $\times 10^{12} \text{ erg cm}^{-2} \text{ s}^{-1}$

X-ray and γ -ray data, so the increase of the synchrotron component will imply discrepancy with X-ray and γ -ray data. The modeling shows that multiwavelength data of PKS 1830-211, LQAC 247-061 and 4C+41.32 can be explained when the power-law index of emitting electrons is relatively hard, 1.79 ± 0.08 , 1.97 ± 0.08 , 1.74 ± 0.21 respectively. Whereas soft index of 2.96 ± 0.06 and 2.49 ± 0.07 , respectively, are required to explain the data of TXS

0536+145 and PMN J0833-0454. Because of this soft index, the fit resulted to higher value for the cut-off energy for those two sources, $(12.94 \pm 1.82) \times 10^3$ and $(8.57 \pm 0.76) \times 10^3$ respectively. The cut-off energy is estimated to be $(5.99 \pm 0.41) \times 10^3$, $(2.75 \pm 0.27) \times 10^3$ and $(1.62 \pm 0.14) \times 10^3$ for PKS 1830-211, LQAC 247-061 and 4C+41.32 respectively. The modeling shows that the magnetic field in the emitting region is within 0.1 – 15.8 G where the lowest magnetic field of 0.1 ± 0.01 G is estimated for PKS 1830-211 while maximum of 15.82 ± 1.74 G for LQAC 247-061. For the considered sources, the Doppler boosting factor varies in a small range of 12.28 – 14.58 which is typical value usually estimated for the FSRQs. The modeling allowed to estimate also variability time or the size of the emitting region. The variability time is order to sub-day scales for all the considered except for 4C +41.31 for which $t_{\text{var}} = 3.73$ days which corresponds to $R = 3.37 \times 10^{16}$ cm considering its redshift of $z = 2.55$.

By applying the model, it is possible to evaluate the luminosity of the jet. The jet power carried out by the electrons and magnetic field is computed using the relations $L_e = \pi c R_b^2 \Gamma^2 U_e$ and $L_B = \pi c R_b^2 \Gamma^2 U_B$, respectively. The corresponding values are given in Table 5.3. For all the considered sources, the jet is particle dominated with $L_e/L_B > 1$. The highest total luminosity of $L_{\text{tot}} = L_e + L_B = 3.17 \times 10^{46}$ erg s⁻¹ is estimate for PKS 1830-211 while PMN J0833-0454 has the lowest luminosity of 5.52×10^{44} erg s⁻¹. The modeling allows to put an upper limit on the disk luminosity requiring that it does not overproduce the synchrotron component. The disc luminosity varies in the range of $(0.01 - 9) \times 10^{46}$ erg s⁻¹.

5.4 SUMMARY

High redshift blazars are often studied in different bands providing substantial information on the processes responsible for particle acceleration as well as on the properties of jet plasma close to supermassive black holes. The high redshift blazars observations in HE and VHE γ -ray bands is also important, as it may provide information on the density of extragalactic background light. Up to now, 38 blazars are observed beyond the redshift of 2.5 which is sufficient enough to have in depth view of processes in those extreme objects.

In the current work, the multiwavelength emission properties of 7 high redshift blazars are investigated analyzing Fermi-LAT and Swift XRT/UVOT data accumulated between 2008-

Table 5.3: Parameters obtained from the modeling of multiwavelength SEDs. [1]: object name. [2] and [3]: the Lorentz factors corresponding to the minimum ($\times 10^2$) and cutoff energy ($\times 10^3$) of the electron distribution respectively. [4]: Magnetic field in units of G. [5]: Slope of electron energy distribution. [6]: Doppler factor. [7]: accretion disk luminosity (L_d) in units of $10^{46} \text{ erg s}^{-1}$ [8]:Variability time in unit of 10^{-1} day [9] and [10]: The power of the jet in the form of the relativistic electrons (L_e)and magnetic field (L_B) in units of $10^{45} \text{ erg s}^{-1}$ and $10^{43} \text{ erg s}^{-1}$.

Sources	γ_{\min}	γ_{cut}	B [G]	α	δ	L_d	t_{var}	L_e	L_B
[1]	[2]	[3]	[4]	[5]	[6]	[7]	[8]	[9]	[10]
PKS 1830-211	7.53 ± 0.32	5.99 ± 0.41	0.11 ± 0.0	1.79 ± 0.08	13.8 ± 0.31	0.55	9.23	30	0.07
LQAC 247-061	0.27 ± 0.03	2.75 ± 0.27	15.82 ± 1.74	1.97 ± 0.08	12.28 ± 0.84	9.00	2.18	0.21	55
TXS 0536+145	1.33 ± 0.07	12.94 ± 1.82	3.92 ± 0.21	2.96 ± 0.06	14.27 ± 0.63	0.34	3.66	0.68	16
4C +41.32	3.23 ± 0.56	1.62 ± 0.14	0.32 ± 0.03	1.74 ± 0.21	12.32 ± 0.77	0.01	37.3	2.05	6.58
PMN J0833-0454	0.69 ± 0.06	8.57 ± 0.76	9.44 ± 0.91	2.49 ± 0.07	14.58 ± 1.01	0.8	2.60	0.21	33.8

2022. Main findings can be summarized as follows:

- The γ -ray emission from PKS 1830-211, LQAC 247-061, TXS 0536+145 and 4C+41.32 varies in time. In the γ -ray band, the most variable source is PKS 1830-211 showing multiple periods of flux enhancement; the brightest flare was observed on MJD 58596.49 when the flux increased up to $(1.74 \pm 0.04) \times 10^{-5} \text{ photon cm}^{-2} \text{ s}^{-1}$.
- In several occasions the γ -ray spectral index of the considered sources hardened significantly. For example, on MJD 56014.81 the index of TXS 0536+145 was $\Gamma_\gamma = 2.00 \pm 0.16$ or $\Gamma_\gamma = 2.10 \pm 0.11$ index was observed for 4C+41.32 on MJD 56177.66.
- The most variable source in the X-ray band is PKS 1830-211. Its 2.0-10 keV flux increased up to $(2.41 \pm 0.44) \times 10^{-11} \text{ erg cm}^{-2} \text{ s}^{-1}$ on MJD 58583.10 and the X-ray photon index is very hard changing in the range of 0.34 – 0.94.
- The multiwavelength emission of PKS 1830-211, LQAC 247-061, TXS 0536+145 ,4C+41.32 and PMN J0833-0454 was modeled with one-zone leptonic scenario considering the IC scattering of both synchrotron and BLR photons. The power-law index of the emitting electrons is in the range of 1.79 – 2.96, the cut-off energy in $(1.62 – 12.94) \times 10^3$ and the

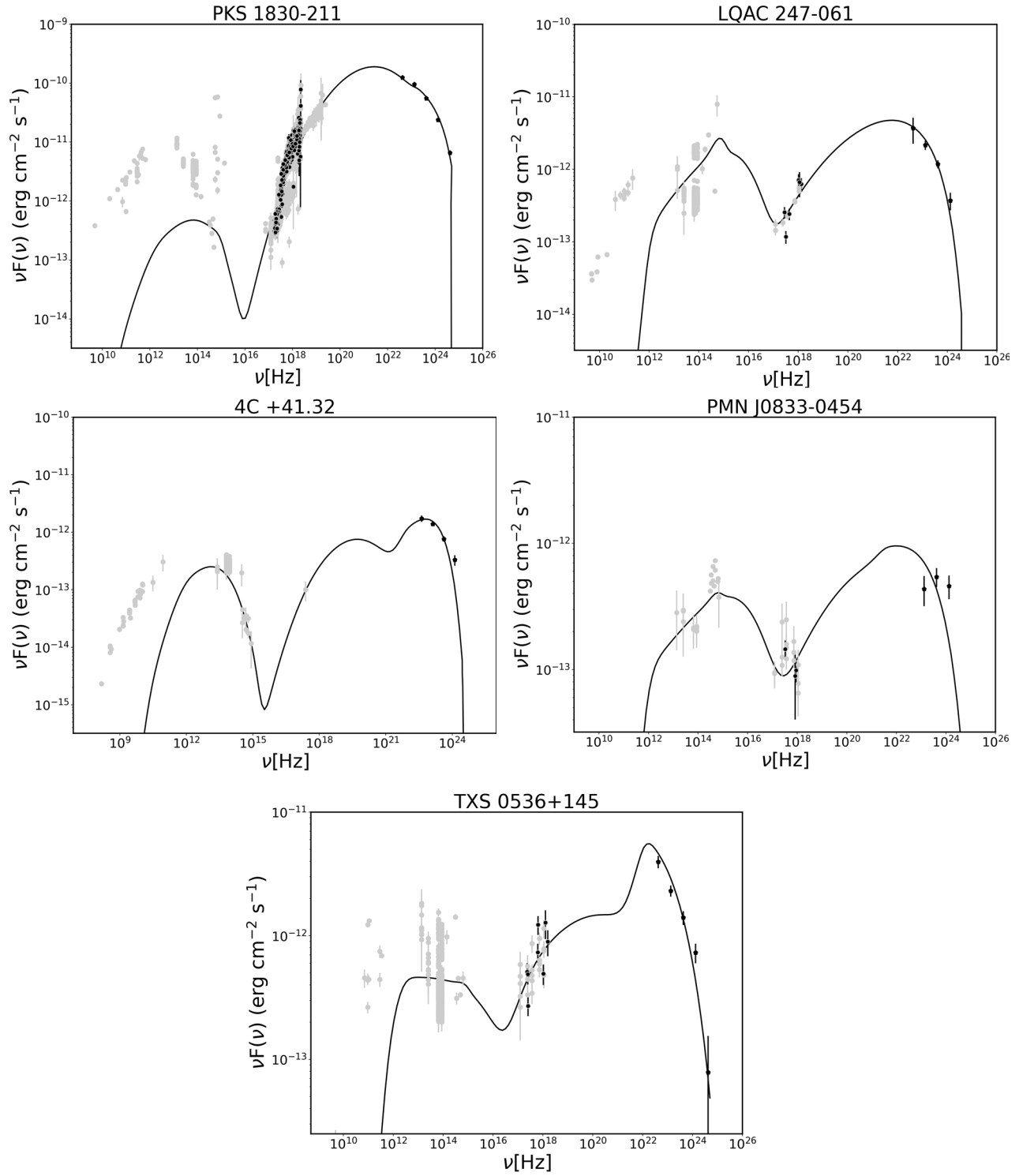


Figure 5.3 The modeling of multiwavelength SEDs of considered sources.

magnetic field in the emitting region is within 0.11 – 15.82.

- The modeling allowed to estimate the energetics of the jet of the considered sources. The total jet luminosity varies in the range of $(0.05 - 3.17) \times 10^{46} \text{ erg s}^{-1}$ and the disc luminosity (upper limit) is in the range of $(0.01 - 9) \times 10^{46} \text{ erg s}^{-1}$.

CONCLUSION

In this thesis the multiwavelength emission from high redshift blazars is investigated. These high redshift blazars are among the most powerful objects in the Universe and their study can help in understanding the evolution of blazars and relativistic jets in the early Universe.

The following results were obtained:

1. The multiwavelength properties of 33 distant blazars with redshifts greater than 2.5 is examined. It is found that the emission of several sources varies in different Swift XRT observations, and γ -ray emission varies for 14 sources. The one-zone leptonic model is used to estimate jet properties, finding the emission region size, magnetic field, and Doppler factor. Central black hole masses and accretion disk luminosities are also estimated.

2. A multi-frequency spectral and temporal study of high-redshift blazar PKS 0537-286 is conducted using data from Fermi-LAT, NuSTAR, Swift XRT, and UVOT. The flaring activities are attributed to hardening of the emitting electron spectral index and shifting of the cut-off energy to higher values. The most energy-efficient scenario is when the jet energy dissipation occurs within the BLR.

3. Multiwavelength observations of B3 1343+451, a distant and bright flat-spectrum radio quasar, reveal strong flares in the γ -ray band. The shortest flux halving timescale in the γ -ray band is of the order of 2.34 days indicating the emission originates from a compact region. The SED is modeled, explaining the flares by changes in the bulk Lorentz factor of the emitting region without significant modification of the emitting electron parameters and jet luminosity.

4. The origin of broadband emission from 7 high-redshift blazars is investigated, observing flaring periods with significant flux increases and photon index hardening in the HE γ -ray band. The time-averaged broadband SED is modeled using a one-zone leptonic emission mechanism, estimating the parameters of the emitting particles and the energetics of the jet.

In conclusion, these studies offer valuable insights into the properties and processes of high-redshift blazars and their jets, contributing to our understanding of the powerful phenomena occurring in the early Universe.

BIBLIOGRAPHY

- [1] U. C. Megan and P. Padovani, "Unified Schemes for Radio-Loud Active Galactic Nuclei," *Publications of the Astronomical Society of the Pacific*, vol. 107, p. 803, 1995.
- [2] M. Ackermann and e. al, "Minute-timescale >100 MeV γ -Ray Variability during the Giant Outburst of Quasar 3C 279 Observed by Fermi-LAT in 2015 June," *Astrophysical Journal*, vol. 824, p. L20, 2016.
- [3] V. Beckman and C. Shrader, "The AGN phenomenon:open issues," *Proceedings of Science*, vol. 176, p. 1, 2013.
- [4] G. Ghisellini, L. Maraschi and A. Treves, "Inhomogeneous synchrotron-self-compton models and the problem of relativistic beaming of BL Lac objects.," *Astronomy and Astrophysics*, vol. 146, pp. 204-212, 1985.
- [5] S. Bloom and A. Marscher, "An Analysis of the Synchrotron Self-Compton Model for the Multi--Wave Band Spectra of Blazars," *Astrophysical Journal*, vol. 461, p. 657, 1996.
- [6] L. Maraschi, G. Ghisellini and A. Celotti, "A Jet Model for the Gamma-Ray--emitting Blazar 3C 279," *Astrophysical Journal*, vol. 397, p. L5, 1992.
- [7] M. Błażejowski, M. Sikora, R. Moderski and G. Madejski, "Comptonization of Infrared Radiation from Hot Dust by Relativistic Jets in Quasars," *Astrophysical Journal*, vol. 545, pp. 107-116, 2000.
- [8] G. Ghisellini and F. Tavecchio, "Canonical high-power blazars," *Monthly Notices of the Royal Astronomical Society*, vol. 397, pp. 985-1002, 2009.
- [9] M. Sikora, M. Begelman and M. Rees, "Comptonization of Diffuse Ambient Radiation by a Relativistic Jet: The Source of Gamma Rays from Blazars?," *Astrophysical Journal*, vol. 421, p. 153, 1994.
- [10] K. Mannheim, "The proton blazar," *Astronomy and Astrophysics*, vol. 269, p. 67, 1993.

- [11] K. Mannheim and P. L. Biermann, "Photomeson production in active galactic nuclei," *Astronomy & Astrophysics*, vol. 221, pp. 211-220, 1989.
- [12] A. Mücke, R. J. Protheroe, R. Engel, J. P. Rachen and T. Stanev, "BL Lac objects in the synchrotron proton blazar model," *Astroparticle Physics*, vol. 18, p. 593, 2003.
- [13] A. Mücke and R. J. Protheroe, "A proton synchrotron blazar model for flaring in Markarian 501," *Astroparticle Physics*, vol. 15, p. 121, 2001.
- [14] S. Gasparyan, D. Bégué and N. Sahakyan, "Time-dependent lepto-hadronic modelling of the emission from blazar jets with SOPRANO: the case of TXS 0506 + 056, 3HSP J095507.9 + 355101, and 3C 279," *Monthly Notices of the Royal Astronomical Society*, vol. 509, p. 2102, 2022.
- [15] P. Padovani and P. Giommi, "The Connection between X-Ray-- and Radio-selected BL Lacertae Objects.," *Astrophysical Journal*, vol. 444, p. 567, 1995.
- [16] A. A. Abdo and e. al., "The Spectral Energy Distribution of Fermi Bright Blazars.," *Astrophysical Journal*, vol. 716, p. 30, 2010.
- [17] P. Padovani and e. al., "Active galactic nuclei: what's in a name," *Review of Astronomy & Astrophysics*, vol. 25, p. 2, Aug 2017.
- [18] J. Biteau, E. Prandini, L. Costamante, M. Lemoine, P. Padovani, E. Pueschel, E. Resconi, F. Tavecchio, A. Taylor and A. Zech, "Progress in unveiling extreme particle acceleration in persistent astrophysical jets," *Nature Astronomy*, vol. 4, pp. 124-131, 2020.
- [19] N. Gehrels and e. al, "Erratum: The swift Gamma-ray burst mission," *Astrophysical Journal*, vol. 621, p. 558, 2005.
- [20] S. Barthelmy and e. al, "The Burst Alert Telescope (BAT) on the SWIFT Midex Mission," *Space Science Reviews*, vol. 120, pp. 143-164, 2005.
- [21] N. D. Burrows and e. al, "The Swift X-Ray Telescope," *Scientific Studies of Reading*, vol. 120, pp. 165-195, 2005.
- [22] P. Roming and e. al, "The Swift Ultra-Violet/Optical Telescope," *Space Science Reviews*, vol. 120, pp. 3-4, 2005.

- [23] A. A. Moiseev and e. al, "Observation and simulations of the backslash effects in high-energy γ -ray telescopes containing a massive calorimeter.," *Astroparticle Physics*, vol. 22, p. 275, 2004.
- [24] Ghisellini G., *Radiative Processes in High Energy Astrophysics*, vol. 873, 2013.
- [25] F. Aharonian, L. Bergström and C. Dermer, *Astrophysics at Very High Energies. Heidelberg : Swiss Society for Astrophysics and Astronomy, Saas-Fee Advanced Course,,* vol. 40, 2013.
- [26] E. Fermi, "On the Origin of the Cosmic Radiation," *Physical review*, vol. 75, no. 8, pp. 1169-1174, 15 Apr 1949.
- [27] S. Inoue and F. Takahara, "Electron Acceleration and Gamma-Ray Emission from Blazars.," *Astrophysical Journal*, vol. 463, p. 555 s.l.:, 1996.
- [28] R. Moderski, M. Sikora, P. S. Coppi and F. Aharonian, "Klein-Nishina effects in the spectra of non-thermal sources immersed in external radiation fields," *Monthly Notices of the Royal Astronomical Society*, vol. 363, pp. 954-966, 19 Apr 2005.
- [29] G. Blumenthal and R. Gould, "Bremsstrahlung, Synchrotron Radiation, and Compton Scattering of High-Energy Electrons Traversing Dilute Gases," *Reviews of Modern Physics*, vol. 42, pp. 237-271, 1970.
- [30] C. Dermer and G. Menon, "High Energy Radiation from Black Holes: Gamma Rays, Cosmic Rays, and Neutrinos," 2009.
- [31] G. E. Romero, M. Boettcher, S. Markoff and F. Tavecchio, "Relativistic Jets in Active Galactic Nuclei and Microquasars," *Space Science Reviews*, vol. 207, pp. 5-61, Jul 2017.
- [32] M. Sikora and e. al, "Constraining Emission Models of Luminous Blazar Sources," *Astrophysical Journal*, vol. 704, pp. 38-50, 2009.
- [33] M. Hayashida and e. al, "The Structure and Emission Model of the Relativistic Jet in the Quasar 3C 279 Inferred from Radio to High-energy γ -Ray Observations in 2008-2010," *Astrophysical Journal*, vol. 754, p. 114, 2012.
- [34] U. Marie-Helene, M. Laura and U. C Megan, "Variability of Active Galactic Nuclei," *Review of Astronomy and Astrophysics*, vol. 35, pp. 445-502, Jan 1997.

- [35] M. Nenkova, M. Sirocky, R. Nikutta, Ž. Ivezić and M. Elitzur, "AGN Dusty Tori. II. Observational Implications of Clumpiness," *Astrophysical Journal*, vol. 685, pp. 160-180, 2008.
- [36] S. Abdollahi and e. al, "Fermi Large Area Telescope Fourth Source Catalog," *Astrophysical Journal Supplement Series*, vol. 247, p. 33, 2020.
- [37] M. Volonteri, "Formation of supermassive black holes," *The Astronomy and Astrophysics Review*, vol. 18, pp. 279-315, 2010.
- [38] F. Stecker and e. al, "Intergalactic Photon Spectra from the Far-IR to the UV Lyman Limit for $0 < z < 6$ and the Optical Depth of the Universe to High-Energy Gamma Rays," *Astrophysical Journal*, vol. 648, pp. 774-783, 2006.
- [39] A. Dominguez and e. al, "Extragalactic background light inferred from AEGIS galaxy-SED-type fractions," *Monthly Notices of the Royal Astronomical Society*, vol. 410, pp. 2556-2578, 2011.
- [40] A. A. Abdo and e. al, "Fermi Large Area Telescope Constraints on the Gamma-ray Opacity of the Universe," *The Astrophysical Journal*, vol. 723, p. 1082-1096, 2010.
- [41] M. Ackermann and e. al, "The Imprint of the Extragalactic Background Light in the Gamma-Ray Spectra of Blazars," *Science*, vol. 338, p. 1190, 2012.
- [42] F.-L. Collaboration and e. al, "A gamma-ray determination of the Universe's star formation history," *Science*, vol. 362, p. 1031-1034, 2018.
- [43] A. Desai and e. al, "A GeV-TeV Measurement of the Extragalactic Background Light," *The Astrophysical Journal Letters*, vol. 874, p. L7, 2019.
- [44] H. a. B. K. Bloemen, "New COMPTEL gamma-ray source (GRO J0516-609) near PKS 0506-612/0522-611: first evidence for MeV Blazars," *Astronomy & Astrophysics*, vol. 293, pp. L1-L4, 1995.
- [45] G. Ghisellini and e. al, "Chasing the heaviest black holes of jetted active galactic nuclei," *Monthly Notices of the Royal Astronomical Society*, vol. 405, pp. 387-400, 2010b.
- [46] N. I. Shakura and R. A. Sunyaev, "Black holes in binary systems. Observational appearance.," *Astronomy and Astrophysics*, vol. 500, pp. 33-51, 1973.

- [47] N. Gehrels and e. al, "The Swift Gamma-Ray Burst Mission," *Astrophysical Journal*, vol. 611, pp. 1005-1020, 2004.
- [48] S. V. Paliya and e. al, "Broadband Observations of High Redshift Blazars," *Astrophysical Journal*, vol. 825, p. 74, 2016.
- [49] V. S. Paliya, "The High-redshift Blazar S5 0836+71: A Broadband Study," *Astrophysical Journal*, vol. 804, p. 74, 2015.
- [50] G. Ghisellini and e. al, "High-redshift Fermi blazars," *Monthly Notices of the Royal Astronomical Society*, vol. 401, pp. 901-914, 2011.
- [51] X. Li and e. al, "Imaging and Variability Studies of CTA 102 during the 2016 January γ -ray Flare," *Astrophysical Journal*, vol. 854, p. 17, 2018.
- [52] M. Ajello and e. al, "NuSTAR, Swift, and GROND Observations of the Flaring MeV Blazar PMN J0641-0320," *Astrophysical Journal*, vol. 826, p. 76, 2016.
- [53] A. Kaur and e. al, "New High-z Fermi BL Lacs with the Photometric Dropout Technique," *Astrophysical Journal*, vol. 834, p. 41, 2017.
- [54] M. Ackermann and e. al, "Gamma-Ray Blazars within the First 2 Billion Years," *The Astrophysical Journal Letters*, vol. 837, p. L5, 2017.
- [55] A. Kaur and e. al, "New High-z BL Lacs Using the Photometric Method with Swift and SARA," *Astrophysical Journal*, vol. 859, p. 80, 2018.
- [56] L. Marcotulli and e. al, "High-redshift Blazars through NuSTAR Eyes," *Astrophysical Journal*, vol. 839, p. 96, 2017.
- [57] V. S. Paliya and e. al, "Detection of a Gamma-Ray Flare from the High-redshift Blazar DA 193," *Astrophysical Journal*, vol. 871, p. 211, 2019.
- [58] D. G. York and e. al, "The Sloan Digital Sky Survey: Technical Summary," *The Astrophysical Journal*, vol. 120, pp. 1579-1587, 2000.
- [59] E. L. Wright and e. al, "The Wide-field Infrared Survey Explorer (WISE): Mission Description and Initial On-orbit Performance," *The Astrophysical Journal*, vol. 140, pp. 1868-1881, 2010.

- [60] W. L. Freedman and e. al, "Final Results from the Hubble Space Telescope Key Project to Measure the Hubble Constant," *Astrophysical Journal*, vol. 553, pp. 47-72, 2001.
- [61] J. Mattox and e. al, "The Likelihood Analysis of EGRET Data," *Astrophysical Journal*, vol. 461, p. 396, 1996.
- [62] B. Lott and e. al, "An adaptive-binning method for generating constant-uncertainty/constant-significance light curves with Fermi-LAT data," *Astronomy and Astrophysics*, vol. 544, p. A6, 2012.
- [63] B. Rani and e. al, "Constraining the location of rapid gamma-ray flares in the flat spectrum radio quasar 3C 273," *Astronomy & Astrophysics*, vol. 557, p. A71, 2013.
- [64] N. Sahakyan and S. Gasparyan, "High energy gamma-ray emission from PKS 1441+25," *Monthly Notices of the Royal Astronomical Society*, vol. 470, pp. 2861-2869, 2017.
- [65] N. Sahakyan, V. Baghmanyanyan and D. Zargaryan, "Fermi-LAT observation of nonblazar AGNs," *Astronomy & Astrophysics*, vol. 614, p. A6, 2018.
- [66] V. Baghmanyanyan, S. Gasparyan and N. Sahakyan, "Rapid Gamma-Ray Variability of NGC 1275," *Astrophysical Journal*, vol. 848, p. 111, 2017.
- [67] S. Gasparyan and e. al, "On the Multiwavelength Emission from CTA 102," *Astrophysical Journal*, vol. 863, p. 114, 2018.
- [68] M. S. Dutka and e. al, "Multiband Observations of the Quasar PKS 2326-502 during Active and Quiescent Gamma-Ray States in 2010-2012," *The Astrophysical Journal*, vol. 835, p. 182, 2017.
- [69] D. Zargaryan, S. Gasparyan, V. Baghmanyanyan and N. Sahakyan, "Comparing 3C 120 jet emission at small and large scales," *Astronomy & Astrophysics*, vol. 608, p. A37, 2017.
- [70] T. Poole and e. al, "Photometric calibration of the Swift ultraviolet/optical telescope," *Monthly Notices of the Royal Astronomical Society*, vol. 383, pp. 627-645, 2008.
- [71] W. Cash, "Parameter estimation in astronomy through application of the likelihood ratio.," *Astrophysical Journal*, pp. 939-47, 1979.

- [72] P. A. Evans and e. al, "Methods and results of an automatic analysis of a complete sample of Swift-XRT observations of GRBs," *Monthly Notices of the Royal Astronomical Society*, vol. 397, pp. 1177-1201, 2009.
- [73] M. Ajello and e. al, "The Fourth Catalog of Active Galactic Nuclei Detected by the Fermi Large Area Telescope," *Astrophysical Journal*, vol. 892, p. 105, 2020.
- [74] G. Ghisellini and e. al, "Jet and accretion power in the most powerful Fermi blazars," *Monthly Notices of the Royal Astronomical Society*, vol. 399, pp. 2041-2054, 2009b.
- [75] C. C. Cheung, "Fermi LAT detection of a GeV flare from High-redshift Blazar PKS 0537-286," *The Astronomer's Telegram*, vol. 10356, p. {1}, 2017.
- [76] A. A. Abdo and e. al, "Gamma-ray Light Curves and Variability of Bright Fermi-detected Blazars," *Astrophysical Journal*, vol. 722, pp. 520-542, 2010b.
- [77] V. S. Paliya and e. al, "Fermi-LAT detection of high gamma-ray activity from the $z=3.6$ quasar NVSS J163547+362930," *The Astronomer's Telegram*, vol. 11847, p. {1}, 2018.
- [78] L. Pacciani and e. al, "Exploring the Blazar Zone in High-energy Flares of FSRQs," *Astrophysical Journal*, vol. 790, p. 45, 2014.
- [79] N. Sahakyan, "Investigation of the γ -ray spectrum of CTA 102 during the exceptional flaring state in 2016-2017," *Astronomy & Astrophysics*, vol. 635, p. A25, 2020.
- [80] R. Angioni and e. al, "The large gamma-ray flare of the flat-spectrum radio quasar PKS 0346-27," *Astronomy & Astrophysics*, vol. 627, p. A140, 2019.
- [81] A. Dar and A. Laor, "Hadronic Production of TeV Gamma-Ray Flares from Blazars," *Astrophysical Journal Letters*, vol. 478, pp. L5-L8, 1997.
- [82] J. H. Beall and W. Bednarek, "On the Hadronic Beam Model for Gamma-Ray Production in Blazars," *Astrophysical Journal*, vol. 510, pp. 188-196, 1999.
- [83] W. Bednarek and R. J. Protheroe, "Gamma-rays from interactions of stars with active galactic nucleus jets," *Monthly Notices of the Royal Astronomical Society*, vol. 287, pp. L9-L13, 1997.

- [84] K. Mannheim, "High-energy neutrinos from extragalactic jets," *Astroparticle Physics*, vol. 3, pp. 295-302, 1995.
- [85] A. Paggi and e. al, "Flaring Patterns in Blazars," *Astrophysical Journal*, vol. 736, p. 128, 2011.
- [86] J. G. Kirk and A. F. Heavens, "Particle acceleration at oblique shock fronts," *Monthly Notices of the Royal Astronomical Society*, vol. 239, pp. 995-1011, 1989.
- [87] D. C. Ellison and e. al, "First-Order Fermi Particle Acceleration by Relativistic Shocks," *Astrophysical Journal*, vol. 360, p. 702, 1990.
- [88] E. Summerlin and M. Baring, "Diffusive Acceleration of Particles at Oblique, Relativistic, Magnetohydrodynamic Shocks," *Astrophysical Journal*, vol. 745, p. 63, 2012.
- [89] L. O. Drury, "REVIEW ARTICLE: An introduction to the theory of diffusive shock acceleration of energetic particles in tenuous plasmas," *Reports on Progress in Physics*, vol. 46, pp. 973-1027, 1983.
- [90] M. Baring, M. Böttcher and E. Summerlin, "Probing acceleration and turbulence at relativistic shocks in blazar jets," *Monthly Notices of the Royal Astronomical Society*, vol. 464, pp. 4875-4894, 2017.
- [91] M. L. Ahnen and e. al, "Very High Energy γ -Rays from the Universe's Middle Age: Detection of the $z = 0.940$ Blazar PKS 1441+25 with MAGIC}," *The Astrophysical Journal Letters*, vol. 815, p. L23, 2015.
- [92] A. U. Abeysekara and e. al, "Gamma-Rays from the Quasar PKS 1441+25: Story of an Escape," *The Astrophysical Journal Letters*, vol. 815, p. L22, 2015.
- [93] MAGIC Collaboration, "Multi-wavelength characterization of the blazar S5 0716+714 during an unprecedented outburst phase," *Astronomy and Astrophysics*, vol. 619, p. A45, 2018.
- [94] M. Hayashida and e. al, "Rapid Variability of Blazar 3C 279 during Flaring States in 2013-2014 with Joint Fermi-LAT, NuSTAR, Swift, and Ground-Based Multiwavelength Observations," *Astrophysical Journal*, vol. 807, p. 79, 2015.

- [95] M. Sikora and e. al, "On the Nature of MeV Blazars," *Astrophysics Journal*, vol. 577, pp. 78-84, 2002.
- [96] A. Tramacere, E. Massaro and A. Taylor, "Swift observations of the very intense flaring activity of Mrk 421 during 2006. I. Phenomenological picture of electron acceleration and predictions for MeV/GeV emission," *Astrophysical Journal*, vol. 739, p. 66, 2011.
- [97] A. Tramacere, P. Giommi, M. Perri, F. Verrecchia and G. Tosti, "Swift observations of the very intense flaring activity of Mrk 421 during 2006. I. Phenomenological picture of electron acceleration and predictions for MeV/GeV emission," *Astronomy & Astrophysics*, vol. 501, pp. 879-898, 2009.
- [98] E. Massaro, A. Tramacere, M. Perri, P. Giommi and G. Tosti, "Log-parabolic spectra and particle acceleration in blazars. III. SSC emission in the TeV band from Mkn501," *Astronomy & Astrophysics*, vol. 448, pp. 861-871, 2006.
- [99] G. B. Rybicki and A. P. Lightman, *Radiative processes in astrophysics*, 1979.
- [100] F. Tavecchio and e. al, "The X-Ray Jet of PKS 0637-752: Inverse Compton Radiation from the Cosmic Microwave Background?," *The Astrophysical Journal Letters*, vol. 544, pp. L23-L26, 2000.
- [101] J. Zhang and e. al, "Relativistic Jet Properties of GeV-TeV Blazars and Possible Implications for the Jet Formation, Composition, and Cavity Kinematics," *Astrophysical Journal*, vol. 788, p. 104, 2014.
- [102] A. Celotti and G. Ghisellini, "The power of blazar jets," *Monthly Notices of the Royal Astronomical Society*, vol. 385, pp. 283-300, 2008.
- [103] G. Ghisellini and F. Tavecchio, "Fermi/LAT broad emission line blazars," *Monthly Notices of the Royal Astronomical Society*, vol. 448, pp. 1060-1077, 2015.
- [104] V. S. Paliya and e. al, "General Physical Properties of CGRaBS Blazars," *Astrophysical Journal*, vol. 851, p. 33, 2017.
- [105] I. Liodakis and V. Pavlidou, "Population statistics of beamed sources - II. Evaluation of Doppler factor estimates," *Monthly Notices of the Royal Astronomical Society*, vol. 454, pp. 1767-1777, 2015.

- [106] S. Cutini and e. al, "Radio-gamma-ray connection and spectral evolution in 4C +49.22 (S4 1150+49): the Fermi, Swift and Planck view," *Monthly Notices of the Royal Astronomical Society*, vol. 445, pp. 4316-4334, 2014.
- [107] E. J. Summerlin and e. al, "Diffusive Acceleration of Particles at Oblique, Relativistic, Magnetohydrodynamic Shocks," *Astrophysical Journal*, vol. 745, p. 63, 2012.
- [108] F. M. Rieger and e. al, "Fermi acceleration in astrophysical jets," *Ap&SS*, vol. 309, pp. 119-125, 2007.
- [109] G. Ghisellini and e. al, "The power of relativistic jets is larger than the luminosity of their accretion disks," *Nature*, vol. 515, pp. 376-378, 2014.
- [110] L. Maraschi and F. Tavecchio, "The Jet-Disk Connection and Blazar Unification," *Astrophysical Journal*, vol. 593, pp. 667-675, 2003.
- [111] G. Ghisellini and e. al, "The blazar S5 0014+813: a real or apparent monster?," *Monthly Notices of the Royal Astronomical Society*, vol. 399, pp. L24-L28, 2009.
- [112] G. Ghisellini and e. al, "General physical properties of bright Fermi blazars," *Monthly Notices of the Royal Astronomical Society*, vol. 402, p. 497-518, 2010a.
- [113] M. S. Shaw and e. al, "Spectroscopy of Broad-line Blazars from 1LAC," *Astrophysical Journal*, vol. 748, p. 49, 2012.
- [114] G. Calderone and e. al, "Black hole mass estimate for a sample of radio-loud narrow-line Seyfert 1 galaxies," *Monthly Notices of the Royal Astronomical Society*, vol. 431, pp. 210-239, 2013.
- [115] Y. Shen and e. al, "A Catalog of Quasar Properties from Sloan Digital Sky Survey Data Release 7," *Astrophysical Journal Supplement Series*, vol. 194, p. 45, 2011.
- [116] T. M. Kneiske and e. al, "Implications of cosmological gamma-ray absorption. II. Modification of gamma-ray spectra," *Astronomy & Astrophysics*, vol. 413, pp. 807-815, 2004.
- [117] D. Mazin and M. Raue, "New limits on the density of the extragalactic background light in the optical to the far infrared from the spectra of all known TeV blazars," *Astronomy & Astrophysics*, vol. 471, pp. 439-452, 2007.

- [118] A. Franceschini, G. Rodighiero and M. Vaccari, "Extragalactic optical-infrared background radiation, its time evolution and the cosmic photon-photon opacity," *Astronomy & Astrophysics*, vol. 487, pp. 837-852, 2008.
- [119] A. A. Abdo and e. al, "Spectrum of the Isotropic Diffuse Gamma-Ray Emission Derived from First-Year Fermi Large Area Telescope Data," *Physical Review Letters*, vol. 104, p. 101101, 2010.
- [120] S. Abdollahi and e. al, "Incremental Fermi Large Area Telescope Fourth Source Catalog," *Astrophysical Journal*, vol. 260, p. 53, 2022.
- [121] V. S. Paliya and e. al, "Blazars at the Cosmic Dawn," *Astrophysical Journal*, vol. 897, p. 177, 2020.
- [122] N. Sahakyan and e. al., "Multiwavelength study of high-redshift blazars," *Monthly Notices of the Royal Astronomical Society*, vol. 498, p. 2594–2613, 2020.
- [123] W. Atwood, A. Abdo, M. Ackermann, W. Althouse and e. al., "The Large Area Telescope on the Fermi Gamma-Ray Space Telescope Mission," *Astrophysical Journal* , vol. 697, pp. 1071-1102, 2009.
- [124] Harrison and e. al, "The Nuclear Spectroscopic Telescope Array (NuSTAR) High-energy X-Ray Mission," *Astrophysical Journal*, vol. 770, p. 103, 2013.
- [125] A. E. Wright and e. al, "PKS 0537-286: a high-redshift QSO with an extreme Lyman-continuum cutoff.," *Astrophysical Journal*, vol. 226, pp. L61-L64, 1978.
- [126] G. Zamorani and e. al, "X-ray studies of quasars with the Einstein Observatory II," *Astrophysical Journal*, vol. 245, pp. 357-374, 1981.
- [127] J. Siebert and e. al, "ASCA observations of high redshift quasars.," *Astronomy & Astrophysics*, vol. 307, p. 8, 1996.
- [128] M. Cappi, M. Matsuoka, A. Comastri, W. Brinkmann and e. al., "ASCA and ROSAT X-Ray Spectra of High-Redshift Radio-loud Quasars," *Astrophysical Journal*, vol. 478, pp. 492-510, 1997.

- [129] F. Fiore, M. Elvis, P. Giommi and P. Padovani, "X-Ray Spectral Survey of WGACAT Quasars. I. Spectral Evolution and Low-Energy Cutoffs," *Astrophysical Journal*, vol. 492, pp. 79-90, 1998.
- [130] R. Angioni, "Fermi-LAT detection of renewed gamma-ray activity from the high-redshift FSRQ PKS 0537-286," *The Astronomer's Telegram*, vol. 14285, p. 1, 2020.
- [131] J. Valverde and J. Forman, "Fermi-LAT detection of renewed gamma-ray activity from the FSRQ PKS 0537-286," *The Astronomer's Telegram*, vol. 15405, p. 1, 2022.
- [132] N. Sahakyan and e. al, "A Multiwavelength Study of Distant Blazar PKS 0537-286," *Astrophysics*, vol. 63, pp. 459-469, 2020.
- [133] E. e. a. Bottacini, "PKS 0537-286, carrying the information of the environment of SMBHs in the early Universe," *Astronomy & Astrophysics*, vol. 509, p. A69, 2010.
- [134] R. Britto, E. Bottacini, B. Lott, S. Razzaque and S. Buson, "Fermi-LAT Observations of the 2014 May-July Outburst from 3C 454.3," *Astrophysical Journal*, vol. 830, p. 162, 2016.
- [135] N. Sahakyan, "Modelling the broad-band emission of 3C 454.3," *Monthly Notices of the Royal Astronomical Society*, vol. 504, pp. 5074-5086, 2021.
- [136] N. Sahakyan and e. al, "Modelling the time variable spectral energy distribution of the blazar CTA 102 from 2008 to 2022," *Monthly Notices of the Royal Astronomical Society*, vol. 517, p. 2757-2768, 2022.
- [137] N. Sahakyan and P. Giommi, "A 13-yr-long broad-band view of BL Lac," *Monthly Notices of the Royal Astronomical Society*, vol. 513, pp. 4645-4656, 2022.
- [138] R. Middei, P. Giommi, M. Perri, S. Turriziani and e. al., "The first hard X-ray spectral catalogue of Blazars observed by NuSTAR," *Monthly Notices of the Royal Astronomical Society*, vol. 514, pp. 3179-3190, 2022.
- [139] K. Arnaud, "XSPEC: The First Ten Years," vol. 101, p. 17, 1996.
- [140] P. Giommi and e. al, "X-ray spectra, light curves and SEDs of blazars frequently observed by Swift," *Monthly Notices of the Royal Astronomical Society*, vol. 507, p. 5690-5702, 2021.

- [141] Y.-L. Chang and C. B. a. P. Giommi, "The Open Universe VOU-Blazars tool," *Astronomy and Computing*, vol. 30, no. 2213-1337, pp. 100-350, 2020.
- [142] A. Mainzer and e. al, "Initial Performance of the NEOWISE Reactivation Mission," *Astrophysical Journal*, vol. 792, p. 30, 2014.
- [143] C. Dermer, R. Schlickeiser and A. Mastichiadis, "High-energy gamma radiation from extragalactic radio sources.," *Astronomy and Astrophysics*, vol. 256, pp. L27-L30, 1992.
- [144] C. D. Dermer and R. Schlickeiser, "On the Location of the Acceleration and Emission Sites in Gamma-Ray Blazars," *The Astrophysical Journal Supplement Series*, vol. 90, p. 945, 1994.
- [145] A. C. Donea and R. Protheroe, "Radiation fields of disk, BLR and torus in quasars and blazars: implications for γ -ray absorption," *Astroparticle Physics*, vol. 18, pp. 377-393, 2003.
- [146] E. Massaro and e. al, "Log-parabolic spectra and particle acceleration in blazars. III. SSC emission in the TeV band from Mkn501," *Astronomy & Astrophysics*, vol. 448, pp. 861-871, 2006.
- [147] A. Tramacere, "JetSeT: Numerical modeling and SED fitting tool for relativistic jets," *Astrophysics Source Code Library*, p. ascl:2009.001, 2020.
- [148] A. A. Abdo and e. al, "FERMI LARGE AREA TELESCOPE AND MULTI-WAVELENGTH OBSERVATIONS OF THE FLARING ACTIVITY OF PKS 1510-089 BETWEEN 2008 SEPTEMBER AND 2009 JUNE," *Astrophysical Journal*, vol. 1425, p. 721, 2010.
- [149] N. Sahakyan and P. Giommi, "The strange case of the transient HBL blazar 4FGL J1544.3-0649," *Monthly Notices of the Royal Astronomical Society*, vol. 502, pp. 836-844, 2021.
- [150] J. N. Reeves and e. al, "The first XMM-Newton spectrum of a high redshift quasar - PKS 0537-286," *Astronomy & Astrophysics*, Vols. L116 - L121, p. 365, 2001.
- [151] P. Pjanka and e. al, "The power and production efficiency of blazar jets," *Monthly Notices of the Royal Astronomical Society*, vol. 465, p. 3506-3514, 2017.

- [152] A. M. Brown, "Locating the γ -ray emission region of the flat spectrum radio quasar PKS 1510-089," *Monthly Notices of the Royal Astronomical Society*, vol. 431, pp. 824-835, 2013.
- [153] R. Buehler, "Fermi LAT detection of a GeV flare from the high redshift blazar B3 1343+451," *The Astronomer's Telegram*, vol. 2217, 2009.
- [154] O. Roopesh, "Highest gamma-ray flux level detected from very high redshift blazar B3 1343+451," *The Astronomers Telegram*, vol. 3793, 2011.
- [155] E. Massaro and e. al, "Log-parabolic spectra and particle acceleration in the BL Lac object Mkn 421: Spectral analysis of the complete BeppoSAX wide band X-ray data set," *Astronomy & Astrophysics*, vol. 413, pp. 489-503, 2004.
- [156] A. A. Abdo and e. al, "PKS 1502+106: A New and Distant Gamma-ray Blazar in Outburst Discovered by the Fermi Large Area Telescope," *Astrophysical Journal*, vol. 710, pp. 810-827, 2010.
- [157] J. Kirk, F. Rieger and A. Mastichiadis, "Particle acceleration and synchrotron emission in blazar jets," *Astronomy and Astrophysics*, vol. 333, pp. 452-458, 1998.
- [158] A. A. Abdo and e. al, "Fermi Discovery of Gamma-ray Emission from NGC 1275," *Astrophysical Journal*, vol. 699, pp. 31-39, 2009.
- [159] N. Sahakyan, D. Zargaryan and V. Baghmanyanyan, "On the gamma-ray emission from 3C 120," *Astronomy and Astrophysics*, vol. 574, p. A88, 2015.
- [160] A. A. Abdo and e. al, "Fermi Large Area Telescope View of the Core of the Radio Galaxy Centaurus A," *Astrophysical Journal*, vol. 719, pp. 1433-1444, 2010.
- [161] G. Ghisellini, L. Maraschi and F. Tavecchio, "The Fermi blazars' divide," *Monthly Notices of the Royal Astronomical Society*, vol. 396, pp. L105-L109, 2009.
- [162] S. a. A. F. e. a. Abdollahi, "Incremental Fermi Large Area Telescope Fourth Source Catalog," *ApJ*, vol. 260, p. 53, 2022.
- [163] B. Rani and e. al, "Radio to gamma-ray variability study of blazar S5 0716+714," *Astronomy and Astrophysics*, vol. 552, p. A11, 2013.

- [164] HI4PI Collaboration, "HI4PI: A full-sky H I survey based on EBHIS and GASS," *Astronomy and Astrophysics*, vol. 594, p. A116, 2016.
- [165] P. Kalberla and e. al, "The Leiden/Argentine/Bonn (LAB) Survey of Galactic HI. Final data release of the combined LDS and IAR surveys with improved stray-radiation corrections," *Astronomy and Astrophysics*, vol. 440, pp. 775-782, 2005.
- [166] J. Dickey and F. Lockman, "H I in the galaxy," *Annual Review of Astronomy and Astrophysics*, vol. 28, pp. 215-261, 1990.